UNIVERSITY of CALIFORNIA
Santa Barbara

Tensor Network Wavefunctions for Topological Phases

A dissertation submitted in partial satisfaction of the
requirements for the degree

Doctor of Philosophy

in

Physics

by

Brayden Alexander Ware

Committee in charge:

Professor Chetan Nayak, Co-Chair

Dr. Bela Bauer, Co-Chair

Professor David Weld

September 2017

The dissertation of Brayden Alexander Ware is approved.

David Weld

Bela Bauer, Committee Co-Chair

Chetan Nayak, Committee Co-Chair

August 2017

Acknowledgements

This dissertation could only be completed with the support and assistance of many people. I give my greatest thanks to:

My advisor, Bela Bauer, for his encouragement and guidance. Throughout my graduate school career, Bela was there to gently nudge me in the right direction no matter how many times I stubbornly struck off in a different direction.

Chetan Nayak, Roman Lutchyn, Parsa Bonderson, Zhenghan Wang, and Mike Freedman, for creating the lively and friendly physics enviroment within Station Q. In the Station Q seminar room, new ideas were broken down and discussed until everybody understood them in their own way, practice talks were patiently analyzed and improved point by point from start to finish, and pies were demolished. Additionally, the Station Q postdocs Meng Cheng, Mike Zaletel, Mike Mulligan, and Maissam Barkeshli for many inspiring physics discussions.

My collaborators on the work contained in this thesis: Sid Parameswaran and Itamar Kimchi for inspiring the first project in this thesis and launching me into the field of entanglement and topological phases, and Jun Ho Son, Jason Alicea, and Ryan Mishmash for combining their ongoing project with ours to make something greater than the sum of the two parts.

My fellow graduate students, for many long and fruitful physics discussions, especially Jen Cano, Eugeniu Plamadeala, Dominic Else, Alex Rasmussen, Kaushal Patel, Kevin Slagle, Christina Knapp, and Zhen Bi.

Teddy Parker, Keith Fratus, and Kevin Kuns for wide ranging discussions on physics, life, and esoteric facts that challenged me to put my ideas into sound explanations and to rethink what I thought I knew.

Hunter Banks, Thomas Malkowski, Bill Wolf, Sara Sterphone, Eric Rind, Charles de las Casas, Ruwan Senaratne, Zach Geiger, Alex Miller, Sebastian Fischetti, Kurt Fujiwara, Shankari Rajagopal, and many more, for making Santa Barbara feel like home.

My mom and dad, my brother Taylor, and my sister Caroline for their constant support and encouragement.

Special thanks to David Weld for serving on my committee.

Curriculum Vitæ

Brayden Alexander Ware

Education

Ph.D. in Physics, University of California, Santa Barbara, expected June 2017.

M.S. in Physics, University of California, Santa Barbara, 2014.

S.B. in Mathematics and Physics, Massachusetts Institute of Technology, 2011.

Publications

Topological crystalline Bose insulator in two dimensions via entanglement spectrum
B. Ware, I. Kimchi, S. Parameswaran, B. Bauer
Phys. Rev. B 92, 195105 (2015)

Ising Anyons in Frustration-Free Majorana-Dimer Models
B. Ware, J.H. Son, M. Cheng, R.V. Mishmash, J. Alicea, B. Bauer
Phys. Rev. B 94, 115127 (2016)

Featureless quantum insulator on the honeycomb lattice
P. Kim, H. Lee, S. Jiang, **B. Ware**, C-M. Jian, M. Zaletel, J. Han, Y. Ran
Phys. Rev. B 94, 064432 (2016)

Talks and Posters

Commuting Projector Models for Fermionic Symmetry Protected and Topological Phases
Talk at Symmetry, Topology, and Quantum Phases Program, KITP, Santa Barbara CA, December 2016

Majorana-dimer models and fermionic topological phases
Talk at Synthetic Quantum Matter Program, KITP, Santa Barbara CA, September 2016

Symmetry-enriched topological invariants from tensor network representations
Talk at APS March Meeting, Baltimore MD, March 2016.

Non-trivial edge physics in a featureless Mott insulator
Talk at APS March Meeting, San Antonio TX, March 2015.

Featureless Bosonic Insulators
Poster at TOPO2015, Cargèse, France, September 2015.

Professional Development

California Summer Workshop on Advanced Research in Materials
University of California Irvine, June 2016.

Topological Phases in Condensed Matter and Cold Atoms Systems (TOPO2015)
Institut d'Etudes Scientifiques de Cargèse, September 2015

Station Q Semiannual Meeting
Station Q, Santa Barbara CA, June 2016, December 2015 and June 2015

Workshop on Tensor Networks and Simulations
Simons Institute, Berkeley CA, April 2014

Pfaffians!: Dimer Models and Majorana Fermions
Talk for UCSB Many Body Journal Club, Februrary 2016

Parton mean-field constructions of spin liquids
Talk for Seminar on Spin Liquids, October 2015

Haah's Code: Fractal-like excitations from ring theory
Talk for Seminar on Topological Phases, April 2015

Loop model construction for $SU(2)_k$ anyon theories
Talk for Seminar on Topological Phases, October 2014

Time-Reversal and Fermion Parity symmetric states in 1D
Talk for Seminar on Topological Phases, September 2014

Introduction to Tensor Networks with applications to topological phases
Talk for UCSB Many Body Journal Club, August 2014

Introduction to Z_2 Gauge Theory
Talk for UCSB Many Body Journal Club, May 2013

A Quantum Algorithm to Compute the Jones Polynomial at $q = e^{\frac{2\pi i}{k}}$
Course Paper for Quantum Information & Quantum Computation, Winter 2013

Teaching Experience

Teaching Assistant for graduate courses:
Statistical Mechanics, Concepts of Condensed Matter Physics

Teaching Assistant for special topics course: Group Theory for Physicists

Teaching Assistant for undergraduate courses:
Quantum Mechanics I and II, Electromagnetism, Advanced Electromagnetism, Thermodynamics and Waves, Basic Astronomy, Introductory Physics Labs

Abstract

Tensor Network Wavefunctions for Topological Phases

by

Brayden Alexander Ware

The combination of quantum effects and interactions in quantum many-body systems can result in exotic phases with fundamentally entangled ground state wavefunctions – topological phases. Topological phases come in two types, both of which will be studied in this thesis. In *topologically ordered* phases, the pattern of entanglement in the ground state wavefunction encodes the statistics of exotic emergent excitations, a universal indicator of a phase that is robust to all types of perturbations. In *symmetry protected topological* phases, the entanglement instead encodes a universal response of the system to symmetry defects, an indicator that is robust only to perturbations respecting the protecting symmetry.

Finding and creating these phases in physical systems is a motivating challenge that tests all aspects - analytical, numerical, and experimental - of our understanding of the quantum many-body problem. Nearly three decades ago, the creation of simple ansatz wavefunctions - such as the Laughlin fractional quantum hall state, the AKLT state, and the resonating valence bond state - spurred analytical understanding of both the role of entanglement in topological physics and physical mechanisms by which it can

arise. However, quantitative understanding of the relevant phase diagrams is still challenging. For this purpose, tensor networks provide a toolbox for systematically improving wavefunction ansatz while still capturing the relevant entanglement properties.

In this thesis, we use the tools of entanglement and tensor networks to analyze ansatz states for several proposed new phases. In the first part, we study a featureless phase of bosons on the honeycomb lattice and argue that this phase can be topologically protected under any one of several distinct subsets of the crystalline lattice symmetries. We discuss methods of detecting such phases with entanglement and without.

In the second part, we consider the problem of constructing fixed-point wavefunctions for *intrinsically fermionic* topological phases, i.e. topological phases contructed out of fermions with a nontrivial response to fermion parity defects. A zero correlation length wavefunction and a commuting projector Hamiltonian that realizes this wavefunction as its ground state are constructed. Using an appropriate generalization of the minimally entangled states method for extraction of topological order from the ground states on a torus to the intrinsically fermionic case, we fully characterize the corresponding topological order as $\text{Ising} \times (p_x - ip_y)$. We argue that this phase can be captured using fermionic tensor networks, expanding the applicability of tensor network methods.

Contents

Chapter 0

Introduction

The classical understanding of many-body physics involves local order parameters and their thermal and quantum fluctuactions. After the discovery of the fractional Quantum Hall effect in 1982, it was realized that there exist a variety of phases of matter with fluctuations remaining at zero temperature and with no local order parameters. These so called topological phases were outside the purview of the existing Landau theory, and they brought a number of surprising new features to the study of many body physics, such as emergent collective excitations with fractional charge and statistics and backscattering-free edge states. These exotic phenomena attracted a great amount of research interest, in part driven by the hope of applications to new generations of electronics and superconductors. More importantly, this new field has transformed our understanding of the quantum many-body problem by shifting the focus from correlations to quantum entanglement. The fractionalized excitations and edge states are ultimately consequences of

patterns of entanglement in the ground state that exist independently from local correlations, and moreover that cannot be modfied by local perturbations. For this reason, topological phases could also be useful for applications in quantum computing.

The most striking aspect of topological phenomena was that macroscopic and unpristine electronic systems adhered to rather simple predictions with unprecedented precision, such as in the fractional Quantum Hall effect, where the Hall conductance becomes pinned to quantized values

$$\sigma_H = \frac{p}{q} \times \frac{e^2}{h}$$

with precision better than several parts in 10^8 [3] – a measurement so precise that it is used to define the value of $\frac{e^2}{h}$. [78] The explanation for this extraordinary robustness is in the existence of an energy gap above the ground state – which implies that the ground state wavefunction changes continuously for small perturbations in the Hamiltonian – and in *topological protection*, i.e the existence of distinct classes of wavefunctions that cannot be connected continuously. The key to unlocking analytical and computational understanding of topological phases is the ability to produce wavefunctions in the appropriate topological class. In the study of the fractional Quantum Hall effect alone, the ability to write down such a wavefunction (the Laughlin wavefunction [93]) spurred the development of the low-energy field theory descriptions of this phase [19, 53] and elucidated the essential flux attachment mechanism behind the phenomena. The computational study of microscopic Hamiltonians for the fractional quantum Hall effect was also bolstered; a Hamiltonian whose ground state is exactly the Laughlin state and thus

known to realize the appropriate phase was found [66], followed by numerical evidence to show that it could be continously connected to more realistic Hamiltonians[65].

This thesis is concerned with how to identify these distinct topological classes of wavefunctions with their corresponding gapped phases of quantum matter using the tools of entanglement and symmetry. Additionally, we'd like to have good classes of variational wavefunctions for the purpose of efficient numerical simulations. Both of these problems have been largely solved in one dimension, so the scenarios we investigate will be in two dimensions.

0.1 Topologically Ordered Phases

Unentangled quantum phases distinguished by patterns of spontaneous symmetry breaking generically lose their sharp distinctions when perturbations breaking the symmetry are allowed. This motivates the consideration of a coarser notion of phase involving no symmetry, or in other words, phases that are completely stable to all types of perturbations. This notion can be formalized via the notion of gapped quasi-adiabatic evolution or via low depth quantum circuits[72, 29]. Under this definition, there is precisely one phase with an unentangled ground state (since any two different unentangled ground states can be continuously connected). The other phases are the *topologically ordered* phases, which by definition have global patterns of entanglement that cannot be generated locally. This situation is illustrated in Fig. 1(a). While we generally can break all symmetries by considering arbitrary perturbations, one exception must be made for

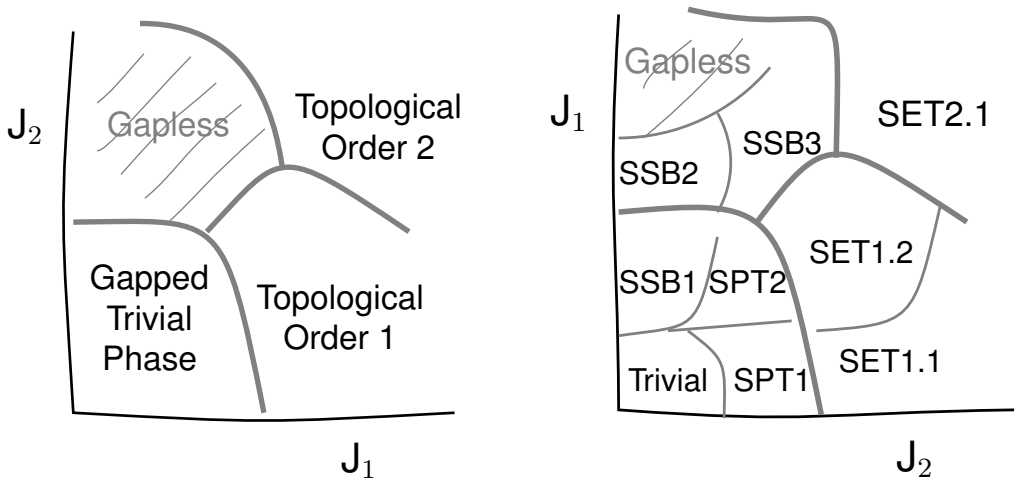

(a) No symmetry

(b) With symmetry G

Figure 1: Generic phase structure in phase diagrams with and without symmetry. Without symmmetry, gapped phases are distinguished only by topological order or, for the single short ranged entangled phase, lack of topological order. With symmetry, short range entangled phases can be distinguished both by symmetry breaking patterns and by symmetry protected topological (SPT) order. Distinctions between phases with the same topological order also appear; these are denoted SET, for symmetry enriched topological order.

fermion parity, since local Hamiltonians can't break fermion parity. In what follows, we consider phases made of bosonic degrees of freedom only unless specifically specified: phases made of fermions will be discussed separately in Chapter 2.

With symmetry considerations removed, the key property distinguishing various topological orders in two dimensions is the emergence of *anyons*, point-like excitations with statistics differing from the usual bosons and fermions. These excitations also exhibit mutual braiding statistics, universal Berry phases that occur for adiabatic processes that wind the excitations around each other. An extensive physical and mathematical framework has been developed for the understanding the self- and mutual- braiding statistics

of anyon systems [85, 20]. For the purpose of numerical simulations, it is often more convenient to work with the ground states than with the excitations and to consider periodic boundary conditions. Topological order with emergent anyons guarantees the existence of degenerate ground states. The argument goes as follows: for each anyon a, there is an operator W_x^a that creates a pair of anyons a and $\bar{a}$, drags them around the x cycle of the torus, and reannihilates the pair on the other side. Since no excitations are left at the end, this operator commutes with the Hamiltonian and maps ground states to ground states. Similarly, the same operators exist for the other cycle y of the torus. These operators don't commute when a and b are excitations with mutual braiding statistics θ_{ab}:

$$W_x^a W_y^b = e^{i\theta_{ab}} W_y^b W_x^a,$$

as illustrated in Fig. 0.1. For the ground states to carry an action of this non-commutative algebra, there must be multiple ground states. The minimal allowed number is given by exactly the number of distinct anyon types, where anyons a and $\tilde{a}$ are considered to be the same type if their braiding with other anyons is the same:

$$\theta_{ab} = \theta_{\tilde{a}b} \text{ for all anyons } b \implies a \equiv \tilde{a}.$$

The degeneracy in these ground states cannot be split by local operators in the thermodynamic limit. Intuitively, the braiding phases could be measured using anyons far separated in terms of correlation length from each other and from any given local dis-

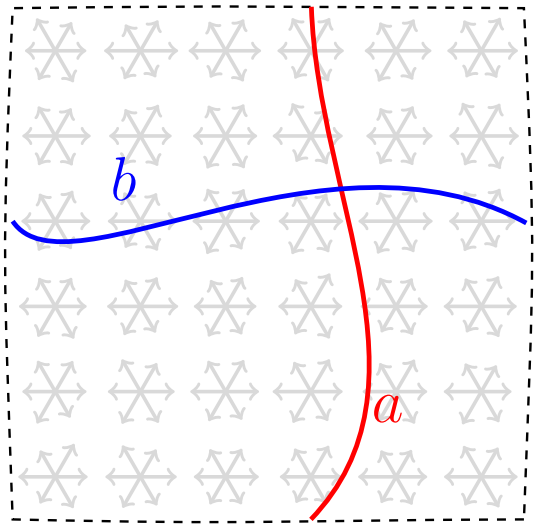

Figure 2: An illustration of $W_x^a\ W_y^b$ acting on a ground state. The operations don't commute, as switching the order is differs by a braid of a and b.

turbance. Given one ground state $|1\rangle$, a basis for the full set of ground states is given by

$$\{W_x^a|1\rangle \text{ for each anyon type } a\}.$$

In finite size systems, perturbations generically cause small energy splittings between the ground states via processes that tunnel between ground states as illustrated in Fig. 3. Due to the one-dimensional support of the operator that tunnels between ground states, the finite size splitting scales as

$$\Delta E \sim e^{-L/\xi},$$

in contrast with the

$$\Delta E \sim e^{-(L/\xi)^2}$$

in spontaneously symmetry broken phases.

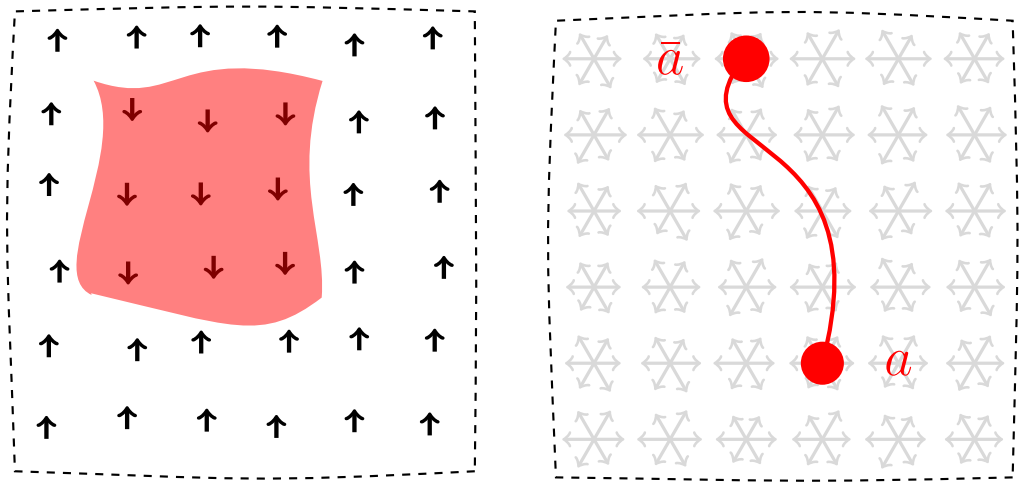

(a) in symmetry breaking phases (b) in topological phases

Figure 3: The degenerate ground states under periodic boundary conditions are useful for distinguishing phases. In spontaneous symmetry breaking phases, in order for a ground state with one value of the local order parameter to tunnel to a different ground state, a domain must form and spread over the whole system, as shown in (a). In topologically ordered phases, an anyon tunneling around a cycle will take you to a different ground state, as shown in (b).

While this argument shows that emergent anyons lead to protected degeneracy, it is believed that the argument reverses: 2D systems with robust degenerate ground states in periodic boundary conditions have as many anyon types as degenerate ground states. Furthermore, it is believed that topological order is completely characterized by anyonic statistics along with a measure of edge modes called the chiral central charge [152]. (This additional allowance is for the one known 2D topological order without anyons, known as the E_8 bosonic Quantum Hall state and copies of it [102].)

While formally topological order is about quantum phases in the absence of symmetry, the question of how to find topological order in physical systems – in strongly correlated electron systems, frustrated quantum magnets, cold atomic gases, or elsewhere - is often

intertwined with symmetry considerations, as the anyon excitations will ultimately be made up of microscopic constituents that have conserved spin, charge, or particle number and that exist in a background potential with approximate crystalline symmetries. Notably, since anyon excitations can only be created in pairs (more precisely, can only be created in sets that fuse to the vacuum) the individual excitations do not have to come in linear representations of the symmetry. This allows for symmetry fractionalization; for example, quasiparticles in the fractional Quantum Hall effect carry electrical charge that is a fraction of the charge of an electron. When these symmetries are restored to generic phase diagrams, the broad groupings of topological phases split into distinct phases, each with a unique pattern of symmetry fractionalization. These patterns are referred to as *symmetry enriched topological orders*, or SETs. This situation is illustrated in Fig. 1(b).

0.2 Symmetry Protected Topological Phases

There can also be symmetry enforced distinctions between phases that are topologically trivial and contain no symmetry breaking. The experimental discovery [91] of topological band insulators that cannot be adiabatically continued to the atomic limit as long as time-reversal invariance is preserved [126, 69] has spurred the exploration of a broad array of phases where symmetries protect subtle, non-local features that distinguish them from trivial, unentangled insulators. These phases, collectively known as symmetry-protected topological (SPT) phases [27], have by now been observed in several experimental realizations in one, two and three dimensions and an extensive

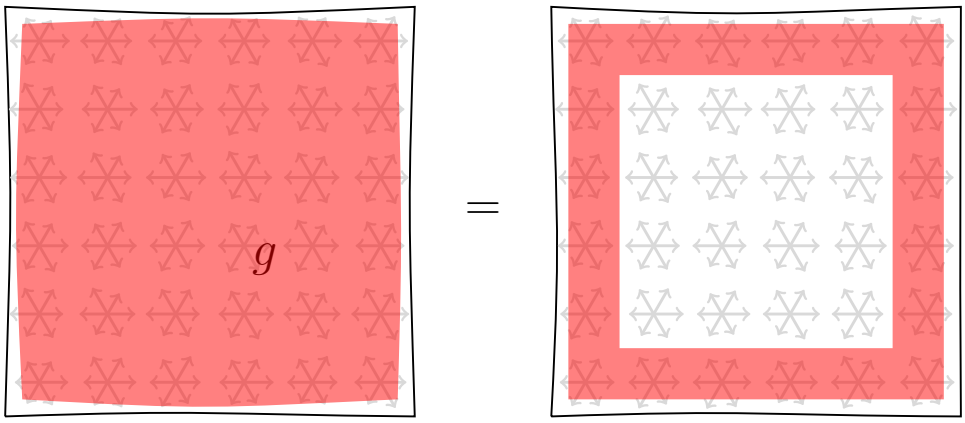

Figure 4: For a symmetric phase, applying the action of the symmetry in the bulk leaves the wavefunction invariant. In open boundary conditions, a nontrivial SPT phase has low energy states with that carry anomalous symmetry action.

mathematical framework has been developed for their characterization and classification [133, 30, 137, 132, 28, 151, 150].

Unlike topologically ordered phases, these phases are often only subtly distinguished from a trivial insulator in the bulk. Instead, the topological properties can be observed by focusing on the boundary of a finite system. In many cases, the boundary exhibits gapless features such as the localized Majorana zero modes at the ends of one-dimensional topological superconductors [84], the helical edge states of the quantum spin Hall effect [67, 81, 18] and the protected Dirac cones on the surface of three-dimensional $\mathbb{Z}_2$ topological insulators [56]. The unifying theme of these disparate edge phenomena is *anomalous* symmetry action, a generalization of symmetry fractionalization to extended objects [41].

In one dimensional phases, this can be illustrated simply with the AKLT chain, an exactly solvable model of spin-1s [1]. The exact ground state wavefunctions in this

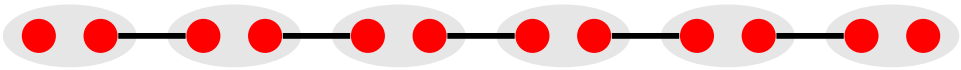

Figure 5: AKLT chain and charicature of 1D SPTs. An SO(3) symmetric and local perturbation cannot couple the remaining spin-1/2s, the gapless edge states remain.

model can be formed by using a splitting of the spin-one on each site into a pair of spin-1/2s, then by pairing the spin-1/2s into singlets between sites of the chain. When the chain is cut open, dangling spin-1/2 edge states appear at the boundaries. This pair of spin-1/2s represent a Hilbert space of size 4 and are the only remaining degrees of freedom accessible below the energy gap – in the bulk, all the spins are paired. Due to the integer spin representation of the spin at each site, these states as a collection are $SO(3)$ symmetric. However, in the low-energy Hilbert space represented by the boundary modes, the symmetry action can only be recognized linearly by combining both boundaries together. When the edges are far apart and the system has an energy gap, local perturbations cannot effect both edge spins simultaneously. Thus, either the edge perturbation breaks the symmetry or the spin-1/2 doublet at each edge remains degenerate up to splittings exponentially small in the system size.

Considering not only local symmetries but also symmetries that relate the physical locations of degrees of freedom, such as the spatial symmetries of rotation or reflection, can lead to an even richer panoply of phases [54, 140, 39, 17, 120, 139]. This has been well explored for the case of band insulators whose non-trivial structure is protected by crystal symmetries [75, 142], which are referred to as non-interacting topological crystalline insulators. However in these cases, the boundary modes often do not appear,

for a simple reason: any possible physical boundary of the system may break the relevant symmetry. In order to distinguish these phases, we will turn to entanglement in the ground state wavefunction.

0.3 Detecting Topological Phases with Entanglement

It has been shown that the features of topological order and symmetry protected topological order manifest in the entanglement properties of the ground state wavefunctions. This was first noted in studies of the entanglement spectrum of fractional Quantum Hall trial wavefunctions, which generally take the form of gapless spectra that mirror the gapless modes on a boundary. [97] In one dimensional SPT phases, the entanglement spectrum features protected degeneracies that signify entanglement that cannot be removed while preserving the symmetry, and can thus be used to establish that the phases are fundamentally distinct from trivial, non-entangled insulators. While the entanglement spectra can signal non-triviality, additional work has shown that entanglement properties beyond the spectra can be used to extract the precise symmetry fractionalization in one dimensional SPT phases [121] and the precise braiding statistics of two dimensional topological phases [80].

Additionally it was shown in the case of one dimensional SPT phases [121] protected by spatial inversion that the non-trivial features can still be extracted from the entanglement spectrum, even though the boundary degeneracy is not guaranteed. This suggests that entanglement can be used for the complete (numerical) identification of topological

phases generally, even when a necessary ingredient for the topological protection is a non-local symmetry operation.

In this thesis, we will explore some problems related to this identification for wavefunctions in two dimensions. For this purpose, we developed numerical tools using the framework of tensor network states, a memory efficient way of representing quantum ground states. In Chapter 1, we study a featureless phase of bosons on the honeycomb lattice and argue that this phase can be topologically protected under any one of several distinct subsets of the crystalline lattice symmetries. We discuss methods of detecting such phases with entanglement and without.

In Chapter 2, we consider the problem of constructing wavefunctions for *intrinsically fermionic* topological phases, i.e. topological phases contructed out of fermions with a nontrivial response to fermion parity defects. A zero correlation length wavefunction and a commuting projector Hamiltonian that realizes this wavefunction as its ground state are constructed. Using an appropriate generalization of the minimally entangled states method for extraction of topological order from the ground states on a torus to the intrinsically fermionic case, we fully characterize the corresponding topological order as Ising $\times$ $(p_x - ip_y)$.

Chapter 1

Tensor Networks for Crystalline SPTs

In this Chapter, we compute the entanglement properties of an insulating state of interacting bosons on the honeycomb lattice, and show that it constitutes a topological phase protected by lattice symmetries. In particular, we show that the non-trivial entanglement is not related just to the group formed by the lattice symmetries, but becomes tied to the specific realization as a honeycomb lattice. Combined with the symmetry, this enforces a non-trivial short-range entanglement structure.

The wavefunction we consider is an insulator of interacting bosons on the honeycomb lattice at a filling of one boson per unit cell, or half filling per site. It forms one example of a class of insulators that require a non-Bravais lattice, i.e. a lattice with multiple sites per unit cell. The necessity for such a non-trivial unit cell arises due to higher-dimensional

generalizations [115, 114, 70, 71] of the Lieb-Schultz-Matthis (LSM) theorem [99],which forbids the existence of a featureless state — a state that neither spontaneously breaks a symmetry, nor displays intrinsic topological order, nor has power-law correlations and is thus "gapless" — in systems with a fractional filling per unit cell. While such a featureless state at half-filling per site is allowed on the honeycomb lattice, the explicit construction is challenging. Symmetry guarantees that a free-fermion spectrum is gapless at certain high-symmetry points, and there is thus no basis of localized, symmetric and orthogonal Wannier states. This implies that a featureless state on the honeycomb lattice cannot be constructed by filling a permanent of localized Wannier orbitals [117], and any construction of a quantum state thus must involve interactions. Ref. [83] pursued an approach of constructing a permanent wavefunction by filling local and symmetric orbitals that are not orthogonal and it was argued that that the resulting wavefunction is indeed featureless. In particular, using numerical simulations it was found that the state exhibits isotropic and exponentially decaying correlations, and arguments were presented that it is not topologically ordered.

Here while we confirm the featureless bulk of the state, including the absence of intrinsic topological order, we show that nevertheless the entanglement of the state cannot be removed while preserving certain symmetries — it is symmetry-protected. The relevant symmetry is a combination of charge conservation and lattice symmetries, which together protect universal features in the entanglement spectrum. In particular, we show that the low-lying entanglement spectrum is to great accuracy described by that of a conformal

field theory with central charge $c = 1$, and that there is an exact double degeneracy throughout the entanglement spectrum for certain geometries, which is protected by the symmetries of the state and thus serves as a topological invariant identifying the SPT order. Since lattice symmetry is involved crucially, this provides one of the first examples for an SPT of interacting bosons protected by lattice rather than on-site symmetries. To further substantiate the robustness of these features, we obtain parent Hamiltonians for the phase in certain quasi-one-dimensional geometries and study the effect of weak symmetry-preserving and -breaking perturbations on the ground states of these Hamiltonians.

All of these features become accessible through a description of the state as a projected entangled-pair state (PEPS) [73, 111, 57, 143]. These states form a specific class of tensor network states that corresponds to a generalization of the well-known matrix-product state (MPS) [153, 43, 116, 136] framework to higher dimensions. PEPS have been shown to be a powerful description of many classes of gapped systems, including topologically ordered and SPT phases. Here, we have an exact description of the state as a PEPS, allowing us to extract properties such as the entanglement spectrum and the topological invariants exactly on certain geometries; we emphasize that these properties of the state are not accessible to other numerical methods.

The topological invariants extracted here form examples of a broad class of invariants that provably must be constant throughout the phase. These differ from the order parameters that measure local symmetry breaking in that they are not related to the

expectation values of local operators. Early examples of topological invariants for SPT phases are the string order parameter for the one-dimensional AKLT phase [1, 2, 37, 120], and the spin Chern number for the quantum spin Hall effect [138]. The invariants we consider here measure how the action of the symmetry is implemented on the physical edge states of open systems or on the Schmidt states of an entanglement decomposition [122]. These invariants feature heavily in the classification of SPT phases with on-site symmetry, and similar invariants that apply to free-fermion states have been used for topological crystalline insulators [55, 75]. In contrast, topological invariants for interacting states protected by lattice symmetries in more than one dimension are poorly understood. We will discuss the action of the symmetry on the edge of the state and progress towards the goal of finding a topological invariant to identify the corresponding phase.

The rest of this chapter is structured as follows: in Section 1.1, we review the honeycomb featureless boson insulator (HFBI) state, and introduce its PEPS representation. In Section 1.2, we discuss results for the correlation functions of this state. In Section 1.3, we discuss the entanglement spectra that we obtain numerically from the PEPS representation and discuss in detail their connection to the spectrum of a free boson conformal field theory. In Section 1.4, we describe the symmetry-protected topological invariants that allow us to identify the symmetries that protect certain entanglement properties of the state in quasi-one-dimensional geometries. Section 1.5 discusses the effect of weak perturbations to a parent Hamiltonian in the same quasi-one-dimensional setup, and Section 1.6 introduces a different perspective on the phase from the point of view of a

boson-vortex duality.

1.1 Construction of the featureless boson insulator

In the honeycomb lattice, each unit cell is associated with exactly one hexagon plaquette, which respects the lattice point group symmetries. As shown in Ref. [83], this provides an explicit construction of a bosonic insulator on the honeycomb lattice that is completely featureless in the bulk, henceforth referred to as *honeycomb featureless boson insulator* (HFBI). The state is succinctly described by the following expression:

$$|\psi\rangle = \prod_{\hexagon} \left(\sum_{i \in \hexagon} b_i^\dagger \right) |0\rangle. \tag{1.1}$$

Here, $\hexagon$ denotes the elementary hexagons of the honeycomb lattice. Despite the deceivingly compact expression, this many-body bosonic state is strongly correlated and requires concrete computation for its properties to be unveiled.

We focus on two closely related variants of this state: a version of soft-core bosons where $b_i^\dagger$ creates a boson on site i and obeys the usual bosonic commutation relations, and a hard-core version of the same state where $b_i^\dagger$ also creates a boson but $(b_i^\dagger)^2 = 0$. In either case, the operator $\sum_{i \in \hexagon} b_i^\dagger$ creates exactly one boson per hexagon; as there is one hexagon per unit cell of two sites of the lattice, the state has one boson per unit cell, or half a boson per site, thus allowing the existence of a featureless state. In the case of soft-core bosons, the maximum number of bosons per site is three.

Ref. [83] examined properties of both the soft-core and hard-core variants of this state.

In the soft-core case, ground-state correlations were mapped to those of a classical loop model on the triangular lattice. A Monte Carlo analysis thereof revealed that the boson Green's function $\langle b_i^\dagger b_j \rangle$ decays exponentially – thereby ruling out the possibility that the many-body wavefunction describes a superfluid – and further, that the correlation functions of a variety of neutral operators (e.g., those describing charge- or bond-density order) remained short-ranged. This loop model mapping also included a variational parameter, m, that tunes the the soft-core boson wavefunction on the honeycomb lattice into that of a trivial Mott insulator on a triangular lattice of fictitious sites placed at the center of each hexagon. The absence of a transition under this perturbation was taken as evidence that the ground state would remain unique on manifolds of nontrivial topology, thereby ruling out the possibility that the wavefunction describes a topologically ordered phase. For the case of hard-core bosons, a different quantum-classical mapping enabled the efficient calculation of boson number correlations. This directly revealed that the hard-core projection did not induce any long-range correlations in the neutral sector. Although working in the number basis precludes direct access to 'charged' correlators such as the boson Green's function, on general grounds, the algebraic decay characteristic of classical 2D superfluids [1] is expected to also infect density-density correlations, and thus their exponential decay provides indirect evidence that the hard-core boson wavefunction also lacks superfluid order. We note that none of these quantum-classical mappings can readily provide insights into the entanglement properties of the wavefunction.

[1] Note that the quantum-classical mappings described map quantum correlations to classical ones *in the same dimension.*

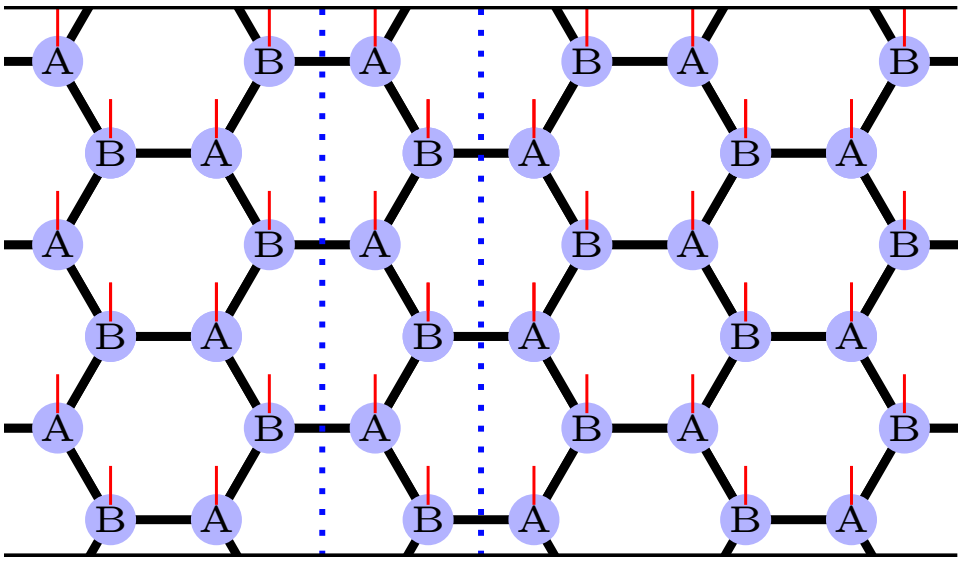

Figure 1.1: Honeycomb lattice PEPS and zig-zag entanglement cut. In this PEPS of rank-4 tensors, the top and bottom edges are identified, forming a cylinder with circumference $W = 3$ unit cells. A one-dimensional MPS representation is constructed by contracting the tensors in each cylinder slice (region marked by dotted lines). The entanglement cut used (either one of the dotted lines) passes through the hexagon mid-points, preventing the tight-binding lattice from gaining additional sites as long as crystalline symmetries are preserved.

1.1.1 PEPS representation

In order to go beyond the properties accessible via these quantum-classical mappings of the HFBI, and in particular in order to be able to study its edge properties, we now derive a representation as a projected entangled pair state (PEPS). Importantly, this PEPS description will respect all of the relevant symmetries of Eq. (1.1).

To obtain a PEPS construction, we first choose a local basis $|n\rangle$ of boson occupation numbers, i.e. $b^\dagger b|n\rangle = n|n\rangle$. The PEPS will thus describe the coefficients of $|\psi\rangle$ in this basis, $\langle n_1 \dots n_L|\psi\rangle$. The PEPS representation is most easily obtained in a two-step construction, where we first construct the state shown in Fig. 1.2. Here, the tensor

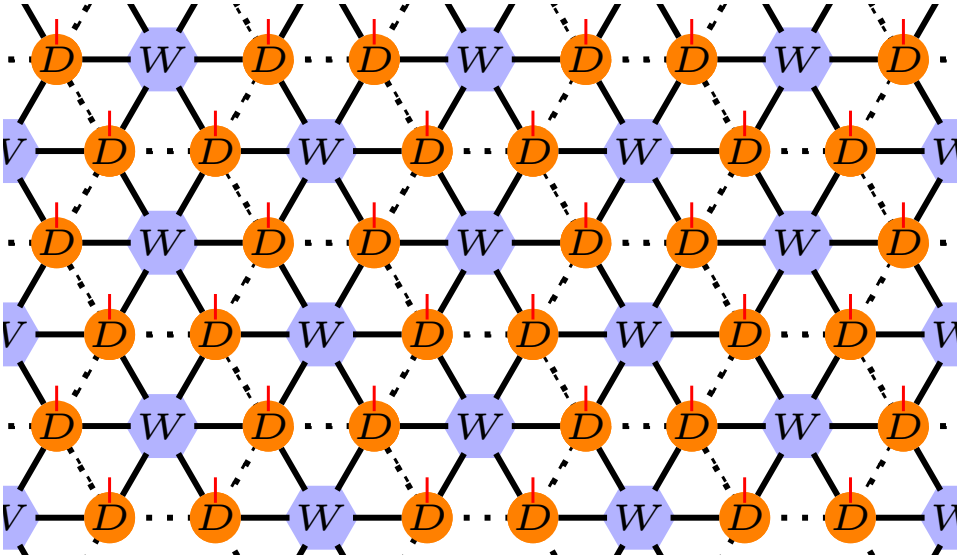

Figure 1.2: Intermediate tensor network for HFBI state. Here, the tensors labeled D are located on the sites of the honeycomb lattice, while the tensors labeled W are located on the centers of each hexagon. Dotted lines thus represent the physical lattice, while the solid lines indicate auxiliary bonds over which the tensor network is contracted.

labeled $W = W^{n_1 \ldots n_6}$, which is placed in the center of each hexagon, is a rank-6 tensor given by

$$W^{n_1 \ldots n_6} = \begin{cases} 1: & \sum_i n_i = 1 \\ 0: & \text{else} \end{cases} , \tag{1.2}$$

where each $n_i \in \{0, 1\}$.

This tensor describes the coefficients of a so-called W-state in the occupation number basis, i.e. $W^{n_1 \ldots n_6} = \langle n_1 \ldots n_6 | \sum_{i=1}^{6} b_i^\dagger |0\rangle$. We note that this tensor is symmetric under permutations of its indices.

On the sites of the physical lattice, we have placed a rank-4 tensor denoted as D, shown in panel (a) of Fig. 1.3(a), which connects the W tensors from three adjacent hexagons, and as fourth index has a physical index p. For a state of soft-core bosons,

where $p = 0, 1, 2, 3$, this tensor is given by

$$D^{\mathrm{sc}}_{p,i_0 i_1 i_2} = \begin{cases} \sqrt{p!} & : \quad p = i_0 + i_1 + i_2 \\ 0 & : \quad \text{else} \end{cases} . \tag{1.3}$$

We can also encode a state of hard-core bosons by replacing D by

$$D^{\mathrm{hc}}_{p,i_0 i_1 i_2} = \begin{cases} 1: & p = i_0 + i_1 + i_2 \leq 1 \\ 0: & \text{else} \end{cases} . \tag{1.4}$$

Other values for the D and W tensors that respect the charge and lattice symmetries can also give rise to featureless insulators. Some of these variants are described in Appendix 1.9.

This tensor network wavefunction manifestly respects all the translational and point group symmetries of the honeycomb lattice, since the tensors W and D are invariant under rotations of their virtual indices in the plane. One can also check that the wavefunction is $U(1)$ invariant with charge 1 per plaquette.

In order to convert the tensor network of Fig. 1.2 into a PEPS representation, we first factor the W-tensor into a matrix-product state of six tensors as shown in Fig. 1.3(b). We choose a form of the MPS that breaks the rotational symmetry of the W-state (which appears as translational symmetry of the MPS). This allows us to obtain an MPS description with a small bond dimension of $M = 2$; a fully symmetric choice would require bond dimension 6. Since these states are physically equivalent, all physical quantities are unaffected by this choice. One possible decomposition is given by

$$W^{i_1 i_2 i_3 i_4 i_5 i_6} = \sum_{\alpha_1 \ldots \alpha_5} V^{i_1}_{\alpha_1} W^{i_2}_{\alpha_1 \alpha_2} \ldots W^{i_5}_{\alpha_4 \alpha_5} X^{i_6}_{\alpha_5} \tag{1.5}$$

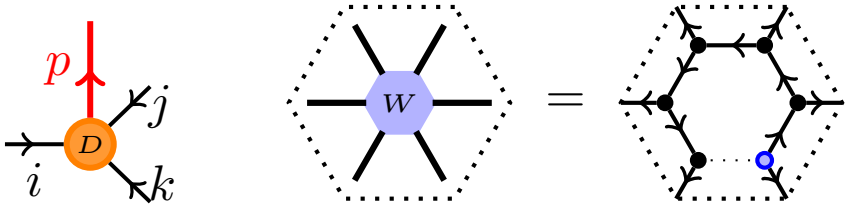

(a) D tensor (b) W-tensor and factored form

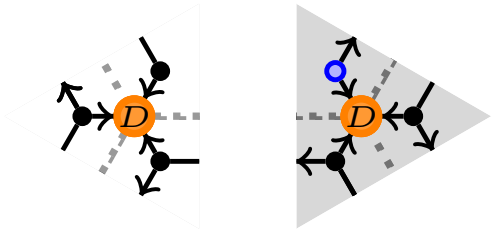

(c) A tensor (d) B tensor

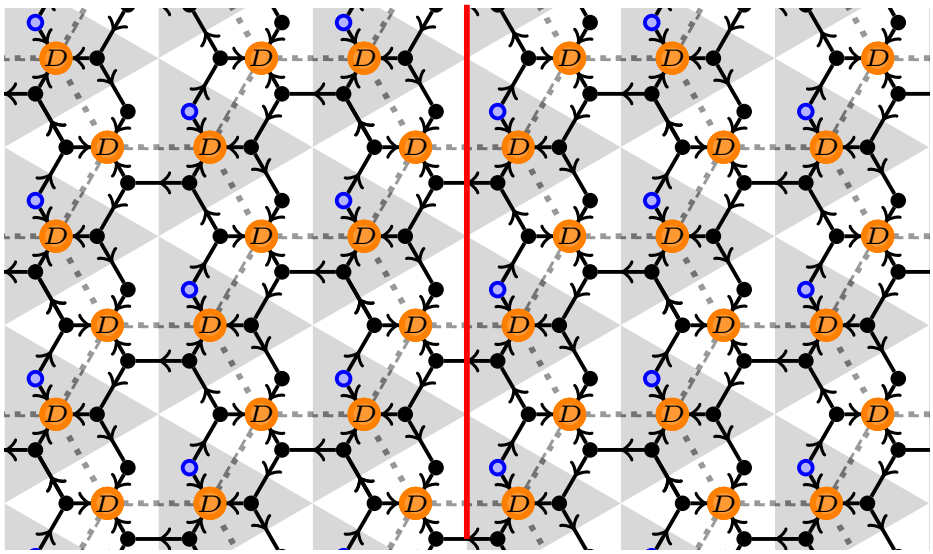

(e) PEPS tensor network for F.B.I. state

Figure 1.3: Construction of PEPS for HFBI state. The site tensors (shown in panels (c), (d)) are constructed using the factors of the plaquette tensor W (panel (b)) combined with the original vertex tensor D (panel (a)). The red line in panel (e) shows where the entanglement cut considered in this chapter crosses the network.

where $V^{i_1}_{\alpha_1} = \delta_{i_1,\alpha_1}$, $X^{i_6}_{\alpha_5} = \delta_{i_6,\alpha_5+1} + \delta_{i_6,\alpha_5-1}$, and

$$W^{j}_{i_0 i_1} = \begin{cases} 1 & : i_0 + j = i_1 \\ 0 & : \text{else} \end{cases},$$

where each index takes values in $\{0, 1\}$. Applying this to each W-tensor yields the state as shown in Fig. 1.3(e). By contracting the four tensors in each shaded region together, we obtain a PEPS in the regular form as shown in Fig. 1.1. The resulting PEPS has a bond dimension of $M = 2$ on the horizontal bonds, and a bond dimension of $M = 4$ on all other bonds. While it superficially breaks the rotational symmetry of the lattice, it is an exact representation of the FBI state and does not break any symmetries after contracting the indices.

This decomposition respects the physical $U(1)$ charge conservation symmetry in that all tensors are separately $U(1)$-invariant [14]. To make this manifest, we have indicated in Fig. 1.3 arrows on each bond that show the flow of charge.

1.1.2 Representation on infinite cylinders

For the calculations presented in this manuscript, we consider the state $|\psi\rangle$ on a cylinder of infinite length, but finite circumference of W unit cells. In Fig. 1.1, we have indicated the choice of boundary conditions for the cylinder used in this chapter. For many practical purposes, the PEPS on an infinite cylinder can be represented as an infinite, translationally invariant matrix-product state of bond dimension $\chi = 2^W$ and physical dimension $p = 4^{2W}$ ($p = 2^{2W}$) for the soft-core (hard-core) case. The MPS is created by blocking all tensors in each slice of the cylinder, as shown in Figure 1.1.

With each cylinder slice blocked together and considered as an MPS, the procedures we use for computing both correlation functions and entanglement properties are in principle identical to those used previously in MPS [34, 122]. Due to the exponential increase in the MPS bond dimension, this numerically exact approach scales exponentially in the circumference of the cylinder. It is however computationally advantageous to exploit the additional structure present in the PEPS transfer operator; by doing so, we can compute correlation functions and the entanglement spectrum for the cut shown in Figure 1.3(e) for the HFBI state on cylinders of circumference up to $W = 10$. These computations are presented in the following Sections 1.2 and 1.3.

1.2 Correlation functions

In Ref. [83], certain real-space correlation functions of the featureless boson insulator state were studied using a mapping to a particular classical statistical mechanical system which was sampled using Monte Carlo techniques. Here, we go beyond this by employing PEPS calculations on infinite cylinders that allow us to measure a broader class of correlation functions and, in particular, allow us establish a strict upper bound on the exponential decay of *all* two-point correlation functions for an infinite cylinder of given width.

In Fig. 1.4, we show both density-density and off-diagonal short-range correlation functions for a cylinder of circumference $W = 8$. Comparing these to the Monte Carlo results of Ref. [83], which have been computed for a different geometry, we find good qualitative agreement. Crucially, while the boundary conditions we choose break the

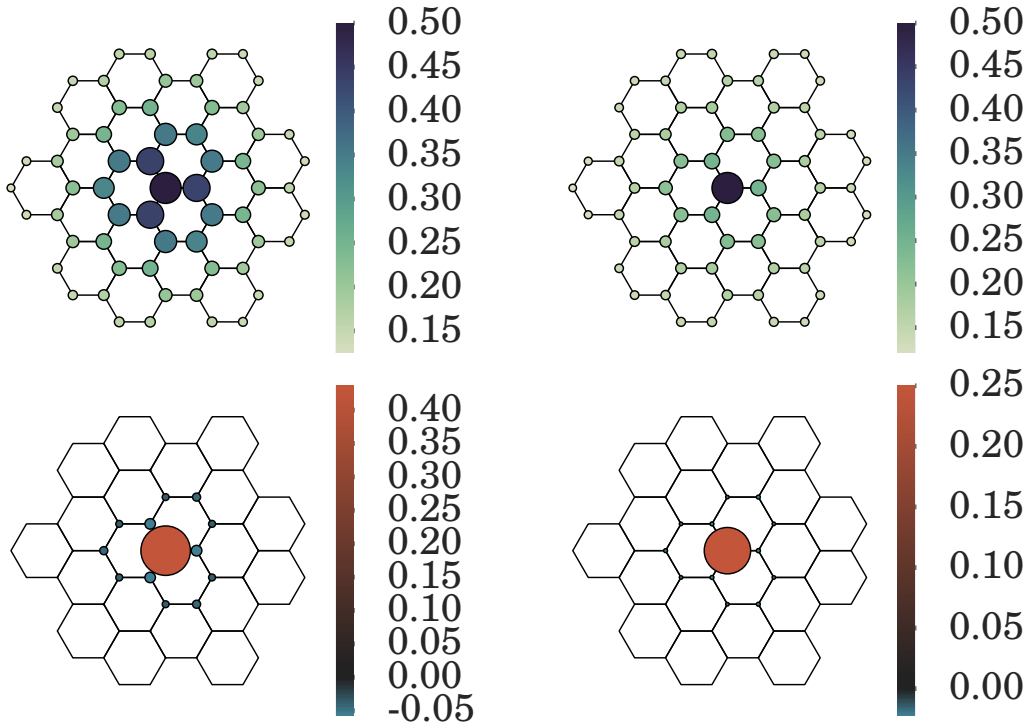

Figure 1.4: Short distance correlation functions $\langle b_0^\dagger b_x \rangle$ (top panels) and $\langle (n_0 - \frac{1}{2})(n_x - \frac{1}{2}) \rangle$ (bottom panels) for the soft-core HFBI (left panels) and the hard-core HFBI (right panels) on the $W = 8$ cylinder. The magnitude of the correlation function at site x is proportional to the radius of the corresponding circle.

rotational symmetry by making the system periodic in one direction and infinite in the other, the short-range correlations for distances up to half of the cylinder circumference appear unaffected by this.

It is a well-known result that PEPS can, in the thermodynamic limit, exhibit power-law correlation functions [144], while the correlation functions in an MPS of finite bond dimension decay exponentially. The long-range correlations of an MPS are encoded in its transfer operator T, which for an MPS of bond dimension M is a matrix of size $M^2 \times M^2$. Denoting the spectrum of T as λ_i with $|\lambda_0| \geq |\lambda_1| \geq \ldots$, we can normalize the state such that $\lambda_0 = 1$. If the largest eigenvalue is found to be non-degenerate, $\lambda_1 < \lambda_0$, we have that all correlation functions of operators $\mathcal{O}_i$ that are supported on a finite number of sites centered around a site i decay as $\langle \mathcal{O}_i \mathcal{O}_j \rangle - \langle \mathcal{O}_i \rangle \langle \mathcal{O}_j \rangle \sim e^{-|i-j|/\xi_{\mathcal{O}}}$. Crucially, the correlation length $\xi_{\mathcal{O}}$ for any operator $\mathcal{O}$ is bounded from above by $-1/\log|\lambda_1|$ [135]. In the following, we thus evaluate the spectrum of the transfer operator of our PEPS along cylinders of varying circumference W to establish an upper bound on the correlation length for each circumference $\xi(W)$ Note that the possibility of having power-law correlations in a PEPS can be reconciled with the above consideration if the correlation length $\xi(W)$ diverges as $W \to \infty$; we will thus need to carefully consider the scaling of $\xi(W)$.

Our results for the correlation bounds $\xi(W)$ are shown in Fig. 1.5. Here, we show the upper bound for the case of soft-core and hard-core bosons, and in each case consider the spectrum of the full transfer operator as well as $S^z = 0$ sector, which encodes correlations of operators $\mathcal{O}_i$ that do not change the boson number (such as density-density

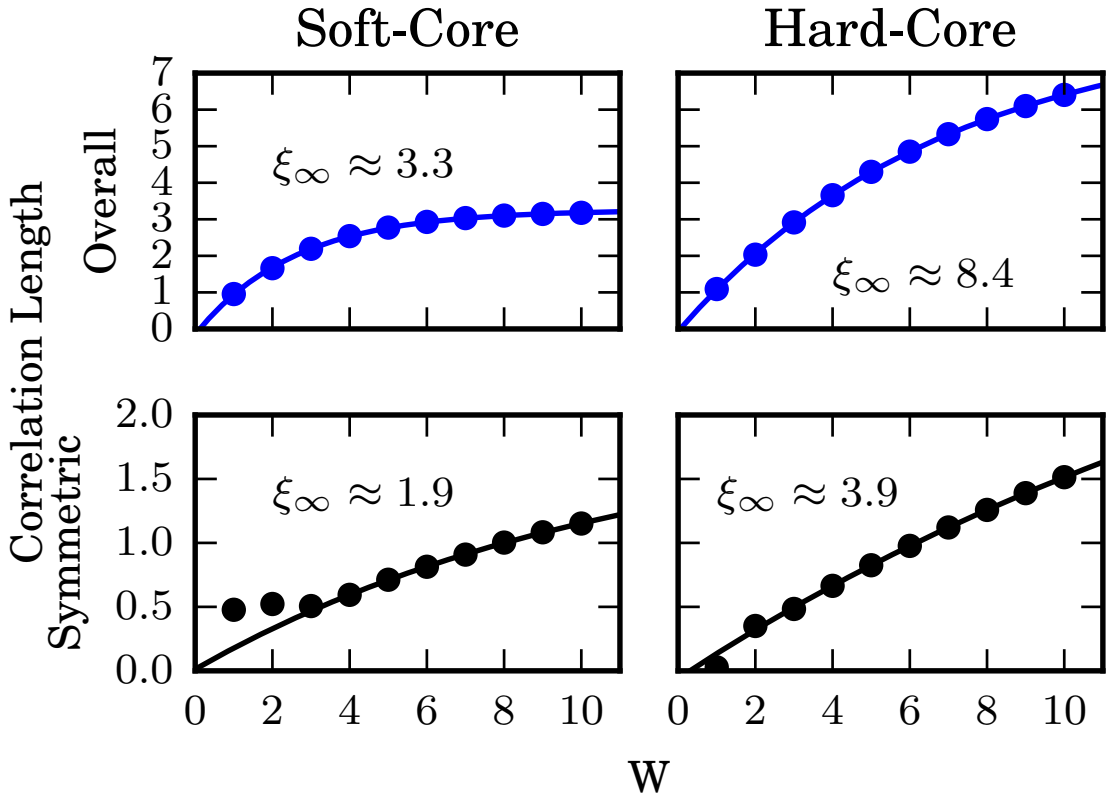

Figure 1.5: Bound on the correlation length of all operators and $U(1)$ symmetric operators respectively for the soft-core and hard-core states vs. cylinder circumference W. Fits of the form $\xi = \xi_\infty - Ae^{-W/B}$ were used to extract the correlation lengths. These bounds can be confirmed to match the correlation lengths of $\langle b_x^\dagger b_y \rangle$ and $\langle n_x n_y \rangle$ in each case.

correlations). We find that in each case, the largest eigenvalue of the transfer operator is non-degenerate. Furthermore, we find that the correlation length approaches a finite constant as we increase W, as shown in Figure 1.5.

1.3 Entanglement spectrum

Here, the entanglement spectrum ε_i is defined through the spectrum ρ_i of the reduced density matrices $\rho_{L/R}$ obtained for a bipartition of the state, where we have $\varepsilon_i = -\log \rho_i$. The corresponding eigenvectors of the reduced density matrices are referred to as Schmidt states $|\psi^{(i)}_{L/R}\rangle$. The Schmidt decomposition

$$|\psi\rangle = \sum_i \sqrt{\rho_i} |\psi^{(i)}_L\rangle |\psi^{(i)}_R\rangle \tag{1.6}$$

relates the Schmidt states to the original wavefunction.

The quasi-1D cylinder geometry is convenient for calculating the entanglement spectrum for entanglement cuts transverse to the long direction of the cylinder. To extract the entanglement spectrum exactly, we use a method proposed in Ref. [34]. In the setup given here, the exact representation of the HFBI state as a PEPS of fixed bond dimension implies an upper bound on the number of non-zero ρ_i; for the cut shown in Fig. 1.3(e), this upper bound is $\chi = 2^W$.

Upon computation of the entanglement spectrum, we find that this bound is saturated, so that there are precisely 2^W contributing terms in Eq. 1.6. This fact can be simply understood without reference to the PEPS representation: Each of the w plaquettes on the cut can contribute its one boson either to the left or the right of the cut, and

this is the complete source of the uncertainty of the state on one half of the cut when ignoring the state on the other half.

We can form a set of 2^W vectors $|\sigma_1, \ldots, \sigma_W)$ that correspond to the choices for the auxiliary degrees of freedom of the PEPS across the cut, where $\sigma_i \in \{0, 1\}$ is the number of bosons contributed by the i'th hexagon the left of the cut. The PEPS defines a map from these boundary vectors to physical states in the bulk of the semi-infinite cylinder, which we denote as $|\psi_L^{(\sigma_1,\ldots,\sigma_W)}\rangle$; on the subspace of physical states spanned by Schmidt states with non-vanishing contribution to the reduced density matrix, this map is invertible and can be computed explicitly.

Translation around the cylinder acts in the natural way on the states $|\psi_L^{(\sigma_1,\ldots,\sigma_W)}\rangle$ by permuting the values of σ_i, $\sigma_i \to \sigma_{i+1}$. Although the boson number on the half-infinite cylinder is infinite, we can define for each basis element a $U(1)$ charge corresponding to the number of bosons to the left of the cut relative to a uniform background charge,

$$Q_L = \sum_i (\sigma_i - \frac{1}{2}). \tag{1.7}$$

Only relative charges between states will be important for our conclusions, and the precise way in which background charge is accounted for does not matter. Each state is paired with a corresponding state on the right half of the cylinder with opposite charge.

We can block-diagonalize the reduced density matrix for a half-infinite cylinder in both the $U(1)$ charge and transverse momentum quantum numbers, allowing us to perform more efficient calculations. In addition, we can assign quantum numbers to both the Schmidt states and the entanglement spectrum. This property is generically true for

$U(1)$-symmetric and translationally invariant PEPS on a cylinder, although not in general true for arbitrary symmetry groups. This point is elaborated on in Section 1.4.2.

The entanglement spectra for the HFBI on cylinders with even and odd width circumferences are shown in Fig. 1.6, plotted against the transverse momentum eigenvalue and colored by the $U(1)$ charge eigenvalue of the corresponding Schmidt states. All the numerical results in this section are obtained for the soft-core boson variant of the state. We find that the entanglement spectrum looks like it has a gapless edge mode with linear dispersion near momentum zero. To further substantiate this, we compare the lowest entanglement energies for several cylinder widths and quantum number sectors in Fig. 1.7. The finite-size scaling confirms in all cases that the entanglement gap closes as $1/W$, as one would expect for a gapless mode with linear dispersion.

The gapless edge is suggestive of the state having either topological or SPT order. While topological order was already ruled out in Ref. [83], our PEPS representation gives us additional tools to substantiate this assertion. In particular we can calculate the entanglement between the two parts of the cylinder as a function of circumference $S(W)$ and check for a subleading term to the area law by performing a fit to $S(W) = \alpha W + S_0$. In a topological phase and in one of the minimally entangled states (MES) [159], one would expect the subleading term to correspond to the topological entanglement entropy, $S_0 = -\gamma$ [88, 95, 80]. In a non-minimally entangled state, one would instead measure other values of $S_0 > -\gamma$. However, since each MES exhibits long-range order of a specific Wilson loop operator, such a superposition of MES represents a superposition of different

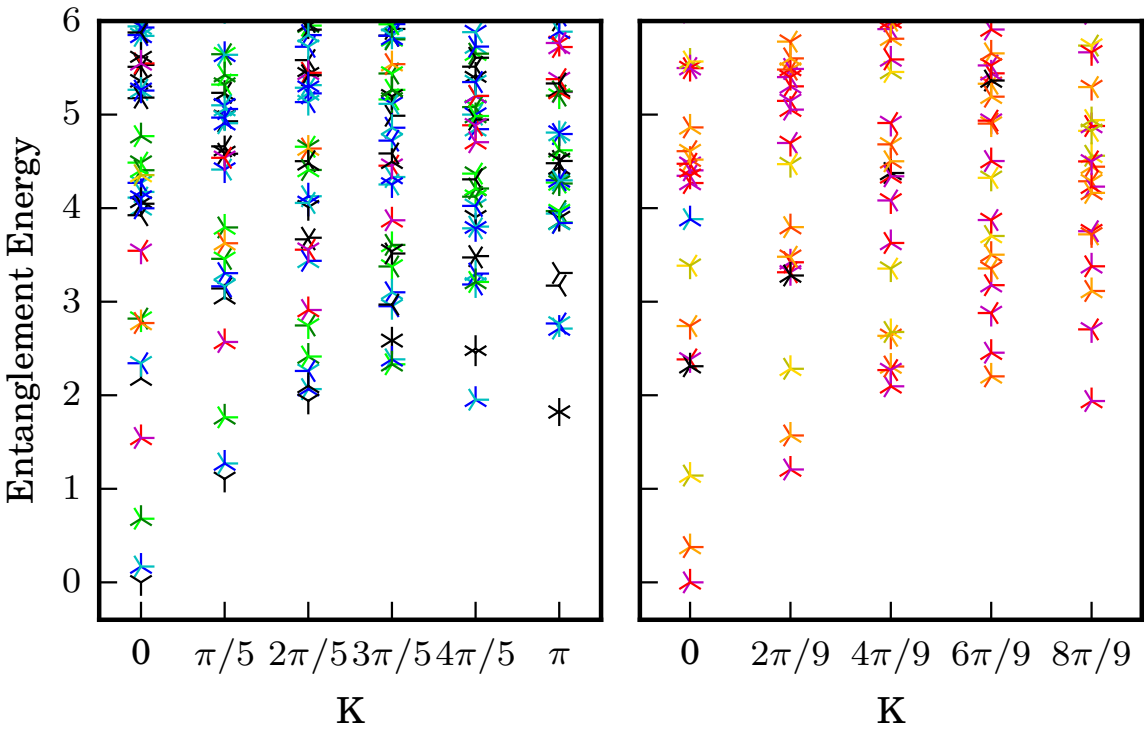

Figure 1.6: Entanglement spectrum on the zig-zag edge of a cylinder of circumference $W = 10$ (left panel) and $W = 9$ (right panel), as function of transverse momentum K_y. Different colors indicate different $U(1)$ charge sectors.

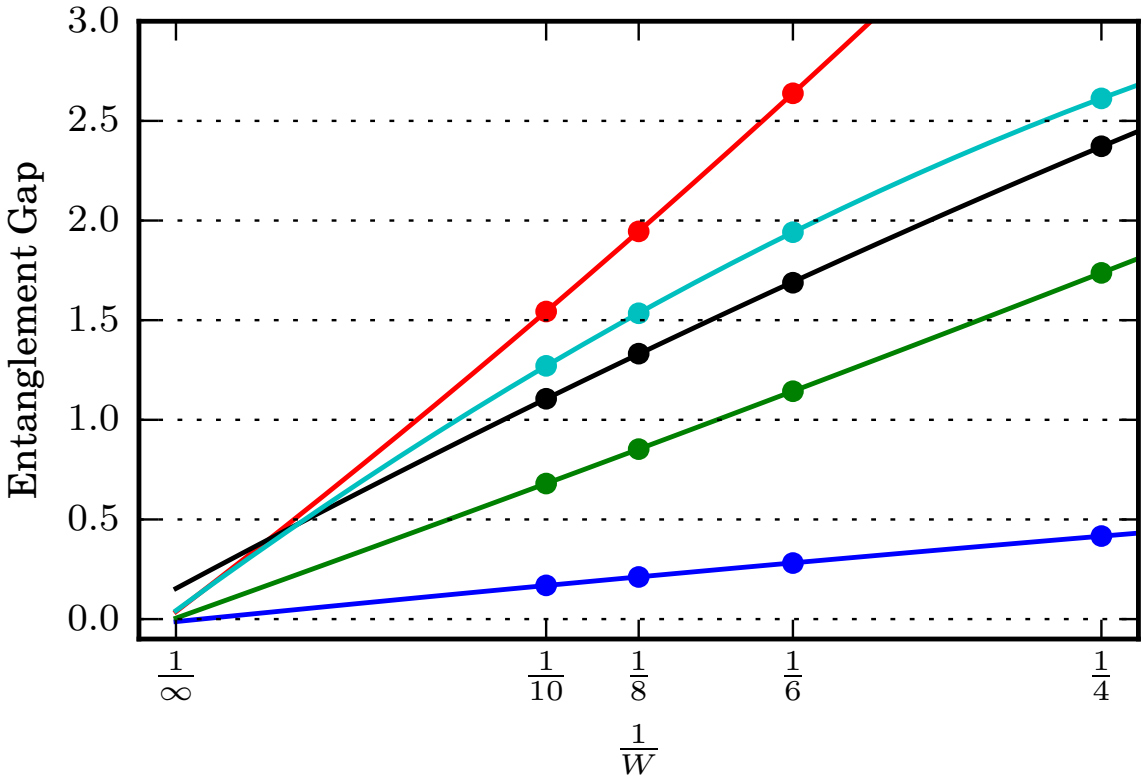

Figure 1.7: The lowest five states above the ground state in Figure 1.6 show gapless $1/W$ scaling behavior. In this plot, fits for the entanglement energy versus $1/W$ (of the form $a + \frac{b}{W} + \frac{c}{W^2}$) to extract the gap are consistent with a gap value of 0.

ordering patterns and can thus be detected via a degeneracy of the largest eigenvalue of the transfer matrix. Our results for the entropy are shown in Fig. 1.8. We find results that are consistent with $S_0 = 0$, which together with the fact that we also find that the transfer matrix to be nondegenerate rules out topological order.

1.3.1 Conformal field theory description of the edge

In addition to the gapless behavior, we find that the low energy entanglement spectrum can be completely described by the finite-size spectrum of a conformal field theory (CFT).

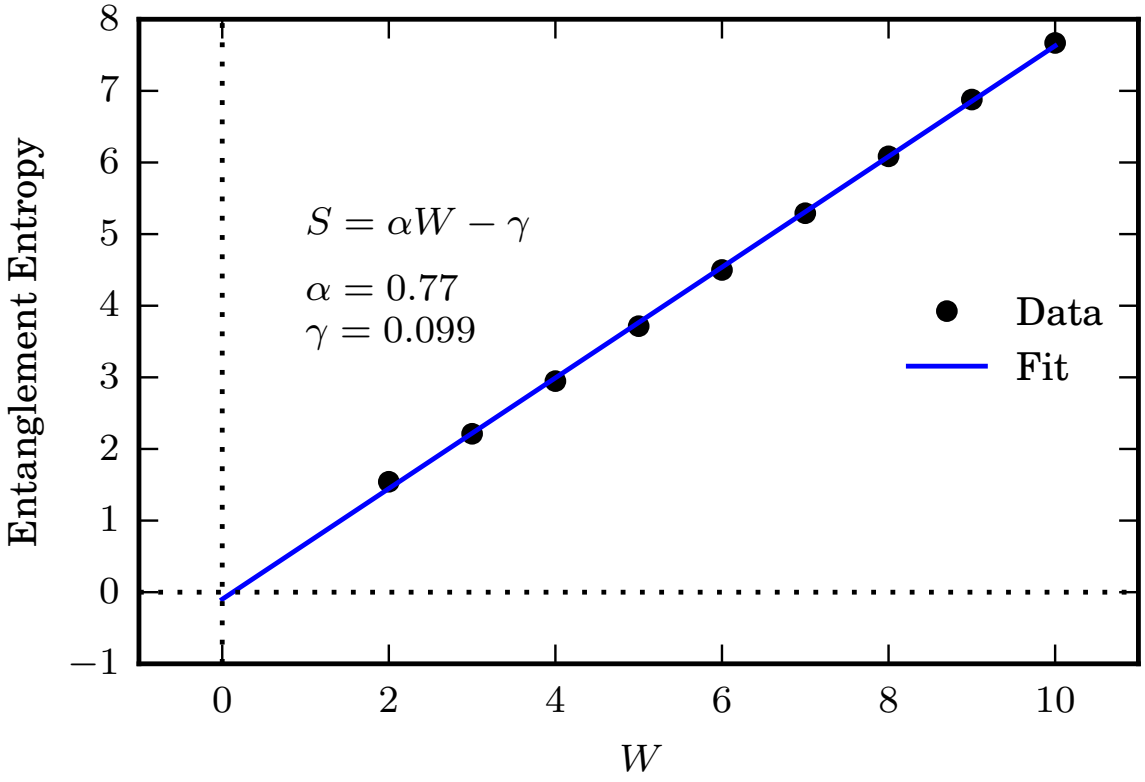

Figure 1.8: The constant correction to the entanglement entropy, which measures the topological entanglement entropy γ when the state is minimally entangled, is consistent with 0.

Given the $U(1)$ symmetry of the state, the simplest possible conformal field theory we might expect to appear at the edge is that of a single free bosonic field - and indeed, this is the CFT that matches the entanglement spectrum. We briefly review the relevant properties of this CFT [49].

The free boson CFT is created from the Lagrangian

$$\mathfrak{L} = \frac{g}{2} \int dt \int_0^W dx \left[(\partial_t \phi)^2 - (\partial_x \phi)^2 \right] \tag{1.8}$$

with the compactified field identification

$$\phi \equiv \phi + 2\pi R$$

and placed on a circle of circumference W with periodic boundary conditions

$$\phi(x) \equiv \phi(x + W).$$

The family of free-boson CFTs is parametrized by a single parameter $\kappa = \pi g R^2$, also known as the Luttinger liquid parameter [49, 58].

Upon canonical quantization, we find that the set of energy eigenstates consists of $U(1)$ Kac-Moody primaries $|e, m\rangle$, with integers e, m labeling the $U(1)$ charge and the winding number of the bosonic field respectively, and level $n, \bar{n}$ descendants of each primary for non-negative integers $n, \bar{n}$, which we will collectively label $|e, m; n, \bar{n}\rangle$. The number of level $(n, \bar{n})$ descendants of a given primary, all of which are degenerate in the thermodynamic limit, is $Z(n)Z(\bar{n})$, where $Z(n)$ is the number of partitions of the integer n.

The energies and momenta for the states $|e, m; n, \bar{n}\rangle$ are given below on a finite size system of circumference W:

$$\begin{aligned} \mathbf{P} &= \frac{2\pi}{W}(em + n - \bar{n}) \\ \mathbf{H} &= \frac{2\pi}{W}(\frac{e^2}{4\kappa} + \kappa m^2 + n + \bar{n}) + \dots \end{aligned} \tag{1.9}$$

Here, the ellipsis $(\dots)$ denotes further subleading contributions due to coupling to irrelevant operators.

By rescaling the energy and momentum, we find a system-size independent pattern that can be matched to the low-energy, linearly dispersing part of the entanglement

spectrum from Figure 1.6:

$$\begin{aligned} \mathbf{P} &\propto (em + n - \bar{n}) \\ \mathbf{H} &\propto e^2 + 4\kappa^2 m^2 + 4\kappa(n + \bar{n}) + \dots \end{aligned} \tag{1.10}$$

The results of this match are shown in Figure 1.9. An estimate for κ can be obtained from the energy of the first descendent $|0, 0; 1, 0\rangle$, which gives $\kappa \approx 1.6$. The label e, which measures the $U(1)$ charge, is integer for even W and half-integer for odd W. The degeneracy pattern $1, 1, 2, ...$ for the level-$(n, 0)$ descendents along the edge of the cone matches the prediction.

The states with odd winding number m, such as $|0, \pm 1\rangle$, do not appear at the energy and momentum predicted by the above formula. Instead, the primary states $|e, m = \pm 1\rangle$ can be found centered around momentum $K = \pi$. The identification of these states in the spectrum is shown in Figure 1.10. Although the larger-m states are too high in energy to be reliably distinguished at this system size, a natural conjecture is that all primaries with odd m will appear around momentum π. (This is a standard side-effect of lattice regularization.)

Given the PEPS representation, we can express the entanglement Hamiltonian H_L for the left semi-infinite cylinder, defined via $\rho_L = \exp(-H_L)$, as a Hamiltonian acting on the auxiliary degrees of freedom of the PEPS crossing the cut, which we have denoted as $|\sigma_1, \dots, \sigma_W)$. We expect this Hamiltonian to encode the universal properties of the edge CFT, which should be invariant under local gauge choices in the PEPS. Its ground

state is (up to normalization) given as

$$|\Psi_0) = \sum_{\sigma_1,\ldots,\sigma_W} \langle \Psi^{(\sigma_1,\ldots,\sigma_W)} | \Psi_L^{(0)} \rangle |\sigma_1,\ldots,\sigma_W). \tag{1.11}$$

In Fig. 1.11, we show the bipartite von Neumann entanglement entropy of this state for a cut into l and $W-l$ sites, which confirms the central charge $c=1$ of the edge CFT. A similar construction was considered in [101].

1.4 Symmetry protection

1.4.1 Overview

While the gapless entanglement spectrum observed above is consistent with a symmetry-protected topological phase, it does not by itself guarantee the presence of such a robust phase, and does not allow us to infer which symmetries are protecting the topological properties of the phase. A key observation that allows us to make progress on these crucial questions is that many points in the entanglement spectrum are degenerate. In particular, we find that for cylinders of odd circumference, the entire spectrum is doubly degenerate.

In this section, we will discuss how the corresponding degenerate Schmidt states are related through the action of a symmetry of the HFBI wavefunction. As discussed in Ref. [122] and reviewed in the Section 1.4.2, this symmetry action can be used to diagnose one-dimensional symmetry protected topological order, for which the degeneracy throughout the entire entanglement spectrum is a robust feature. We will demonstrate

that the odd circumference cylinders, considered as quasi-one-dimensional states, are indeed SPTs protected by a combination of lattice inversion and charge parity symmetries.

1.4.2 Symmetry protection of the HFBI

While the Schmidt eigenstates are uniquely defined for non-degenerate eigenvalues of the reduced density matrix, they are not unique when the spectrum is degenerate and any choice of orthonormal states in the degenerate subspace represents a valid choice of Schmidt states. Applying a unitary transformation V^{ji}, which respects $\sum_i V^{ji}(V^{ki})^* = \delta_{jk}$, on the left Schmidt states must be accompanied by an appropriate transformation $(V^{ji})^*$ applied to the right Schmidt states.

In particular, this allows the action of an on-site symmetry (or more generally, any symmetry which commutes separately with the reduced density matrices for the left and right half) to mix Schmidt states corresponding to degenerate eigenvalues. The action of such a symmetry operator U_g takes the form

$$\begin{aligned} U_g|\psi_L^{(i)}\rangle &= \sum_j |\psi_L^{(j)}\rangle V_g^{ji} \\ U_g|\psi_R^{(i)}\rangle &= \sum_k |\psi_R^{(k)}\rangle \left(V_g^{ki}\right)^*, \end{aligned} \tag{1.12}$$

where the V_g^{ji} are unitary matrices that only act on degenerate blocks of Schmidt states. Crucially, Ref. [122] describes a numerical procedure to calculate V_g for an on-site symmetry g within the MPS formalism, which we review in Section 1.4.2.

We can also analyze the effects of symmetries that preserve the entanglement cut but swap the left and right halves of the cylinders. In general, we will consider any symmetry

h that swaps the cylinder sides and squares to the identity, which we will call an inverting symmetry. These satisfy a modification of Eq. (1.12):

$$\begin{aligned} U_h|\psi_L^{(i)}\rangle &= \sum_j |\psi_R^{(j)}\rangle V_h^{ji} \\ U_h|\psi_R^{(i)}\rangle &= \sum_k |\psi_L^{(k)}\rangle \left(V_h^{ki}\right)^* . \end{aligned} \tag{1.13}$$

Note here that the left and right Schmidt states are exchanged in the transformation. We can introduce a map S that acts as

$$S|\psi_R^{(i)}\rangle = |\psi_L^{(i)}\rangle. \tag{1.14}$$

Since a change in phase $|\psi_R^{(i)}\rangle \to e^{i\varphi}|\psi_R^{(i)}\rangle$ must be accompanied by the complex conjugate $|\psi_L^{(i)}\rangle \to e^{-i\varphi}|\psi_L^{(i)}\rangle$ to preserve the Schmidt decomposition, S is antiunitary.

Combining the above, we see that

$$U_h S|\psi_R^{(i)}\rangle = \sum_j |\psi_R^{(j)}\rangle V_h^{ji} \tag{1.15}$$

defines the action of the operator $U_h S$ on the right Schmidt states (of course an equivalent action can be defined on the left Schmidt states). Since S is anti-unitary, the combined action of $U_h S$ is also anti-unitary. Together with the requirement that the symmetry squares to the identity, one finds that (where $\mathbf{K}$ represents complex conjugation in the canonical basis)

$$V_h V_h^* = (V_h \mathbf{K})^2 = e^{i\phi_h} I = \pm I, \tag{1.16}$$

that is the inverting symmetry forms an anti-unitary projective representation of $\mathbb{Z}_2$.

The collection of V_g for on-site symmetries sometimes fail to satisfy the group multiplication laws, i.e. one may find $V_{g_1 g_2} \neq V_{g_1} V_{g_2}$. Instead, they may form a projective

representation, where group multiplication laws are obeyed up to phases $\omega(g_1, g_2)$, i.e. $V_{g_1}V_{g_2} = \omega(g_1, g_2)V_{g_1 g_2}$. Certain combinations of these phases, such as

$$e^{i\phi_{g_1,g_2}} \equiv \frac{\omega(g_1, g_2)}{\omega(g_2, g_1)} \tag{1.17}$$

whenever $[g_1, g_2] = 0$, are *symmetry protected topological invariants*, which take discrete values and hence cannot be changed continuously. Thus, $\phi_{g_1,g_2} \neq 0$ signifies that the entanglement degeneracy cannot be removed without breaking the symmetry or going through a phase transition. Similarly, for the inverting (anti-unitary) symmetries h, the phase $\phi_h = \pi$ in Eq. (1.16) signifies that the degeneracy cannot be removed without breaking the symmetry [122].

Projective Representations on the edge of MPS

We can use the formalism of matrix-product states to determine the action of physical symmetries on the Schmidt states. First, this will lead to the assignment of charge and translation (which both act on-site in the MPS representation) quantum numbers to the Schmidt states and corresponding entanglement spectrum as labeled in, e.g., Fig. 1.6. Secondly, this will be used to numerically extract the topological invariants discussed in Section 1.4. We now review this formalism briefly, including a discussion of the method that allows us to numerically determine the symmetry action of inversion symmetry on the Schmidt states. Both of these discussions follow Ref. [122].

We start by finding tensors Γ, Λ representing the so-called canonical form of the MPS,

as detailed in Refs. [145, 147]:

$$|\psi\rangle = \sum_{\{p_i\}} \ldots \Lambda\Gamma_{p_0}\Lambda\Gamma_{p_1}\Lambda\Gamma_{p_2}\Lambda \ldots |...p_0p_1p_2...\rangle. \tag{1.18}$$

This canonical form provides the Schmidt decomposition at each site in the lattice. Here, each physical leg of the MPS represents all $2W$ physical sites on a cylinder slice, and each virtual leg represents all virtual indices that connect cylinder slices; the bond dimension of the MPS is thus 2^W. The change of basis to canonical form generally mixes the Hilbert spaces from these virtual legs, so the resulting basis won't be local around the circumference of the cylinder.

For each on-site symmetry of the wavefunction $U_g = \otimes_i u_g^i$, with $U_g|\psi\rangle = e^{i\Theta_g}|\psi\rangle$, there is an operator V_g that acts on the virtual leg of the MPS and satisfies the equation

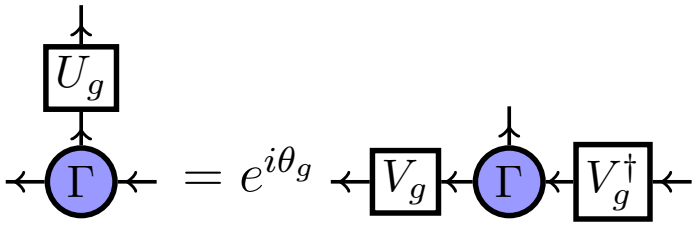

(1.19)

This equation can be rewritten and solved as an eigenvector problem; for an MPS with a nondegenerate largest transfer matrix eigenvalue, this equation is guaranteed have a unique solution where the eigenvalue $e^{i\theta_g}$ is the largest eigenvalue of the eigenvector problem. These solutions V_g have two important properties: they are only defined up to a phase, and they are guaranteed to commute with the diagonal matrix Λ of Schmidt weights.

Due to the first property, these operators are not guaranteed to obey the group

multiplication laws, i.e. one could find situations where

$$V_g V_h = \omega(g,h) V_{gh}. \tag{1.20}$$

It is not always possible to absorb these phases into the definitions of the V_g; in those cases, the V_g do not form a linear representation of the group but rather a projective representation. The set of equivalent classes of phases $\omega(g,h)$ under redefinitions $V_g \to \alpha(g)V_g$ is called $H^2(G, U(1))$, the second group cohomology with $U(1)$ coefficients.

For all the groups discussed in this chapter, the group cohomology classes are labeled by elements of a discrete abelian group. These discrete classes cannot be connected to each other continuously without undergoing a bulk phase transition or breaking the symmetry. Additionally, the classification of projective representations for the on-site symmetry group $U(1) \times \mathbb{Z}_W$ representing charge and translation around the cylinder is trivial. Thus, these edge symmetries can be taken to act linearly, and all Schmidt states can always be simultaneously assigned charge and momentum eigenvalues, as in Figure 1.6.

The second property guarantees that the V_g only mixes exactly degenerate Schmidt states. The action of V_g must have the same phases $\omega(g,h)$ on each degenerate block of Schmidt states, so the projective representation can be nontrivial on any block only if every Schmidt state throughout the entire spectrum is degenerate. The degeneracy will be protected by the symmetry if and only if the V_g form a nontrivial projective representation. Therefore this 1D SPT analysis can only potentially give a nontrival answer for the odd W states of the HFBI, where this exact degeneracy is seen throughout

the spectrum.

The MPS analysis of inversion symmetry proceeds similarly. We will consider in general any symmetry h of the wavefunction that squares to the identity and that can be written in the MPS as the product of an on-site symmetry action U_h and a transpose of the site tensor. This will include an inversion of the honeycomb lattice - equivalent to a 180 degree rotation about the center of any plaquette, which we label $\mathcal{I} = \mathcal{I}_y\mathcal{I}_x$, and the combination of inversion with on-site symmetries. In addition, by blocking two site-tensors together, we can write the reflection symmetry $\mathcal{I}_y$ in this form as well. In this scenario, the edge symmetry action satisfies

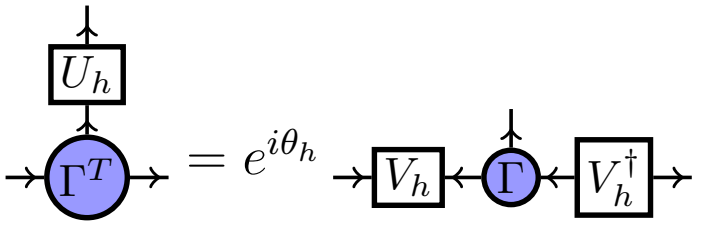

(1.21)

The map V_h is also computed from an eigenvector problem.

1.4.3 Results of symmetry calculation

The on-site symmetries of the featureless boson insulator considered here are the $U(1)$ charge symmetry and the anti-unitary time-reversal symmetry τ, which acts by complex conjugation in the boson number basis. Despite being at half-filling, the hard-core boson variant of the state does not have a particle-hole symmetry. Exploring the edge action of these symmetries numerically, we find that they are all represented linearly and thus do not protect the degeneracy of the entanglement spectrum on cylinders of

odd circumference. In order to protect the degeneracy, we must therefore include lattice symmetries.

By choosing a cylinder geometry, we explicitly break some of the lattice rotational and reflection symmetries. The remaining symmetries are generated by translations T_x parallel and T_y perpendicular to the cylinder axis as well as reflections $\mathcal{I}_x$ about a line parallel and $\mathcal{I}_y$ about a line perpendicular to the cylinder axis. We also consider lattice inversion $\mathcal{I} = \mathcal{I}_x\mathcal{I}_y$, equivalent to a π rotation of the spatial plane about the center of a hexagonal plaquette. These symmetries are illustrated in Fig. 1.12. We find that a number of symmetry-protected topological invariants that are defined through these symmetries take non-trivial values in the HFBI, thus protecting the doubly degenerate entanglement spectrum on odd circumference cylinders. The complete list of non-trivial invariants is summarized in Table 1.1.

The crucial ingredient underlying these SPT invariants is a spatial symmetry h that swaps the two sides of the entanglement cut. By a general symmetry analysis of Eq. (1.15), V_h must act as a particle-hole symmetry on the edge, since the Schmidt pairing S (Eq. (1.14)) pairs states with opposite quantum numbers. In this case, the symmetry action $V_{\mathcal{I}_y}$ is precisely that of a particle-hole transformation in the local PEPS basis. Defining $|\vec{\sigma}) = |\sigma_1, \ldots, \sigma_W)$ and $|1-\vec{\sigma}) = |1-\sigma_1, \ldots, 1-\sigma_W)$, we find that

$$V_{\mathcal{I}_y} |\vec{\sigma}) = |1-\vec{\sigma}) \,, \tag{1.22}$$

since a state where the i^{th} hexagon contributes σ_i bosons on the right is paired with a state where the i^{th} hexagon contributes $1-\sigma_i$ on the left. We can thus read off that $V_{\mathcal{I}_y}$

Group	Generators	Invariant	i
$\mathbb{Z}_2^P$	$\{\Pi\mathcal{I}\}$	$V_{\Pi\mathcal{I}}V_{\Pi\mathcal{I}}^* = -I$	$-$
$\mathbb{Z}_2^P$	$\{\Pi\mathcal{I}_y\}$	$V_{\Pi\mathcal{I}_y}V_{\Pi\mathcal{I}_y}^* = -I$	$-$
$\mathbb{Z}_2 \times \mathbb{Z}_2^{PT}$	$\{\Pi, \tau\mathcal{I}\}$	$V_\Pi V_{\tau\mathcal{I}} V_\Pi^{-1} V_{\tau\mathcal{I}}^{-1} = -I$	$+$
$\mathbb{Z}_2 \times \mathbb{Z}_2^{PT}$	$\{\Pi, \tau\mathcal{I}_y\}$	$V_\Pi V_{\tau\mathcal{I}_y} V_\Pi^{-1} V_{\tau\mathcal{I}_y}^{-1} = -I$	$+$
$\mathbb{Z}_2 \times \mathbb{Z}_2^{PT}$	$\{\Pi\mathcal{I}_x, \tau\mathcal{I}\}$	$V_{\Pi\mathcal{I}_x} V_{\tau\mathcal{I}} V_{\Pi\mathcal{I}_x}^{-1} V_{\tau\mathcal{I}}^{-1} = -I$	$+$
$\mathbb{Z}_2 \times \mathbb{Z}_2^{PT}$	$\{\Pi\mathcal{I}_x, \tau\mathcal{I}_y\}$	$V_{\Pi\mathcal{I}_x} V_{\tau\mathcal{I}_y} V_{\Pi\mathcal{I}_x}^{-1} V_{\tau\mathcal{I}_y}^{-1} = -I$	$+$

Table 1.1: Summary of symmetry protecting invariants found for the HFBI state. The last column indicates whether the symmetry acts unitarily ($i = +$) or antiunitarily ($i = -1$) on the edge. The degenerate entanglement spectrum cannot be split unless all 6 of the minimal protecting symmetry groups are broken.

acts like σ_x in the space spanned by the states $\{|\vec{\sigma}), |1-\vec{\sigma})\}$.

When W is odd, these states have opposite charge parity. Specifically, if $\Pi = e^{i\pi\mathcal{Q}} \in U(1)$ is the charge parity symmetry, we have

$$\begin{aligned} V_\Pi |\vec{\sigma}) &= (-1)^{\sum \sigma_i} |\vec{\sigma}) \\ V_\Pi |1-\vec{\sigma}) &= (-1)^{\sum (1-\sigma_i)} |1-\vec{\sigma}) \\ &= (-1)^W (-1)^{\sum \sigma_i} |1-\vec{\sigma}) \end{aligned} \tag{1.23}$$

Therefore, for W odd, V_Π acts like σ_z in the space $\{|\vec{\sigma}), |1-\vec{\sigma})\}$. It is thus reasonable to expect that the combination of these two symmetries acts as $V_{\Pi\mathcal{I}} = \sigma_x\sigma_z$, which would obey the property that $V_{\Pi\mathcal{I}}V_{\Pi\mathcal{I}}^* = -I$ and thus form a topological invariant.

The local PEPS basis is not unitarily equivalent to the canonical form basis, so we must check this numerically by performing an explicit calculation in the canonical form of an MPS representation of the state, as outlined in Section 1.4.2.

We thus confirm SPT invariants for symmetries that involve such a spatial symmetry h

and an on-site symmetry. There are several appropriate invariants, as listed in Table 1.1; the simplest is

$$V_{\Pi\mathcal{I}} V^*_{\Pi\mathcal{I}} = -I. \tag{1.24}$$

From this we see that the charge, translation, and inversion symmetry can all be broken without splitting the entanglement degeneracy, as long as the single combined symmetry $\Pi\mathcal{I}$ is preserved. In Section 1.5, we will discuss perturbations that preserve this symmetry.

We note that there are also symmetries that act unitarily on the edge and yield SPT invariants; however, these must form the group $\mathbb{Z}_2 \times \mathbb{Z}_2$ as $\mathbb{Z}_2$ does not have unitary projective representations. Examples for this are formed by involving time-reversal symmetry; since V_τ and $V_\mathcal{I}$ both act antiunitarily, $V_{\tau\mathcal{I}}$ acts unitarily on the edge. The $\mathbb{Z}_2 \times \mathbb{Z}_2$ group generated by $\tau\mathcal{I}$ and Π has a projective representation characterized by the topological invariant

$$V_\Pi V_{\tau\mathcal{I}} V_\Pi^{-1} V_{\tau\mathcal{I}}^{-1} = -I. \tag{1.25}$$

This symmetry protection gives a distinct class of perturbations that cannot split the entanglement degeneracy. The complete set of symmetry groups we find is summarized in Table 1.1.

We can form variants of the HFBI state, which are unitarily related to the original state by an on-site unitary and thus share the same entanglement spectrum, where the entanglement degeneracy can be protected by a lattice symmetry alone without involving the on-site Π symmetry. Essentially, the protecting symmetries of the variant generated

by a unitary U is obtained by conjugating the generators of the protecting symmetries of the HFBI by U. These will be discused further in Appendix 1.9.

We also mention that the symmetry protected invariants produced above imply the existance of non-local correlations in the form of 'membrane' order parameters that naturally generalize the string order parameters from one-dimensional SPT phases [121]. For example, the sign of $V_{\Pi\mathcal{I}}V^*_{\Pi\mathcal{I}}$ can be detected by measuring the overlap of the state $|\psi\rangle$ and the same state with a partial application of the protecting symmetry, i.e.

$$\lim_{n\to\infty} \langle\psi|(\Pi\mathcal{I})_{1,2n}|\psi\rangle \propto (-1)^W, \tag{1.26}$$

where $(\Pi\mathcal{I})_{1,2n}$ is the restriction of $\Pi\mathcal{I}$ to $2n$ cylinder slices. We leave open the question of whether this 'membrane' order parameter generalizes in any way to regions that do not wrap the cylinder.

For the HFBI, the symmetry group respected by the cylinder geometry is $U(1)\times(\mathbb{Z}_W \rtimes \mathbb{Z}_2)\times\mathbb{Z}_2^P\times\mathbb{Z}_2^T$, where the factors refer to charge symmetry, translation around the cylinder, $\mathcal{I}_x$, $\mathcal{I}_y$, and τ respectively. The P and T denote space-reversing and time-reversing symmetries, and signify the antiunitary action on the Schmidt states. Many of the non-trivial projective representations of such a complicated group will remain projective when the symmetry is restricted to a subgroup - in this case, the full symmetry is not needed to protect the entanglement degeneracy. As shown in Table 1.1, the projective representation corresponding to the HFBI state can indeed be protected by any one of a number of subgroups of the full symmetry group, all involving inversions and charge parity.

The symmetry actions – both on-site and inversion symmetries – are computed in the Schmidt basis, but can be transformed into the basis $|\{\sigma_i\})$ determined by the virtual legs of the PEPS in Figure 1.3(e). In this case, the symmetry action $V_{\mathcal{I}_y}$ is precisely a particle-hole symmetry in the local PEPS basis, with coefficients

$$V_{\mathcal{I}_y} |\sigma_1, \ldots, \sigma_W) = |1 - \sigma_1, \ldots, 1 - \sigma_W) ,$$

since a state where the i^{th} hexagon contributes σ_i bosons on the right is paired with a state where the i^{th} hexagon contributes $1 - \sigma_i$ on the left. Thus

$$V_{\mathcal{I}_y} = \prod_i \sigma_i^x K,$$

where K is complex conjugation in the local PEPS basis, and σ_i^x is the Pauli operator acting on the i^{th} site of the local PEPS basis.

Charge symmetry acts locally as well:

$$e^{i\theta\mathcal{Q}} |\sigma_1, \ldots, \sigma_W) = e^{i\theta \sum(\sigma_i - 1/2)} |\sigma_1, \ldots, \sigma_W) .$$

In particular, charge parity $V_{\Pi} = e^{i\theta\mathcal{Q}}$ can be written as

$$V_{\Pi} = e^{i\pi \sum(\sigma_i - 1/2)} = \prod_i \sigma_i^z.$$

The combined action of charge parity and reflection across the cut takes the form

$$V_{\Pi\mathcal{I}_y} = \prod_i (i\sigma_i^y)\, K,$$

which is precisely the form that time-reversal acting on an ordinary spin-$\frac{1}{2}$ chain takes. When the circumference of the cylinder W is odd, we see that

$$V_{\Pi\mathcal{I}_y} V^*_{\Pi\mathcal{I}_y} = -I.$$

The degeneracy of the entanglement spectrum can be seen as an application of Kramer's theorem. Formally, this property is said to characterize the nontrivial projective representation

$$H^2(\mathbb{Z}_2^P; U(1)) = \mathbb{Z}_2,$$

and remains true while $\Pi\mathcal{I}_y$ is a symmetry and no phase transitions have occurred.

Time reversal symmetry acts as complex conjugation in the local PEPS basis $V_\tau = K$. Translation and $\mathcal{I}_x$ act as permutations of the local PEPS basis:

$$\begin{aligned} V_T \left|\sigma_1, \ldots, \sigma_W\right) &= \left|\sigma_2, \ldots, \sigma_W, \sigma_1\right) \\ V_{\mathcal{I}_x} \left|\sigma_1, \ldots, \sigma_W\right) &= \left|\sigma_W, \ldots, \sigma_1\right). \end{aligned}$$

These symmetries can be combined with $V_{\Pi\mathcal{I}_y}$ to create the additional topological invariants shown in Table 1.1. A non-trivial projective representation in

$$H^2(\mathbb{Z}_2 \times \mathbb{Z}_2; U(1)) = \mathbb{Z}_2$$

is created whenever two unitary symmetries that commute in the bulk satisfy

$$V_{g_1} V_{g_2} V_{g_1}^{-1} V_{g_2}^{-1} = -I.$$

Each new invariant is related to a new set of pertubations that can't break the entanglement degeneracy.

1.4.4 Tight-Binding Restriction

Before concluding this section, we comment briefly on the role played by the restriction to a particular tight-binding model. Restricting to a particular tight-binding model is a stronger condition than merely specifying a space group symmetry. For instance, the triangular, honeycomb, and kagome lattices all share the same space group, but encode it using one, two and three orbitals per unit cell, respectively. An example is graphene: the electronic Dirac cones in graphene are protected (for vanishingly small spin-orbit coupling) not solely by its space group symmetries, but rather by the tight-binding representation of those symmetries [26] [2]. A restriction to a tight-binding representation is often well motivated by experiments. Choosing a tight-binding model amounts to restricting to the class of models that can be represented using precisely the orbitals we began with; if we are given the freedom to *add* sites, it may be possible to exit a topological phase and enter a trivial one without closing the gap, while still preserving lattice symmetry. For the HFBI, this would be accomplished by adding sites at hexagon

[2] For additional discussion of this point, see [117]

centers, and adiabatically deforming the relative weights afforded to bosons placed at the new sites and the original honeycomb lattice positions. The symmetry protection of the entanglement structure is thus fairly subtle.

This subtlety is better understood for the simpler case of non-interacting fermions. The classification of free-fermion topological phases is known to be richer if one removes the freedom to add trivial bands [86]. The continuity between two phases which arises upon the addition of such trivial bands is known as "stable equivalence" in accord with a basic notion in K-theory [86]. We note that this tight-binding restriction also distinguishes the HFBI and related symmetry-protected short-range entangled states from the ground states of "filling-enforced" topological band insulators introduced very recently [119].

1.5 Quasi-local parent Hamiltonian and perturbations

We now re-examine the question of whether the HFBI state is representative of a robust phase of matter that is separated from conventional phases by phase transitions. One way to demonstrate this – beyond the topological invariants discussed above – is to find a local Hamiltonian with a unique ground state that is the HFBI wavefunction and study the ground state properties under perturbations to this Hamiltonian. For many tensor network states – those that satisfy an injectivity condition [118] — a frustration-free, local

parent Hamiltonian with a unique ground state can be explicitly constructed. In our case, this injectivity condition can be shown to not hold on any simply connected cluster of sites that we can numerically access, and this specific construction of a parent Hamiltonian is thus not possible. Given the challenges of numerical simulations of two-dimensional systems, an exhaustive numerical search for such a Hamiltonian seems unfeasible.

To avoid these problems, we will focus on a quasi-1D approach in this section. This is based on the observation that while the PEPS is not injective on simply connected clusters, it does turn out to be injective on slices of an infinite cylinder. This gives rise to a gapped Hamiltonian whose unique ground state is the HFBI. This 'parent Hamiltonian' is local in the non-compact direction of the cylinder, but non-local around the cylinder and dependent on the circumference W. We believe that nevertheless, the insights gained from these (partially non-local) Hamiltonians can serve as a starting point for identifying the phase in more sophisticated numerical studies of fully two-dimensional boson systems.

Given the unperturbed Hamiltonian, we study the robustness of the entanglement spectrum to perturbations. This depends on the class of perturbations allowed – SPT phases are only distinct if perturbations that break the symmetry are forbidden, which is reflected in the fact that the topological invariants that distinguish the phases are ill-defined in the absence of the symmetry. According to the results discussed in Section 1.4, it is not necessary for the perturbations to preserve the entire symmetry group of the HFBI wavefunction to preserve the entanglement in the state. Instead, the entanglement is robust to any perturbation that does not break *all* of the six protecting groups discussed

in Table 1.1. This set of perturbations is much bigger than the set of perturbations that preserve the entire symmetry group of the HFBI wavefunction. We will confirm that the double degeneracy throughout the entire entanglement spectrum survives these perturbations for odd-W cylinders, while it splits for other perturbations that break all of the protecting symmetries.

1.5.1 Parent Hamiltonians for the $W = 1$ cylinder and equivalence to the Haldane insulator

The $W = 1$ cylinder with hard-core bosons has a Hilbert space equivalent to a two-leg spin-$\frac{1}{2}$ ladder. The HFBI state in this case has a natural MPS representation of bond dimension $d = 2$, constructed by contracting the tensors around each cylinder slice. A well-known property of MPS is the existence of a parent Hamiltonian – a frustration-free Hamiltonian with its unique ground state given by the MPS, first introduced by Ref. [43]. The parent Hamiltonian is constructed in this case as a translationally invariant sum of projectors, where each term projects the Hilbert space of two consecutive rungs of the ladder to the $d^2 = 4$ dimensional subspace of states form spanned by the nonzero eigenvectors of the reduced density matrix of those two rungs. The result H_0 of this construction involves all possible terms that act on two rungs of the ladder and preserve charge and reflection symmetry.

Using a local unitary transformation discussed in detail in Appendix 1.8, we can transform the wavefunction of the HFBI on the $W = 1$ cylinder to that of the 'Haldane

insulator' [17, 122], which is known to be the ground state of an extended Bose-Hubbard model on the two-leg ladder in an appropriate parameter regime, and has also been shown to be a 1D SPT with a doubly degenerate entanglement spectrum and a non-local string order parameter protected by charge parity times inversion $\Pi\mathcal{I}$.

This extended Bose-Hubbard Hamiltonian that gives rise to the Haldane insulator includes only hopping and density-density interactions; additionally, the range of these interactions extends only to neighboring rungs of the ladder. It is thus clear that the additional interactions present in the parent Hamiltonian for the HFBI can be tuned away without undergoing a phase transition. The hard-core bosons should additionally be considered to have infinite on-site density interactions, which can be tuned away from infinity to make a state with soft-core bosons.

1.5.2 Perturbing the state on the $W = 3$ cylinder

Similar to the $W = 1$ cylinder, we can obtain a parent Hamiltonian for the $W = 3$ cylinder as a sum of local projectors acting on adjacent slices of the cylinder. We then consider two different perturbations to these quasi-local parent Hamiltonians. For each perturbation, we use infinite time-evolving block decimation (iTEBD) [145, 146, 147, 113] to evolve an initial wavefunction in imaginary time until it converges to the ground state of the perturbed Hamiltonian. The two perturbations considered are the superfluid pairing

$$H' = \Delta \sum_{\langle ij \rangle} b_i b_j + h.c., \tag{1.27}$$

which breaks the $U(1)$ charge symmetry down to the $\mathbb{Z}_2$ charge parity subgroup and the uniform field

$$H' = h \sum_i \left(b_i + b_i^\dagger \right), \tag{1.28}$$

which fully breaks $U(1)$ charge symmetry but preserves lattice symmetry. The perturbation in (1.27) does not break the protecting symmetry $\mathit{\Pi}\mathcal{I}$, while the perturbation in (1.28) breaks all of the protecting symmetries.

Figure 1.13 show the resulting entanglement spectra from the ground states obtained with iTEBD. Indeed, the perturbation in (1.28) splits the degenerate entanglement spectrum, whereas the double-degeneracy of the entire spectrum is preserved for those perturbations that do not break all of the protecting symmetries. In the case of a symmetry-breaking perturbation, the splitting is most easily observed for the higher levels, but – as shown in the inset – also the lowest values of the entanglement spectrum are weakly split by an amount that scales roughly linearly in the strength of the perturbation.

Unfortunately it is beyond the scope of this work to determine which perturbations leave the CFT structure of the entanglement spectra intact. To assess this would require a Hamiltonian that is local in two dimensions (rather than the Hamiltonians used here which are only local in the non-compact direction of the cylinder). Furthermore, it would require being able to perform accurate simulations for large cylinders, which is prohibitive with the techniques used here.

1.6 Boson-Vortex Duality

An alternative approach for examining the phase structure of two dimensional bosonic systems is to use the boson-vortex duality, which rewrites the theory in terms of the superfluid vortex degrees of freedom defined on the dual lattice. In this picture, the site filling of bosons on the original lattice is mapped to an effective magnetic flux through dual lattice plaquettes that modifies the vortex hopping via the usual Aharonov-Bohm phases [36, 45]. In the dual description the superfluid and Mott insulating phases of the bosons are respectively mapped into the gapped and condensed phases of the vortices. It is instructive to see how this approach fares on the honeycomb lattice at half-site-filling. The vortices move on the dual triangular lattice, and the original site filling of $1/2$ corresponds to a π-flux for vortices for every triangular lattice plaquette. Each unit cell on the triangular lattice contains a pair of triangles and hence 2π flux; as a consequence, the vortices transform normally (rather than projectively) under lattice symmetries. Naively, the π-flux has the effect of inverting the vortex band structure so that the vortex minima are shifted to the Brillouin zone corners K, K' rather than the zone center Γ. Condensing vortices at the zone corners would break lattice symmetries [158]. However, the fact that the vortices transform regularly under lattice symmetries — in other words, that the flux pattern does not lead to an enlarged magnetic unit cell — allows us to add additional hopping while preserving symmetries to returns the vortex minimum to Γ. Condensing vortices at Γ then restores the $U(1)$ symmetry while preserving all lattice symmetries; the resulting phase is an insulating phase of bosons at half-filling on the honeycomb

lattice with no broken symmetries. This argument underscores the fact that such a phase is fundamentally possible. It is not fully clear whether the result of this vortex condensation picture is indeed the HFBI phase, as the argument does not shed light on the entanglement structure of the insulating phase. As there are no known symmetry-preserving insulating phases of bosons on the honeycomb lattice at this filling other than the HFBI and its variants, we conjecture that this phase is adiabatically connected to the HFBI. If instead it is a distinct phase, then it is separated by a phase transition from the HFBI, as long as the symmetries and tight-binding structure of the honeycomb lattice are preserved.

It is perhaps worth noting that the vortex-condensation picture also illustrates a fundamental distinction between half-filling on Bravais and symmorphic non-Bravais lattices. As an example, consider half-filling on the square lattice [8]; performing the duality transformation, we arrive at a theory of vortices moving on the dual square lattice with π flux through each plaquette. Crucially, this flux assignment on the square lattice doubles the unit cell, and so vortices form a projective representation of the space group (related to the magnetic translations familiar from studying particles in a magnetic field). This projective structure cannot be removed and so *guarantees* that a single non-degenerate minimum cannot be restored for any choice of vortex hopping parameters. Put differently, the vortices are (unlike in the honeycomb case) forced to carry non-trivial space group quantum numbers, and the condensation of single vortices necessarily breaks the symmetry [8]. Other approaches lead to more exotic alternatives, e.g. condensing vor-

tices in pairs triggers fractionalization. This in accord with the expectation that a gapped featureless insulator is absent on the half-filled square lattice [115, 114, 70, 71].

1.7 Concluding Remarks and Discussion

We have applied recently developed tensor network methods to study the edge properties of a bosonic insulator that is featureless in the bulk. Our simulations are performed for an infinitely long cylinder of finite circumference W. This allows us to numerically extract the exact entanglement spectrum for up to $W = 10$. We find that the entanglement gap closes as $1/W$, and that furthermore the low-lying spectrum coincides to high accuracy with the spectrum of a free boson conformal field theory. This is further corroborated by observing a central charge of $c = 1$ in the entropy of the lowest Schmidt state.

While these observations are consistent with and strongly suggestive of a symmetry-protected topological phase, where such a gapless spectrum would naturally emerge at the edge, these calculations do not establish a rigorous connection between the edge spectrum and symmetry-protection, i.e. they leave open the possibility that the gapless entanglement spectrum is accidental. To make progress on this question, we analyze in some detail the exact degeneracies in the entanglement spectrum for cylinders of odd circumference W. Using recently developed tools based on matrix-product states, we are able to establish a strong connection to the symmetries of the state by computing topological invariants that detect the non-trivial action of certain symmetry operations. These symmetry operations, whose action is non-trivial, consist of particular combina-

tions of lattice and spin symmetries on the edge. This establishes in the affirmative that the quasi-one-dimensional systems obtained for odd cylinder widths W represent one-dimensional symmetry-protected topological phases.

We cannot establish with the same rigor that the symmetries that protect these one-dimensional topological invariants also protect the gapless edge spectrum on the edge of the two-dimensional system. However, several considerations are in favor of this. Firstly, we observe that the symmetries that are shown to be relevant to the case of odd W are not inherently one-dimensional and could apply equally well to the full, two-dimensional system. The partial application of symmetry in the non-local order parameter in Eq. (1.26) could be applied to arbitrary inversion-symmetric regions in the plane, and not only to cylinder slices. Additionally, we can construct an argument based on the picture of the edge physics provided by the tensor network representation. As outlined in Section 1.3, the edge of the tensor network representation with the cut chosen here can be represented using the Hilbert space of a model of hard-core bosons hopping on a one-dimensional chain with one site per plaquette, where the occupation of a site corresponds to whether the boson of that plaquette is found on the left or right side of the cut. In this representation, the reflection symmetry about the cut takes the special role of guaranteeing equal probability for the boson to be on the left or right of the cut, and thus fixing the model for the edge to half-filling. Thus, if the edge remains translationally symmetric, our model for the edge has fractional charge per unit cell. If the entanglement Hamiltonian can be thought of as local, the Lieb-Schultz-

Matthis theorem applies and guarantees that the entanglement edge is either gapless or spontaneously breaks a symmetry. This suggests that the phase is a two-dimensional symmetry-protected topological phase with a protecting group that includes translation and $\Pi\mathcal{I}$.

The calculations presented here provide a case study where tensor network representations lead to novel insights into strongly correlated physics beyond what is accessible to more traditional methods, such as the quantum-to-classical mappings pursued in Ref. [83] and reviewed in Section 1.1. The tensor-network techniques used in the present approach allow us to strengthen the conclusions of Ref. [83], in particular on the absence of topological order, and reveal entanglement properties that are entirely out of reach of quantum-to-classical mappings. It is amusing to note that this development in theoretical methodology closely parallels the history of the prototypical SPT phase, the AKLT phase of the spin-1 chain, where the existence of a quantum-to-classical mapping was known well before the nontrivial entanglement structure was understood. As in that example, we expect that here as well, the quantum-to-classical mappings are restricted to rather special points within a broader SPT phase, whereas the tensor-network description and its corresponding entanglement structure are expected to be valid more generally throughout the phase.

The question of a parent Hamiltonian, i.e. whether the HFBI can be established as the unique ground state of a gapped local Hamiltonian, remains open. As reviewed briefly in Sec. 1.5, the structure of the PEPS does not allow us to straightforwardly extract a local

parent Hamiltonian in two dimensions. However, this by no means implies that such a parent Hamiltonian does not exist, and future work will explore different numerical approaches to find such a Hamiltonian.

Note: While completing this work, we became aware of related PEPS constructions of featureless paramagnetic wavefunctions on the square lattice with spin 1 per site, and on the honeycomb lattice with spin 1 or $\frac{1}{2}$ per site [79]. The spin-$\frac{1}{2}$ honeycomb lattice example corresponds to the same filling as the featureless insulating phase considered here, but has higher symmetry ($SO(3)$) compared to the $U(1)$ symmetry in the present chapter. We note that even in the case where we consider spinful fermions (see Appendix 1.9.2) bound into Cooper pairs, the wavefunction we construct here is *not* a valid wavefunction for a spin-only model: projecting it to the case of single-fermion occupancy per site (as appropriate to a spin model) annihilates the wavefunction. It will be interesting to study if the spin-only wavefunctions constructed in Ref. [79] possess similarly rich entanglement structure as the HFBI.

1.8 From the AKLT to the $W = 1$ HFBI

The AKLT state $|\psi_{\text{AKLT}}\rangle$ is a state of a spin-1 chain that has an exact representation as an MPS of bond dimension 2 using site tensors A^p_{ij} related to the Pauli matrices [136]. It is the exact ground state of the AKLT Hamiltonian

$$H_{\text{AKLT}} = \sum_j \vec{S}_j \cdot \vec{S}_{j+1} + \frac{1}{3}(\vec{S}_j \cdot \vec{S}_{j+1})^2, \tag{1.29}$$

but it is known that the simpler Hamiltonian

$$H_{\mathrm{AF}} = \sum_j \vec{S}_j \cdot \vec{S}_{j+1} \tag{1.30}$$

is in the same phase, i.e. the AKLT state lies in the Haldane phase of the spin-1 Heisenberg chain. By a series of transformations, we can find a representative MPS wavefunction $|\psi_{\mathrm{HI}}\rangle$ and a simple representative Hamiltonian that can be adiabatically connected to the $W = 1$ HFBI and its corresponding parent Hamiltonian.

By using the unitary operator

$$U(\pi) = \prod_{j \text{ even}} e^{i\pi S_j^z} \tag{1.31}$$

which flips the x, y components of the spins on every other site, we create a wavefunction representative of the Haldane insulator (HI) [17] phase, which is protected by $U\mathcal{I}U^\dagger = \mathit{\Pi}\mathcal{I}$ [122]. This phase is obtained as the ground state of the Hamiltonian

$$H' = UH_{AF}U^\dagger \tag{1.32}$$

$$= \sum_j \left(-\frac{1}{2}(S_j^+ S_{j+1}^- + h.c.) + S_j^z S_{j+1}^z \right). \tag{1.33}$$

Each spin-1 degree of freedom can be split into a pair of $S = 1/2$ spins to make a state on a spin-$\frac{1}{2}$ ladder. An appropriate Hamiltonian can be found in terms of the new spin variables $\vec{S}_{j,A/B}$ by adding a term to project out the spin-singlet component of $\vec{S}_{j,A} + \vec{S}_{j,B}$.

The spin-$\frac{1}{2}$'s can then be treated as hard-core bosons. The Hamiltonian becomes

$$H_{\mathrm{HI}} = \sum_j -\frac{t}{2}((b_{jA}^\dagger + b_{jB}^\dagger)(b_{j+1A} + b_{j+1B}) + h.c.) \\ + V(n_{jA} + n_{jB} - 1)(n_{j+1A} + n_{j+1B} - 1) \\ - \frac{J}{2}(b_{jA}^\dagger b_{jB} + h.c.) - J(n_{jA} - \frac{1}{2})(n_{jB} - \frac{1}{2}), \quad (1.34)$$

where $t = 1$, $V = 1$, and $J \to \infty$. The J term projects the spin-singlet out of each rung, and in practice only needs to be larger than all other relevant scales to drive the system into the appropriate phase.

We can do the same transformations on the MPS $|\psi_{\mathrm{AKLT}}\rangle$ to obtain a new MPS $|\psi_{\mathrm{HI}}\rangle$ with bond dimension 2 and site tensor $A_{ij}^{\prime p}$ that represents a state in the phase of H_{HI} on the two-leg ladder. The site tensor S_{ij}^p of the $W = 1$ HFBI also has bond dimension 2 and represents a state of hard-core bosons on the two-leg ladder. Numerically, these are

represented by the (unnormalized) site tensors

$$A'^{p} = \begin{cases} \begin{pmatrix} 0 & 0 \\ 2 & 0 \end{pmatrix} & p = (00) \\ \begin{pmatrix} 1 & 0 \\ 0 & 1 \end{pmatrix} & p = (01) \\ \begin{pmatrix} 1 & 0 \\ 0 & 1 \end{pmatrix} & p = (10) \\ \begin{pmatrix} 0 & 2 \\ 0 & 0 \end{pmatrix} & p = (11) \end{cases}$$

and

$$S^p = \begin{cases} \begin{pmatrix} 0 & 0 \\ 1 & 0 \end{pmatrix} & p = (00) \\ \begin{pmatrix} 2 & 0 \\ 0 & 1 \end{pmatrix} & p = (01) \\ \begin{pmatrix} 1 & 0 \\ 0 & 2 \end{pmatrix} & p = (10) \\ \begin{pmatrix} 0 & 5 \\ 0 & 0 \end{pmatrix} & p = (11), \end{cases}$$

where $p = (p_1 p_2)$ represents the occupation numbers of the hard-core bosons on the two sites on each leg of the ladder.

By linearly tuning the site tensors using

$$S^p_{ij}(t) = tA'^p_{ij} + (1-t)S^p_{ij}, \tag{1.35}$$

and checking that the transfer matrix of the resulting state is non-degenerate for all $t \in [0,1]$, we confirmed that the $W = 1$ HFBI can be tuned in the space of bond dimension $d = 2$ MPS to $|\psi_{\mathrm{HI}}\rangle$ without passing through a phase transition, and the representative Hamiltonian in (1.34) describes a state in the same phase.

By calculating the canonical form of the S^p_{ij} site tensor, one can check that the $W = 1$ HFBI wavefunction has particle-hole symmetry, while the $W > 1$ states do not. This particle-hole symmetry C can also be used as a symmetry protection via the $\mathbb{Z}_2 \times \mathbb{Z}_2$

group generated by $\{\Pi, C\}$ or by the time-reversing symmetry $\Pi C\tau$. This fact is well known in the context of the AKLT state, where Π and C are represented in the spin-language as π rotations about the z and x axes, and $\Pi C\tau$ is the time-reversing symmetry iS_yK that flips all components of the spins.

In the context of the argument laid out in the conclusion, it seems that particle-hole symmetry can play the same role as inversion symmetry in ensuring the edge remains at half-filling.

1.9 Variants on the HFBI wavefunction

1.9.1 Tuning soft-core bosons to hard-core

In Equations (1.3) and (1.4), the tensor D can be replaced by a more general form

$$D_{p,i_0i_1i_2} = \begin{cases} d_p & : p = i_0 + i_1 + i_2 \\ 0 & : \text{else} \end{cases} , \tag{1.36}$$

which the coefficients $d_p = 1, 1, \sqrt{2}, \sqrt{6}$ for $p = 0, 1, 2, 3$ in the soft-core state and $d_p = 1, 1, 0, 0$ for $p = 0, 1, 2, 3$ in the hard-core state. We can continously tune the coefficients d_2 and d_3 from the soft-core to the hard-core values. Upon doing so, we find that the transfer matrix spectrum remains gapped, with the correlation length monotonically increasing from the soft-core state to the hard-core state. Furthermore, the low energy parts of the entanglement spectrum do not change significantly through this tuning. Therefore we expect that the hard-core and soft-core phases can be adiabatically connected with a path of local Hamiltonians, and all SPT results that apply to one state

apply to the other. By choosing appropriate values of d_2 and d_3, we can also make a state that is equivalent to replacing the vacuum $|0\rangle$ in Equation (1.1) with a constant background of N bosons on each site, $N \to \infty$, and applying boson annihilation instead of creation operators. We can also make a state of spin-S spins, which is however not SU(2)-invariant, where Equation (1.1) becomes

$$|\psi\rangle = \prod_{\hexagon} \left(\sum_{i \in \hexagon} S_i^+ \right) \prod_i |S_i^z = -S\rangle. \tag{1.37}$$

Here, the hard-core state would most closely correspond to a state of $S = 1/2$ spins, while the soft-core state corresponds to a state of $S = 3/2$ spins. All of these states have the same symmetry protection properties.

1.9.2 Interpretation as a Fermionic Wavefunction

We can also interpret the hard-core variant of the HFBI as a wavefunction for spinful fermions on the honeycomb lattice at half filling. Note that including the spin, 'full filling' of a site corresponds to a pair of fermions on each site, so half filling occurs with exactly one fermion per site, corresponding to two fermions per unit cell. Assuming no spin polarization, there must be an equal number of 'up' and 'down' spins. We can bind pairs of opposite-spin fermions into a Cooper pair, which yields one Cooper pair per unit cell. As a Cooper pair is equivalent to a hard-core boson, we may place the Cooper pairs into the hard-core variant of the HFBI. This is equivalent to the wavefunction

$$|\Psi_e\rangle = \prod_{\hexagon} \left(\sum_{i \in \hexagon} c_{i\uparrow}^\dagger c_{i\downarrow}^\dagger \right) |0\rangle. \tag{1.38}$$

As the Cooper pair is in a spin singlet state, this wavefunction preserves $SU(2)$ spin symmetry, in addition to the lattice and $U(1)$ charge conservation symmetries. It is therefore a symmetry-preserving wavefunction of spinful fermions (i.e., electrons) on the honeycomb lattice at half filling. However, it is *not* a valid wavefunction for a pure $SU(2)$ symmetric spin model, as it has a vanishing projection onto the subspace where each site has exactly unit occupancy. Note that the necessity to have 'preformed pairs' that can then be put into a hard-core boson state vividly illustrates the fundamentally interacting nature of this fermionic state.

1.9.3 Inversion Protected Phase

Additionally, the tensor W in Equation (1.2) can be replaced by the more general form

$$W^{n_1 \ldots n_6} = \begin{cases} p_x : & n_x = 1,\, n_y = 0 \;\forall\; y \neq x \\ 0 : & \text{else} \end{cases}, \tag{1.39}$$

which corresponds to modifying Equation (1.1) to

$$|\psi_\ell\rangle = \prod_{\hexagon} \left(\sum_{i \in \hexagon} p_i b_i^\dagger \right) |0\rangle. \tag{1.40}$$

This does not in general preserve the rotational symmetry of the state, but it does if the coefficients $p_0, \ldots p_5$ are in an angular momentum mode

$$p_x = e^{ix\ell}$$

where $\ell \in \{0, 2\pi/6, \ldots, 5 \cdot 2\pi/6\}$. These 6 discrete solutions can't be continously tuned

Group	Generators	Invariant	i
$\mathbb{Z}_2^P$	$\{\mathcal{I}\}$	$V_{\mathcal{I}}V_{\mathcal{I}}^* = -I$	$-$
$\mathbb{Z}_2^P$	$\{\mathcal{I}_y\}$	$V_{\mathcal{I}_y}V_{\mathcal{I}_y}^* = -I$	$-$
$\mathbb{Z}_2 \times \mathbb{Z}_2^{PT}$	$\{\Pi, \tau\Pi\mathcal{I}\}$	$V_\Pi V_{\tau\Pi\mathcal{I}} V_\Pi^{-1} V_{\tau\Pi\mathcal{I}}^{-1} = -I$	$+$
$\mathbb{Z}_2 \times \mathbb{Z}_2^{PT}$	$\{\Pi, \tau\Pi\mathcal{I}_y\}$	$V_\Pi V_{\tau\Pi\mathcal{I}_y} V_\Pi^{-1} V_{\tau\Pi\mathcal{I}_y}^{-1} = -I$	$+$
$\mathbb{Z}_2 \times \mathbb{Z}_2^{PT}$	$\{\Pi\mathcal{I}_x, \tau\Pi\mathcal{I}\}$	$V_{\Pi\mathcal{I}_x} V_{\tau\Pi\mathcal{I}} V_{\Pi\mathcal{I}_x}^{-1} V_{\tau\Pi\mathcal{I}}^{-1} = -I$	$+$
$\mathbb{Z}_2 \times \mathbb{Z}_2^{PT}$	$\{\Pi\mathcal{I}_x, \tau\Pi\mathcal{I}_y\}$	$V_{\Pi\mathcal{I}_x} V_{\tau\Pi\mathcal{I}_y} V_{\Pi\mathcal{I}_x}^{-1} V_{\tau\Pi\mathcal{I}_y}^{-1} = -I$	$+$

Table 1.2: Summary of symmetry protecting invariants found for the $|\psi_{\ell=\pi}\rangle$ state. The degenerate entanglement spectrum cannot be split unless all 6 of the minimal protecting symmetry groups are broken.

to one another while preserving all the lattice symmetries.

The state $|\psi_{\ell=\pi}\rangle$ can be shown to be related to state $|\psi_{\ell=0}\rangle$ discussed in the main text by a on-site unitary operator $U(\pi)$, where

$$U(\varphi) = \prod_{j \in B} e^{i\varphi \hat{Q}_j}. \tag{1.41}$$

Due to this relation, $|\psi_{\ell=\pi}\rangle$ and $|\psi_{\ell=0}\rangle$ have identical correlation lengths and entanglement spectra. However, the protecting symmetries from Table 1.1 are mapped using conjugation by $U(\pi)$ into a new set of protecting symmetries, shown in Table 1.2. Notably, since

$$U(\pi)\Pi\mathcal{I}U(\pi)^\dagger = \mathcal{I}, \tag{1.42}$$

this state has doubly degenerate entanglement spectra on odd cylinder sizes protected by lattice inversion symmetry alone. Thus while the entanglement degeneracy in the

HFBI state $|\psi_{\ell=0}\rangle$ is not split under a staggered field

$$H' = h^s \sum_i (-1)^i \left(b_i + b_i^\dagger\right)$$
$$\text{with } (-1)^i = \begin{cases} 1 & i \in A \\ -1 & i \in B \end{cases} \tag{1.43}$$

(which fully breaks $U(1)$ charge symmetry and inversion but not the combined symmetry $\Pi\mathcal{I}$), the entanglement degeneracy in the state $|\psi_{\ell=\pi}\rangle$ would be unsplit by a uniform field, which may be physically more interesting.

A similar mapping for 1-D inversion protected states is discussed in Appendix A of Ref. [122]. As discussed in Appendix 1.8, the state $|\psi_{\ell=0}\rangle$ on the $W = 1$ cylinder is adiabatically connected to the 1-D Haldane insulator state [17, 122]. Correspondingly, the state $|\psi_{\ell=\pi}\rangle$ on the $W = 1$ cylinder is adiabatically connected to the 1-D AKLT state.

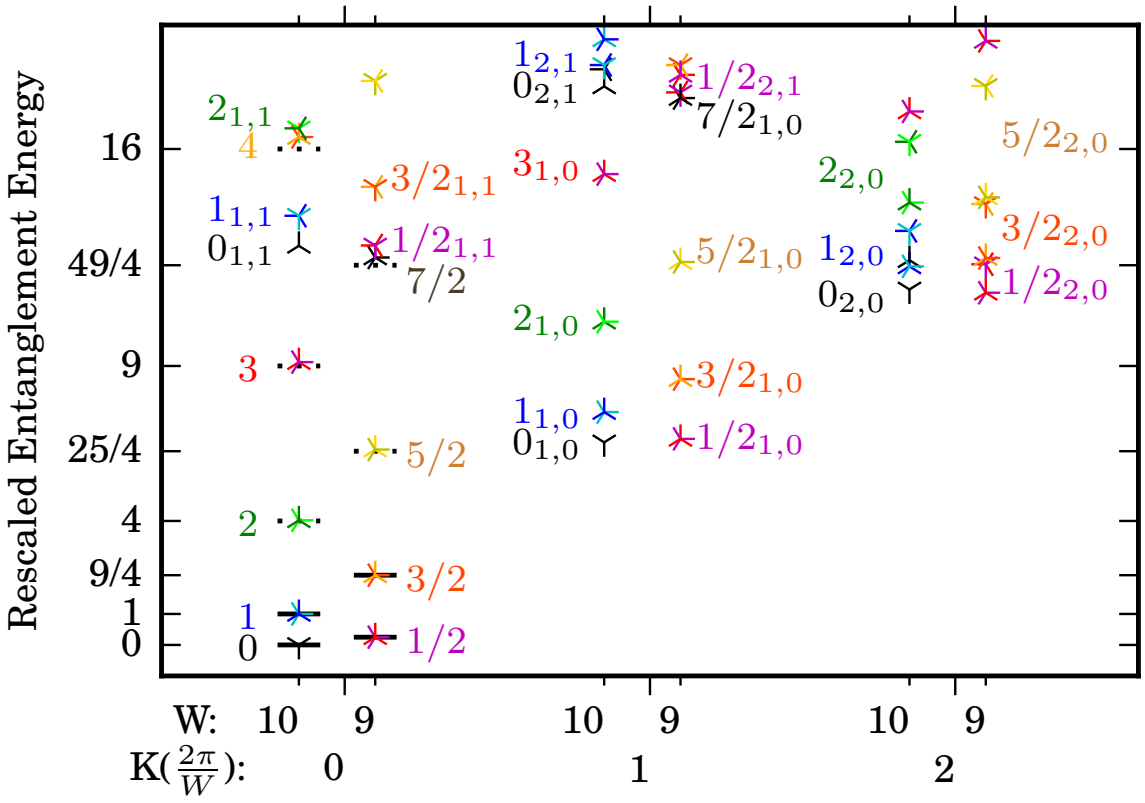

Figure 1.9: The identification of the CFT primaries and level $n, \bar{n}$ descendants in the finite size spectrum of the soft-core boson entanglement Hamiltonian for cylinder circumferences $W = 9$ and 10. The primary states $|e, m, n, \bar{n}\rangle$ with $m = 0, n = 0$, and $\bar{n} = 0$ are labeled in the plot with by their charge e. The lowest such two states for each system size ($e = 0, 1/2, 1, 3/2$) are used to set the zero and scale of the numerical spectrum, while the primaries with charges $2, 5/2, ...4$ appear near the predicted energy e^2. Additionally, descendents of these primaries are labeled in the plot by their charge e and the levels $n, \bar{n}$ shown as subscripts. $m = 0$ for all states appearing in this plot - the $m = \pm 1$ states are shown in Figure 1.10, appearing around momentum π, and the $m = 2$ states are too high in energy to appear here. The best estimate for the Luttinger parameter from this spectrum is $\kappa \approx 1.6$ from the rescaled energy of the $e = 0, m = 0, n = 1, \bar{n} = 0$ state.

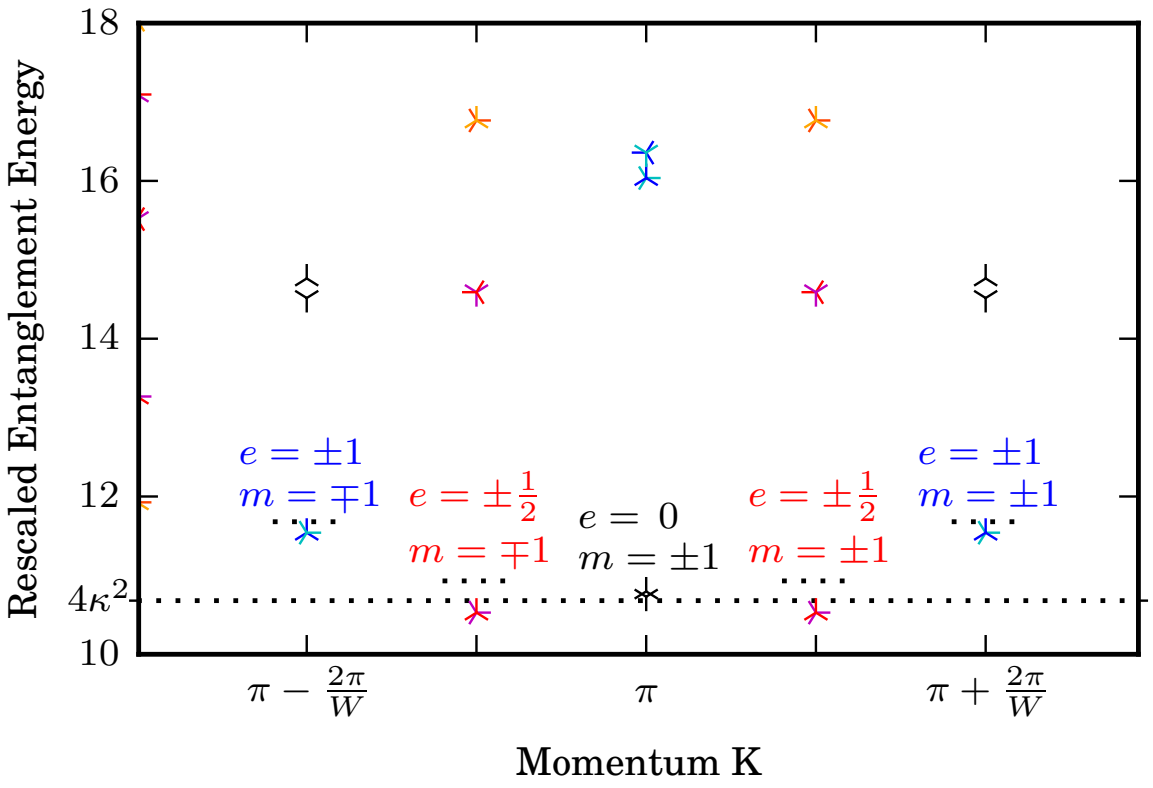

Figure 1.10: The identification of primary states $|e, m = \pm 1\rangle$ and first descendants in the low energy part of the spectrum near momentum π. Unlike the $m = 0$ states shown in Figure 1.9, these primary states have shifted momentum $K = \pi + em(2\pi/W)$ and an extra double degeneracy due to the two values of $m = \pm 1$. Using the estimate $\kappa \approx 1.6$ from Figure 1.9, the predicted value of the entanglement energy for the $|e = 0, m = \pm 1\rangle$ states is $4\kappa^2$, which has been marked in the plot. The agreement is very good.

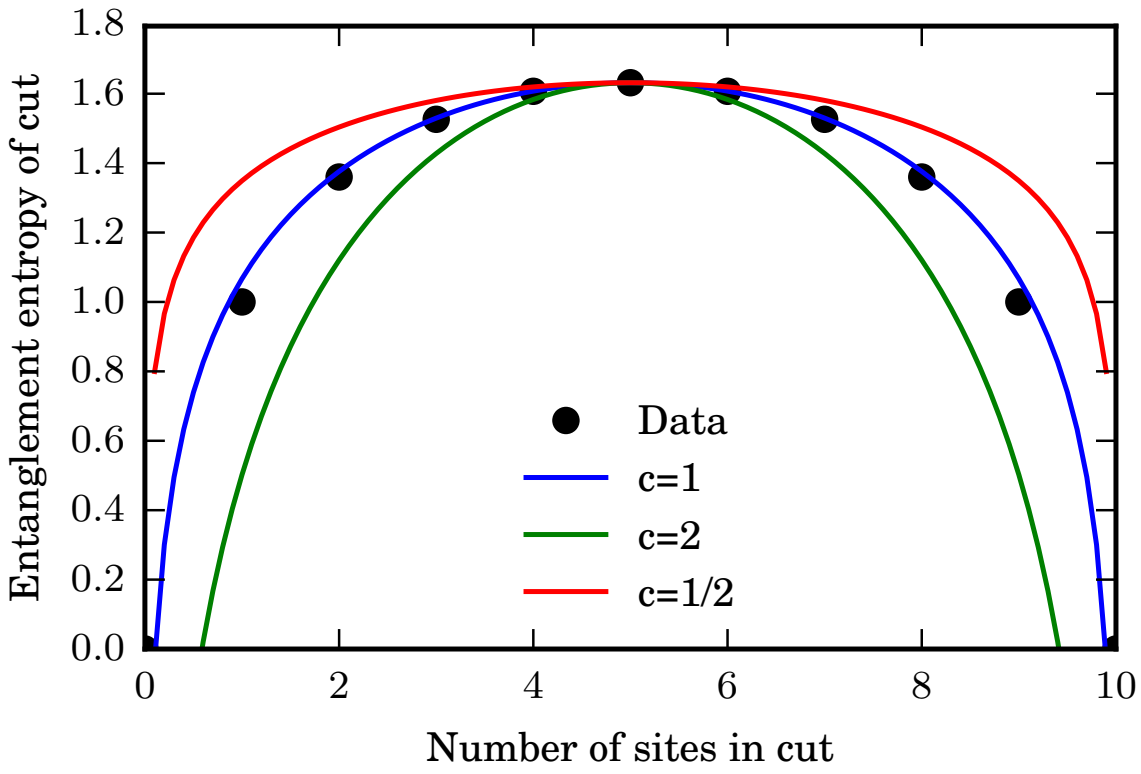

Figure 1.11: Entanglement entropy within the entanglement ground state of the soft-core boson state on 10 sites. For comparison, the Calabrese-Cardy formula [25] $S(x) = c/3 \log \sin(\pi x/L) + const.$ is shown with $c = \frac{1}{2}, 1$, and 2, with the *const.* fixed by matching the maximum of the entanglement entropy data. $c = 1$ is a good fit.

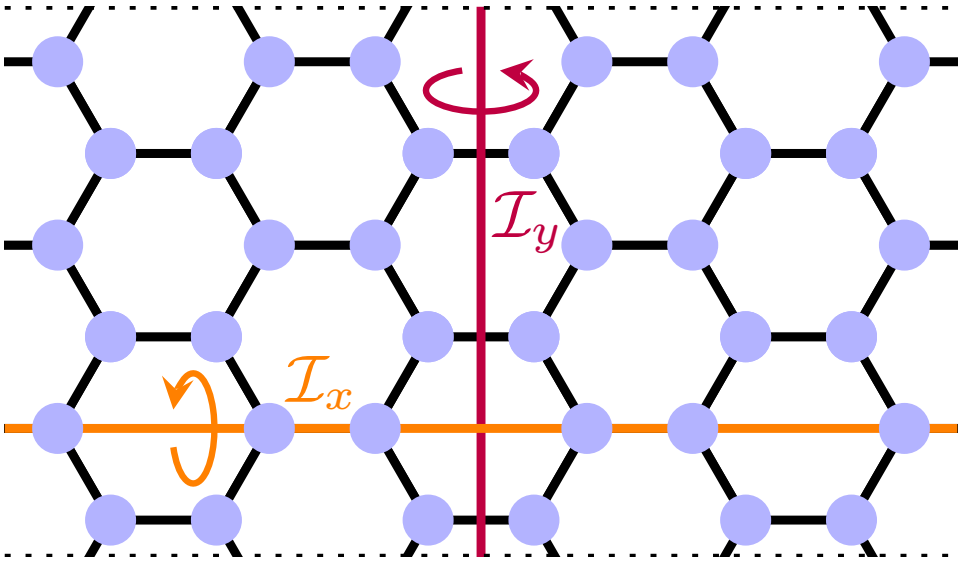

Figure 1.12: Lattice symmetries considered here: (i) $\mathcal{I}_x$ reflection about a line parallel to the long direction of the cylinder, (ii) $\mathcal{I}_y$ reflection about a line perpendicular to the long direction, corresponding to the entanglement cut shown in Fig. 1.3(e). These are both chosen such that the reflection line crosses the hexagon center. Their product, $\mathcal{I} = \mathcal{I}_x\mathcal{I}_y$, thus represents (iii) the inversion about a hexagon center.

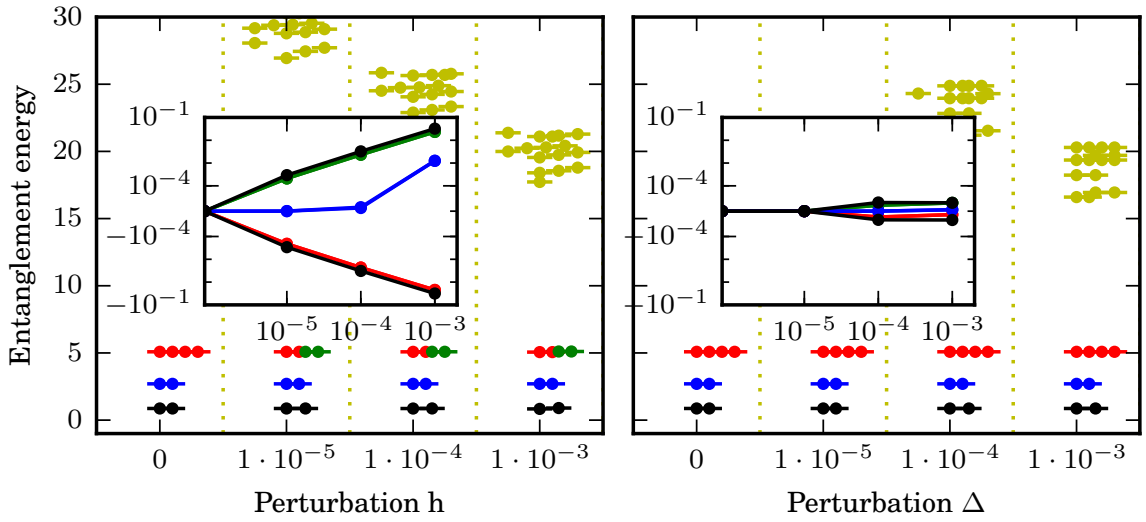

Figure 1.13: Entanglement spectrum for the ground state of the parent Hamiltonian on the $W = 3$ cylinder under a symmetry-breaking perturbation (1.28) (left panel) and a symmetry-preserving perturbation (1.27) (right panel). Insets show the deviations of the lowest eight entanglement energies from their unperturbed values. The initially degenerate entanglement energies are seen to split linearly in the size of the symmetry-breaking perturbation (from the slope of the log-log plot) on the left, while the splittings on the right are zero up to the accuracy of the simulation. Additionally, double degeneracy throughout the entire spectrum remains on the right. These results were obtained using an iTEBD simulation using a bond dimension of $M = 24$.

Chapter 2

Fermionic Topological Phases with Majorana Dimers

2.1 Introduction

Since Anderson's seminal work exploring the relation of high-temperature superconductivity and resonating valence-bond physics [5, 6], dimer models have served as a tool to explore the low-energy behavior of antiferromagnetic spin systems, where fluctuating pairs of spin-singlets are expected to comprise the relevant degrees of freedom [130, 129, 48]. These dimer models describe bosonic degrees of freedom on the links of the lattice with the additional constraint that a fixed number of such dimers emanate from each lattice site. Due to the constrained nature of the Hilbert space, dimer models afford a large degree of analytical control and have been immensely insightful in uncovering the physics of

systems beyond the standard Landau symmetry-breaking paradigm, in particular topological spin liquids [106, 107].

Historically, dimer configurations have often been viewed as proxies for different ways to pair neighboring spins on a lattice into singlets. We go beyond this paradigm by introducing what we term *Majorana-dimer models*: in addition to the dimer degrees of freedom on the links, we introduce Majorana modes [128, 84] on the sites of the lattice. In the low-energy sector of our models, the Majorana modes adjacent to a bond are strongly paired if a dimer is present on this bond. We will see that coupling the fermionic degrees of freedom to dimers in this way generates novel phases of matter that cannot appear in a purely bosonic model. These phases are realized as ground states of frustration-free, and, in one of the settings, indeed exactly solvable Hamiltonians.

In the case of one Majorana mode per site of the lattice, we find realizations of Ising topological order—i.e., an Ising phase—which we substantiate both by observing the pattern of ground-state degeneracy on non-trivial manifolds and by computing modular matrices. Known realizations of the Ising phase, such as Kitaev's honeycomb model [85] or the $\nu = 1$ bosonic Pfaffian fractional quantum Hall state [59, 60], as well as the closely related Moore-Read state for the $\nu = 5/2$ plateau [109], exhibit chiral edge states (in fact required by modularity in bosonic systems [85]). Our models, on the contrary, support fully gapped edges. The resolution crucially relies on the fact that we are considering a *fermionic* system: There is actually a "hidden" $p_x - ip_y$ superconductor, whose chiral Majorana edge states [128] exactly "cancel" those of the Ising phase (see Fig. 2.1); at the

same time, the $p_x - ip_y$ superconductor does not modify the universal bulk properties since it is a short-range entangled state. Therefore, our models generate an intrinsically fermionic topological phase of matter that does not exist in bosonic systems. By placing more than one Majorana mode on each site, we can construct frustration-free parent Hamiltonians for a more general class of models with gapped boundaries. For an odd number of Majorana modes per site, we realize variants of the above Ising $\times$ $(p_x - ip_y)$ phase, while for an even number per site we realize a series of Abelian topological phases with four quasiparticles that are known from Kitaev's 16-fold way [85].

Our construction starts from models of $\mathbb{Z}_2$ topological order, such as the dimer model on the triangular lattice at the Rokhsar-Kivelson point [130] or the toric code on the honeycomb lattice, and then couples their microscopic degrees of freedom to Majorana modes [50, 51]. We first explore the triangular-lattice model [106], where Majorana modes on the lattice sites couple to the dimers in such a way that if a bond is occupied by a dimer, the complex fermion formed by the two adjacent Majoranas is, say, unoccupied. We find that there exists a local Hamiltonian—very much akin to the Rokhsar-Kivelson Hamiltonian for bosonic dimers—whose ground states are equal-weight superpositions of all dimer configurations with the corresponding Majorana configurations formed according to the above rule. The Hamiltonian is found to be frustration-free, i.e., the ground state is a simultaneous eigenstate of all terms of the Hamiltonian. When the dimer model is in the "resonating valence bond" (RVB) phase, deconfined monomer excitations (i.e., sites with no emanating dimers) harbor unpaired Majorana modes, which strongly hints

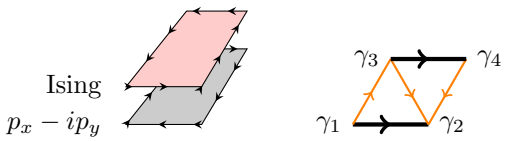

Figure 2.1: Left panel: Bilayer of an Ising phase and a $p_x - ip_y$ topological superconductor with opposite chirality, which together give rise to the topological phase discussed in this chapter. This phase is characterized by three distinct topological sectors, but has a fully gapped edge. Right panel: The Hilbert space of Majorana-dimer models consists of bosonic dimers on the edges of the lattice and Majorana modes on the lattice sites. In the low-energy subspace, the Majoranas are paired according to the placement of the dimers: e.g., the fermion wavefunction corresponding to the dimer configuration shown is the ground state of $H_F = -i\gamma_1\gamma_2 - i\gamma_3\gamma_4$.

at the formation of an Ising-like topological phase.

In a complementary viewpoint, we describe the same phase through a model of fluctuating loops. This perspective follows a recently established paradigm of enhancing loop models by dressing the loops with one-dimensional symmetry-protected topological phases (SPT's). The approach gives a straightforward construction for symmetry-enriched versions of the corresponding loop model [155, 98, 74, 16], since the ends of open strings will carry the same projective representation of the symmetry group as the edge modes of the SPT. The new ingredient here is to consider a one-dimensional fermionic topological phase—the Kitaev chain [84]—that exhibits unpaired Majorana zero modes at the ends. Excitations formed from open strings will thus carry Majorana zero modes. By choosing the Hamiltonian such that the loops fluctuate, these excitations become deconfined and a topologically ordered Ising phase emerges. We construct a commuting-projector Hamiltonian on a Fisher lattice that exactly realizes this scenario.

A similar approach to ours, including the use of Kasteleyn orientations, was used

in Ref. [141] to obtain exactly soluble parent Hamiltonians for all known fermionic symmetry-protected topological phases with an on-site $\mathbb{Z}_2$ symmetry group. The phases described in this chapter can be viewed as gauged versions of the phases described in [141], and on the Fisher lattice a duality transformation—which we discuss in more detail in the Conclusions—can be used to establish a correspondence between the models.

The remainder of this chapter is laid out as follows. Section 2.2 reviews the underlying bosonic quantum dimer models that form the basis for our construction. We then discuss general properties of the Majorana-dimer model constructions in Secs. 2.3.1, 2.3.2, and 2.3.3; the precise form of the dimer dynamics is presented in Secs. 2.3.4 and 2.3.5. Section 2.4 presents ground-state degeneracy and entanglement calculations to determine the precise nature of the topological order in these states. In Sec. 2.5, we discuss the generalizations of our model to systems with more than one Majorana mode per site, drawing on the results established in all the previous sections. Finally, we discuss our results and provide an outlook in Sec. 2.6.

2.2 Review of Bosonic Dimer Models

Before introducing the parent Hamiltonians of the Majorana-dimer construction, we briefly review the Rokhsar-Kivelson [130] Hamiltonian for bosonic dimer models on the triangular lattice [106] and Fisher lattice [46]. In the former case, the Hamiltonian

$$H_{\mathrm{RK}}^{\triangle} = \sum_{p} \left(-tB_p^{\triangle} + VC_p^{\triangle} \right) \tag{2.1}$$

is the sum of dimer flip and potential energy terms, represented by (for one of the plaquette orientations):

$$B_p^{\triangle} = \Big|$$  $$\Big\rangle\Big\langle$$  $$\Big| + \text{h.c.} \tag{2.2}$$

$$C_p^{\triangle} = \Big|$$  $$\Big\rangle\Big\langle$$  $$\Big| + \Big|$$ $$\Big\rangle\Big\langle$$ $$\Big|. \tag{2.3}$$

One can similarly write down these terms for the other two plaquette orientations.

This Hamiltonian is known to form a $\mathbb{Z}_2$ topologically ordered phase for $V_c < V < t$ for some critical $V_c > 0$, and a staggered phase with broken translation symmetry for $V > t$ [107]. At the "RK point" $t = V$, the ground states are exact eigenstates of each individual term of the Hamiltonian, i.e., the Hamiltonian is frustration-free. On a torus, the ground states include equal-weight superpositions of all flippable dimer configurations in each of the four topological sectors of dimers; these ground states extend into the topological phase. Additionally, there are a number of perfectly staggered dimer configurations that remain at zero energy, since they are not connected to other states by the dynamics of the Hamiltonian. These states remain ground states in the staggered phase, but are finite-energy states in the topological phase away from the RK point. The excited states at the RK point are separated from the ground states by a gap of $\Delta \approx 0.2t$.

One can view the dimer model as a spin model, with $S = 1/2$ spins living on the edges of the lattice, and straightforwardly translate the above Hamiltonian into spin terms; in particular, $\sigma_e^z = 1$ indicates the presence of a dimer on edge e while $\sigma_e^z = -1$ corresponds to an empty bond. To enforce the dimer constraint in the language of spins, a vertex

term of the form

$$J\sum_v A_v^{\triangle} = J\sum_v \left(\sum_{e\in v}\sigma_e^z + 4\right)^2 \tag{2.4}$$

must be added, where the sum v runs over the vertices of the lattice. When $J \to \infty$, the dimer constraint is enforced strictly.

We will also use a Rokhsar-Kivelson dimer model on the Fisher lattice [46, 47] obtained by decorating the honeycomb lattice with a triangle on each site (see right panel of Fig. 2.2). The Hamiltonian is given by

$$H_{\mathrm{RK}}^{\hexagon} = -t\sum_p B_p^{\hexagon}, \tag{2.5}$$

$B_p^{\hexagon} =$ 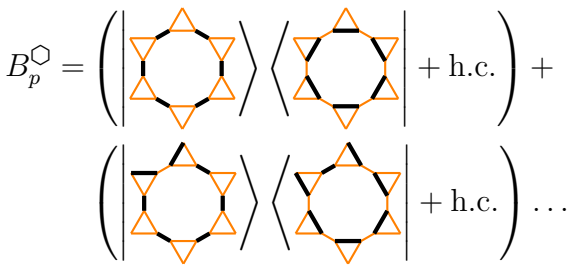 (2.6)

Here the sum runs over all hexagonal plaquettes, and the ... represents all possible (in total 32) local flip moves involving 6 dimers adjacent to a plaquette. This dimer model has the important property that all plaquettes are flippable in every dimer configuration, so that the potential term acts as a constant and can therefore be omitted.

Despite the apparent complexity of the Fisher-lattice dimer Hamiltonian, it admits an exceedingly simple description as a spin model. As with the triangular lattice, the spin model is formed using spin-1/2 degrees of freedom to specify dimer states; however, it

now suffices to place spins only on a subset of edges—the edges between triangles—since the dimer configuration on the remaining edges is completely determined when the dimer constraint is satisfied. We can thus map the model to one of dimer variables on the edges of a honeycomb lattice, which are constrained such that either 1 or 3 dimers emanate from each vertex of the honeycomb lattice. Using the spin-1/2 representation, the spin Hamiltonian in these variables can be written as

$$H_{\mathrm{RK}}^{\hexagon} = -t \sum_{p} B_p^{\hexagon} - J \sum_{v} A_v^{\hexagon}, \tag{2.7}$$

where the individual terms read

$$A_v^{\hexagon} = \prod_{e \in v} \sigma_e^z \qquad\qquad B_p^{\hexagon} = \prod_{e \in p} \sigma_e^x. \tag{2.8}$$

Here the $A_v^{\hexagon}$ term enforces the dimer constraint, and the $B_p^{\hexagon}$ term flips the dimer configuration. We also notice that this Hamiltonian is the same as the toric code on the underlying honeycomb lattice [89]. In fact, if we define an edge of the honeycomb lattice not occupied by a dimer ($\sigma^z = -1$) as being occupied by a string, the dimer constraint can be viewed as the closed-loop constraint for the strings. Thus, as in the toric code, the minimal excitations—violations of a single plaquette term—are dispersionless and carry energy $2t$. On a closed manifold such as a torus, the plaquette terms can only be violated in pairs, so the gap is $4t$.

It is worth mentioning that dimer models have been generalized to describe other

topological phases, such as the double semion phase [52, 96, 127, 77, 23]. The double-semion ground-state wavefunction has a simple representation in the loop basis:

$$|\psi_{\mathrm{DS}}\rangle = \sum_{L} (-1)^{n(L)} |L\rangle. \tag{2.9}$$

Here $n(L)$ is the number of loops while $\{|L\rangle\}$ denotes the set of closed-loop configurations. A similar wavefunction can be written down in the dimer representation, where the amplitude is $(-1)^{n(D)}$ with $n(D)$ being of the number of loops in the transition graph of D. Rokhsar-Kivelson-type models featuring the double-semion ground state were recently found in Ref. [127].

2.3 Majorana-Dimer Models

In this section, we start from the dimer models for $\mathbb{Z}_2$ topological order described in the previous section, and describe how to couple them to fermionic degrees of freedom in a way that yields a new topologically ordered phase. We first review the common ingredients for dressing dimer models with Majorana modes, and then discuss the specifics of two models. We will see that dressing the dimer model on the Fisher lattice yields an exactly solvable model with vanishing correlation length, while starting from the triangular lattice yields a much simpler, but not fully analytically solvable model.

2.3.1 Majorana-Dimer Configurations

To define the Majorana-dimer models, we first associate a Majorana operator γ_i, with $\gamma_i^\dagger = \gamma_i$ and $\{\gamma_i, \gamma_j\} = 2\delta_{ij}$, to each lattice site. The role of the dimers is to represent

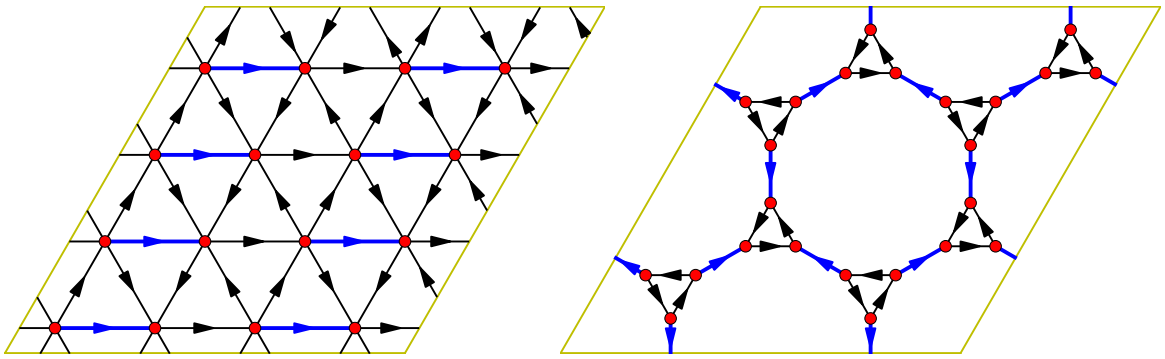

Figure 2.2: Kasteleyn orientation (arrows) and reference dimer configuration (blue bonds) on the triangular lattice (left panel) and the Fisher lattice (right panel).

pairings of Majorana modes into fermionic states. To uniquely define the pairings, we turn the lattice into an oriented graph by associating a direction to each edge of the lattice. A dimer configuration is then given as a collection of oriented bonds $D = \{(i, j)\}$ populated by dimers. The corresponding Majorana wavefunction $|F(D)\rangle$ is the ground state of the non-interacting Hamiltonian

$$H_F(D) = \sum_{(i,j)\in D} i\gamma_i\gamma_j. \tag{2.10}$$

In order to write down the fermionic wavefunction $|F(D)\rangle$, it is helpful to fix a reference set of fermion operators from which we will define a fermionic Fock space. We do that by picking a reference dimer configuration D_0 on the lattice. We assign a complex fermion f_q for each dimer in the reference configuration in the following way, using the previously fixed orientation: the Majorana at the tail of the arrow is taken to be γ_q^A and

the Majorana at the head of the arrow is taken to be γ_q^B, where

$$\gamma_q^A = f_q + f_q^\dagger$$
$$\gamma_q^B = i(f_q^\dagger - f_q).$$

The total dimension of this Fock space is $2^{N/2}$, where N is the number of lattice sites. Figure 2.2 shows examples of reference dimer configurations, illustrated by blue bonds, for the triangular and Fisher lattices.

Following these rules for the definition of fermion dimers, we see that the reference dimer configuration D_0 corresponds to the fermion vacuum state $|\mathbf{0}\rangle$. For some other dimer configuration D, non-trivial correlations in these fermionic states arise from the fact that for dimers in D that are not part of the reference state D_0, the ground state of H_F will pair Majoranas associated with different fermion operators f_q, $f_{q'}$. Relating the configuration D to D_0 by a transition graph, we see that these non-trivial fermion pairs occur along the closed loops of the transition graph, as shown in Fig. 2.3. If the fermions f_q of the reference configuration are viewed as the "physical" fermions, the coupling along such a loop resembles the pattern of entanglement between adjacent sites in the topological phase of the Kitaev chain [84].

Schematically, the wavefunction we are interested in is an "equal-weight" superposition of Majorana-dressed dimer configurations,

$$|\psi\rangle = \sum_D |F(D)\rangle|D\rangle. \tag{2.11}$$

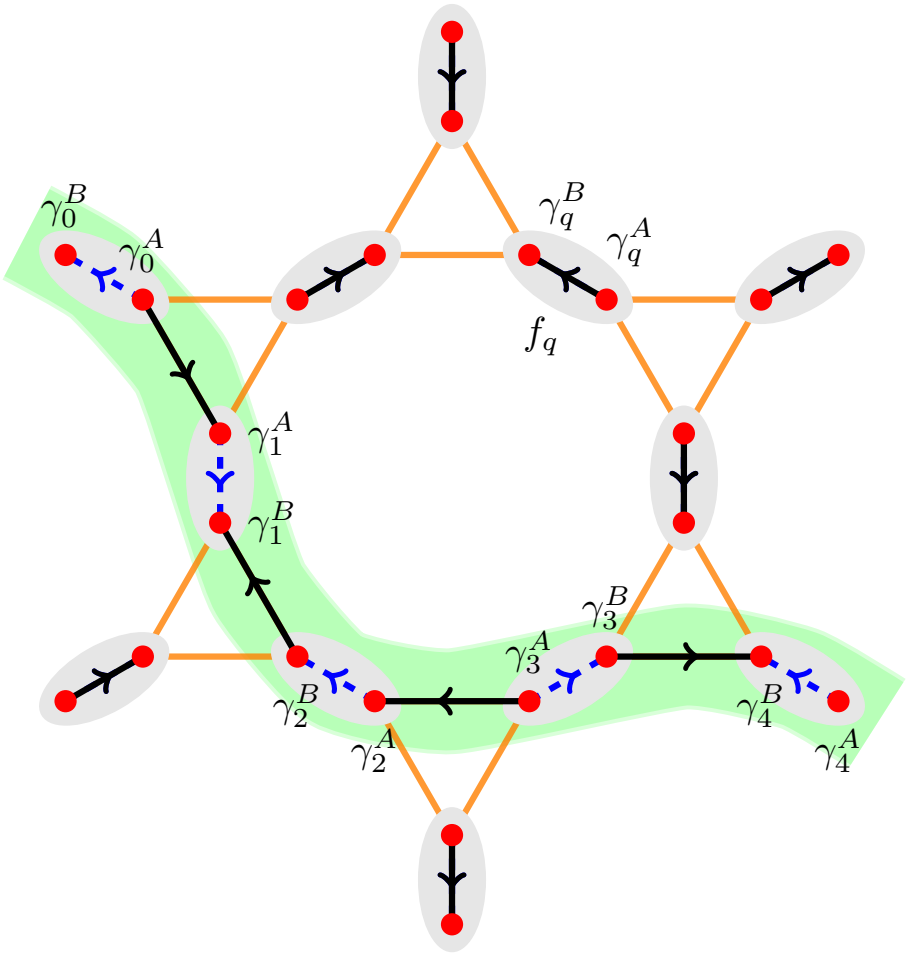

Figure 2.3: Illustration of Majorana pairings on the Fisher lattice. The green highlighted strip illustrates part of a transition-graph loop. Away from the loop, Majorana modes pair into the reference configuration; the corresponding fermion state has each of the f_q fermion unoccupied. Along the transition-graph loop, dimers are not in the reference configuration, and the Majoranas instead pair between neighboring complex fermions $f_q, f_{q'}$. The precise state of the fermions along the transition graph loop is the ground state of the Kitaev chain formed using Majoranas from neighboring sites. In the above example, this chain has the form $h = \ldots + i\gamma_0^A\gamma_1^A - i\gamma_1^B\gamma_2^B - i\gamma_2^A\gamma_3^A + i\gamma_3^B\gamma_4^B + \ldots$. The arrow orientation on the reference edges determines the identification of the two Majoranas at each site as γ_q^A or γ_q^B. The other arrow orientations determine the sign of the coupling between Majoranas.

Note that the definition of $|F(D)\rangle$ does not fix the overall phase of each $|F(D)\rangle$, so we will need to fix these phases in order to precisely define the "equal-weight" wavefunction.

We will also briefly consider a generalization of the wavefunction in Eq. (2.11) to include the "double semion" signs:

$$|\psi\rangle = \sum_D (-1)^{n(D)} |F(D)\rangle |D\rangle. \tag{2.12}$$

Again $n(D)$ is of the number of loops in the transition graph of D. As we will show, this wavefunction represents a phase of matter distinct from that of Eq. (2.11).

2.3.2 Fermion Parity

A basic criterion for the consistency of such a fermion wavefunction is that the total fermion parity is well-defined; for such a wavefunction to exist all superposed dimer configurations must carry the same total fermion parity. We will show that if the orientation for the bonds of the lattice is chosen correctly, this criterion can be met.

The fermion parity of each dimer state is described simply with a *clockwise-odd rule*: if the number of arrows pointing clockwise along a transition graph loop is odd, then the fermion parity of the corresponding state is even and vice versa. (For states with multiple loops in the transition graph, the total fermion parity is determined by combining the fermion parities of each loop separately.) Appendix 2.7 provides a simple proof of this fact. For planar graphs, a *clockwise odd* or *Kasteleyn* [82] orientation can always be picked such that all transition graph loops have an odd number of clockwise-pointing arrows; choosing this orientation guarantees all Majorana-dimer states have even fermion

parity. Since their introduction in Ref. [82], these orientations have been used extensively in the study of classical, bosonic dimer models. For a lattice on a higher-genus surface such as a torus, one can only guarantee that topologically trivial transition-graph loops are clockwise odd; an orientation with this property will be considered a Kasteleyn orientation. For any such orientation, topologically non-trivial loops will be either clockwise odd or even depending only on the $\mathbb{Z}_2$ winding numbers of the loop. Thus, the wavefunction in Eq. (2.11) will have definite fermion parity whenever the dimers in the sum belong to the same topological sector.

Let us briefly discuss the effects of different Kasteleyn orientations on the parity of each topological sector of dimers. Kasteleyn orientations related by a series of local flip moves, where each flip move flips all of the orientation arrows adjacent to a single site i, give equivalent fermion parities for each sector; this local flip move is equivalent to a local Z_2 gauge transformation on the Majoranas, $\gamma_i \to -\gamma_i$, which preserves the Majorana operators' commutation relations. To construct classes of Kasteleyn orientations unrelated by local flip moves, one can flip all of the arrows on edges along one of the non-trivial cycles of the torus. This leads to four inequivalent classes of Kasteleyn orientations. Since flipping the arrows along a non-trivial cycle is equivalent to switching the boundary conditions for the fermions from periodic to anti-periodic, the four classes of Kasteleyn orientations will be labeled by the boundary conditions periodic (P) or anti-periodic (A). The parity of the resulting Majorana-dimers depends only on the topological sector of the dimers and on the boundary conditions as summarized in Table 2.1. Similar

Dimer Sector	Boundary Cond. PP	PA	AP	AA
$(0,0)$	$+1$	$+1$	$+1$	$+1$
$(1,0)$	-1	$+1$	-1	$+1$
$(0,1)$	-1	-1	$+1$	$+1$
$(1,1)$	-1	$+1$	$+1$	-1

Table 2.1: The fermion parity $P_f = \pm 1$ of a Majorana-dimer state depends on the topological sector of the bosonic dimers (rows) and the boundary conditions for the fermions (columns). For the latter, 'P' and 'A' respectively denote periodic and antiperiodic boundary conditions. For example, PP indicates periodic boundary conditions on both cycles of the torus.

results can be derived for Kasteleyn orientations on higher genus surfaces, as detailed in Appendix 2.7.

For the rest of this chapter, we will fix a translationally invariant orientation on the torus and a reference dimer configuration for each lattice. In this case, the states of Majorana-dimers in the three topologically non-trivial sectors $(0,1), (1,0)$, and $(1,1)$ have odd fermion parities, while the trivial sector $(0,0)$ has even fermion parity. Here, the topological sectors are labelled by the parity of the winding numbers of the transition graph loops from the reference configuration.

2.3.3 Phase Consistency and Ground-State Degeneracy

The Majorana-dimer models that we discuss in detail below will follow the same general pattern consisting of terms that enforce the dimer constraint around a vertex, terms that flip dimer configurations, and finally potential terms. We extend the vertex terms to not only enforce the dimer constraint, but also to force the Majorana modes to pair according to the dimer configuration and consistent with the orientation. The ground-

state subspace $\mathcal{H}_r = \{|F(D)\rangle|D\rangle\}$ of these vertex terms is spanned by the set of allowed Majorana-dimer configurations. Additionally, we must extend the flip term B_p of the dimer model to include a fermionic part $\mathcal{B}_p$ that changes the Majorana pairings along with the dimer configurations. This term provides dynamics to the Majorana-dimers and will be constructed to ensure that the ground state of the full Hamiltonian forms an equal-weight superposition of dimers as in Eq. (2.11).

Let $\mathbf{B}_p \equiv B_p\mathcal{B}_p$ denote the combined boson-fermion flip term. (Here and below we use bold font for those operators that act on both the bosonic and fermionic Hilbert spaces.) Because of the bosonic part B_p, matrix elements $\langle F(D')|\langle D'|\mathbf{B}_p|F(D)\rangle|D\rangle$ within the restricted subspace $\mathcal{H}_r$ are non-zero only when dimer configurations D and D' differ by a single plaquette flip:

$$\langle F(D')|\langle D'|\mathbf{B}_p|F(D)\rangle|D\rangle = e^{i\varphi_{p,D}}\delta_{D',D_p}, \tag{2.13}$$

where dimer configurations D and D_p differ by flipping the plaquette p. Importantly, the fermionic part of the flip term contributes phases $e^{i\varphi_{p,D}}$, which are absent in the bosonic dimer model. We can characterize the effect of these phases by examining the matrix elements of the Hamiltonian in the reduced Hilbert space $\mathcal{H}_r$,

$$\begin{aligned} h_{DD'} &\equiv \langle F(D')|\langle D'|H|F(D)\rangle|D\rangle \\ &= Vn(D)\delta_{D',D} - t\sum_p e^{i\varphi_{p,D}}\delta_{D',D_p}. \end{aligned} \tag{2.14}$$

All of the off-diagonal matrix elements of h are generated by $\mathbf{B}_p$, while the diagonal

elements of h are the same as in the bosonic dimer model, i.e., the coefficient V times the number of flippable plaquettes $n(D)$. (In the Fisher-lattice dimer model, V appears as an overall constant and can be dropped.)

Note that $h_{DD'}$ can be viewed as a (possibly non-local) Hamiltonian acting on bosonic dimers without the accompanying Majoranas. The spectrum of our Hamiltonian in the restricted Hilbert space is the same as the spectrum of $h_{DD'}$ and is clearly unaffected by a redefinition $|F(D)\rangle \to e^{i\phi_D}|F(D)\rangle$. If such a redefinition could be made to satisfy $h_{DD'} = -t$ for all D, D' that differ by a single plaquette flip, then the spectrum of the Majorana-dimer model in the restricted Hilbert space would be *identical* to the bosonic dimer model for arbitrary t, V. In that case we say that the $h_{DD'}$ matrix is unfrustrated.

In the following models, we find that $h_{DD'}$ is indeed unfrustrated in systems with open boundary conditions—guaranteeing the existence of a choice of phases for $|F(D)\rangle$ where the ground state is given by Eq. (2.11) at the RK point. As detailed in Appendix 2.8, this choice is equivalent to adopting conventions for $|F(D)\rangle$ where the overlaps TODO

The situation is more subtle, however, on closed manifolds. On a torus we find that non-trivial phases

$$\Theta_{\{D_k\}} = \operatorname{Arg}\left(h_{D_1 D_2} h_{D_2 D_3} \dots h_{D_L D_1}\right) \tag{2.15}$$

can be generated by a sequence of dimer flip moves that start and end with the same dimer configuration. These phases cannot be removed by any redefinition $|F(D)\rangle \to e^{i\phi_D}|F(D)\rangle$ and thus frustrate the hopping. Remarkably, for each of our models, these non-trivial phases are occur only in one of the four topologically distinct sectors, namely

the $(0,0)$ sector. As a result, the minimum energy for the $(0,0)$ sector is greater than zero, while the other three sectors admit zero-energy ground states that are equal-weight superpositions of Majorana-dimer configurations.

Thus, while the bosonic quantum dimer models on these lattices have 4 degenerate ground states formed by superpositions of dimer configurations in each topological sector, the dynamics of the Majorana-dimers instead lead to three fermion-parity-odd ground states corresponding to superpositions of Majorana-dimer configurations in the $(0,1),(1,0)$, and $(1,1)$ sectors, with a finite gap to the $(0,0)$ sector as well as to all other states. This reduction in ground-state degeneracy from $4 \to 3$ is essential for reconciling the anyonic content of the topological order for our Majorana-dimer models discussed below. We also emphasize that the phases $\Theta_{\{D_k\}}$ can only be reproduced in the pure bosonic dimer model non-locally, while they appear from purely local dynamics in the Majorana-dimer models.

The next two sections explain the precise form of the dynamics for a commuting-projector model on the Fisher lattice and a frustration-free model on the triangular lattice. We will then use the ground state(s) on the Fisher lattice to diagnose the topological order.

2.3.4 Majorana Loop Model on a Honeycomb Lattice

Our construction on the Fisher lattice offers the advantage of having a vanishing correlation length and therefore being most amenable to both analytical and numerical methods.

As reviewed in Sec. 2.2, the quantum dimer model on this lattice is equivalent to a $\mathbb{Z}_2$ toric code on the associated honeycomb lattice. Dimer configurations on the Fisher lattice are in one-to-one correspondence with loops on the honeycomb lattice, as illustrated in Fig. 2.3. We will therefore formulate the model as a decorated toric-code model, where the ground-state wavefunction is an equal-weight superposition of closed loops dressed by Kitaev chains.

The fermionic degrees of freedom for the Majorana-dimer model on this lattice consist of one complex fermion f_e on each edge e of the honeycomb lattice, i.e., the complex fermions lie on the sites of a Kagome lattice. We split each fermion into two Majoranas via $f_e = \frac{1}{2}(\gamma_e^A + i\gamma_e^B)$. The Majoranas now form a Fisher lattice, and we take γ_e^A to sit at the tail of the edge's arrow. The Kasteleyn orientation in the right panel of Fig. 2.2 is such that all $\gamma^{A/B}$ are naturally associated with A/B sublattices. In the reference state all fermionic modes are empty $f_e^\dagger f_e = 0$. We pair up Majoranas according to the corresponding dimer configuration following the prescription sketched in Fig. 2.3 and described in the previous subsections.

We now define a frustration-free Hamiltonian whose ground states are given by the Majorana-loop wavefunctions introduced above. The Hamiltonian follows the same structure as the toric code Hamiltonian [Eq. (2.7)] in that one term penalizes configurations that violate the loop or Majorana-pairing constraints, while the second term ensures that the loops fluctuate and the ground state is an equal-weight superposition of all valid configurations. The terms that enforce the constraints are given as the following projectors

on the edges and the vertices of the honeycomb lattice:

$$
\begin{aligned}
A^{\hexagon}_{1,v} &= \frac{1}{2}\left(1+\prod_{e\in v}\sigma^z_e\right)\\
\mathbf{A}^{\hexagon}_{2,v} &= \sum_{\substack{e,e'\in v\\ e\neq e'}} \frac{1-\sigma^z_e}{2}\frac{1-\sigma^z_{e'}}{2}\frac{1+is_{e,e'}\gamma^\lambda_e\gamma^\lambda_{e'}}{2}\\
\mathbf{A}^{\hexagon}_{e} &= \frac{1-\sigma^z_e}{2}\frac{1+i\gamma^A_e\gamma^B_e}{2}.
\end{aligned}
\tag{2.16}
$$

Here $\lambda(v)$ in $\mathbf{A}^{\hexagon}_{2,v}$ indicates the sublattice type of the vertex v; $A^{\hexagon}_{1,v}$ enforces the loop constraint while $\mathbf{A}^{\hexagon}_{2,v}$, $\mathbf{A}^{\hexagon}_{e}$ enforce the Majorana-pairing constraints; and $s_{e,e'} = \pm 1$ encode the Kasteleyn orientation.

We then need the plaquette term to make the loops fluctuate, which in the purely bosonic model is achieved by the first term in Eq. (2.7). However, in the present case, we also need to change the Majorana pairings accordingly. This will be implemented by a fermionic plaquette operator $\mathcal{B}^{\hexagon}_p$, which only involves the Majoranas along the transition loop. We first define $\mathcal{B}^{\hexagon}_p$ through its matrix elements between states in the Fock space of valid Majorana-dimers corresponding to dimer configurations D and D_p that are related by flipping plaquette p [all other matrix elements will vanish when we include the contribution from the bosonic dimers and thus do not need to be specified; see Eq. (2.23) below]:

$$
\langle F(D_p)|\mathcal{B}^{\hexagon}_p|F(D)\rangle = \frac{\langle F(D_p)|F(D)\rangle}{|\langle F(D_p)|F(D)\rangle|},
\tag{2.17}
$$

It is easy to see that $\mathcal{B}^{\hexagon}_p$ is Hermitian and satisfies $\left(\mathcal{B}^{\hexagon}_p\right)^2 = 1$ when acting in the restricted Hilbert space. Since D and D_p only differ locally, one can expect that such

matrix elements can be generated by local operators.

Our specific choice of the $\mathcal{B}_p^{\hexagon}$ operator moves Majoranas along the transition loop using a series of braids. Let us label the Majoranas along the transition loop as $\gamma_1, \gamma_2, \ldots, \gamma_n$, in counterclockwise order. Here the only requirement is that γ_1 should be any of the Majoranas on the edges of the plaquette. We define $s_{i,i+1} = \pm 1$ according to the Kasteleyn orientation on the dimer connecting γ_i and γ_{i+1} (so that $is_{i,i+1}\gamma_i\gamma_{i+1} = 1$ either before or after the move), and generally $s_{ij} = s_{i,i+1} \cdots s_{j-1,j}$ for $1 \leq i < j \leq n$.

We can now define the fermionic part of the plaquette operator as

$$\mathcal{B}_p^{\hexagon}|F(D)\rangle = U_{1,2n-1} \cdots U_{1,5}U_{1,3}|F(D)\rangle. \tag{2.18}$$

Here, the unitary operator U_{ij} exchanges two Majoranas γ_i and γ_j:

$$U_{ij} = \frac{1 + s_{ij}\gamma_i\gamma_j}{\sqrt{2}} \tag{2.19}$$

$$U_{ij}\gamma_i U_{ij}^\dagger = s_{ij}\gamma_j \qquad U_{ij}\gamma_j U_{ij}^\dagger = -s_{ij}\gamma_i. \tag{2.20}$$

We show in Appendix 2.9 that the matrix elements of $\mathcal{B}_p^{\hexagon}$ on the Majorana-dimer subspace indeed satisfy Eq. (2.17), and are therefore independent of the position of the starting Majorana γ_1 on the transition loop. As explained in Appendix 2.9, the form of the $\mathcal{B}_p^{\hexagon}$ operator is not unique; however, any choice generates the same matrix elements given in Eq. (2.17).

In the restricted Hilbert space $\mathcal{H}_r$, the full plaquette operator $\mathbf{B}_p^{\hexagon}$ acts as

$$\begin{aligned}\mathbf{B}_p^{\hexagon}|\{\sigma^z\}\rangle|F\rangle &= B_p^{\hexagon}|\{\sigma^z\}\rangle \otimes \mathcal{B}_p^{\hexagon}|F\rangle \\ &= \left(\prod_{e\in p}\sigma_e^x\right)|\{\sigma^z\}\rangle \otimes \mathcal{B}_p^{\hexagon}|F\rangle.\end{aligned} \tag{2.21}$$

The most important properties of these operators are that they commute with each other within the restricted Hilbert space,

$$\mathbf{B}_p^{\hexagon}\mathbf{B}_{p'}^{\hexagon} = \mathbf{B}_{p'}^{\hexagon}\mathbf{B}_p^{\hexagon}, \tag{2.22}$$

and moreover that each squares to the identity, $(\mathbf{B}_p^{\hexagon})^2 = 1$, as noted earlier. The proof of the commutation relation is rather technical, so we refer interested readers to Appendix 2.9 for details.

As described thus far, the Hamiltonian is frustration-free, i.e., the ground state is a simultaneous eigenstate of all terms. Furthermore, since all terms commute on the restricted subspace $\mathcal{H}_r$, the stronger condition of a commuting-projector Hamiltonian in the full Hibert space can be obtained by conjugating the plaquette flip term with appropriate projectors into $\mathcal{H}_r$. In summary, the full Hamiltonian for this model is

$$\begin{aligned}H = &-J_v\sum_v\left(A_{1,v}^{\hexagon} + \mathbf{A}_{2,v}^{\hexagon}\right) - J_e\sum_e \mathbf{A}_e^{\hexagon} \\ &-t\sum_p \mathbf{B}_p^{\hexagon}\prod_{v\in p}A_{1,v}^{\hexagon}\mathbf{A}_{2,v}^{\hexagon}\prod_{e\in p}\mathbf{A}_e^{\hexagon}.\end{aligned} \tag{2.23}$$

We can also write down a Hamiltonian for the double-semion version of the wave-function given in Eq. (2.12), by modifying the bosonic part $B_p^{\hexagon}$ of the plaquette term to

the following [96]:

$$B_p^{\hexagon} = \prod_{e\in p} \sigma_e^x \cdot i^{\sum_{l\in p \text{ legs}} \frac{1-\sigma_l^z}{2}}. \tag{2.24}$$

Since this affects only the bosonic part, all properties related to the coupling to Majoranas are preserved.

Spectrum

Since all $\mathbf{B}_p^{\hexagon}$ commute with each other, they can be simultaneously diagonalized. The eigenstates can then be labeled by the list of eigenvalues $b_p = \pm 1$ of $\mathbf{B}_p^{\hexagon}$ for all p, with the energy $E = -\sum_p b_p$. The ground state(s) would naively correspond to $b_p = 1$, and all we need to do is to determine the ground-state degeneracy. However, there are additional constraints among the plaquette operators that must be fully taken into account to correctly count the ground states—which turn out to depend on the topology of underlying manifold and the global fermion parity.

First of all, let us consider placing the model in a disk. In this case, there are no additional relations between the plaquette operators, and there are no topologically nontrivial loop configurations. The restricted Hamiltonian $h_{DD'}$ considered in Sec. 2.3.3 is unfrustrated. So the ground state is unique, with a completely gapped spectrum.

Now consider the system on a torus. Loop states are divided into four topological sectors, distinguished by the parity of the winding number around the two non-trivial cycles. As we have discussed in Sec. 2.3.2, all Majorana states in a fixed topological sector of loops with given boundary conditions have the same fermion parity P_f. In

particular, for periodic boundary conditions, there are three degenerate ground states $(1,0),(0,1),(1,1)$ all having odd global fermion parity, and the $(0,0)$ sector has an even fermion parity. Interestingly, we observe that the only frustrating phases in the restricted Hamiltonian $h_{DD'}$ arise from sequences of dimer flips in the $(0,0)$ sector that flip every plaquette once. This can be translated into the following global constraint:

$$\prod_p \mathbf{B}_p^{\hexagon} = -P_f. \tag{2.25}$$

In the three fermion-parity odd sectors with $P_f = -1$ it is possible to have $b_p^{\hexagon} = 1$ for all plaquettes p simultaneously. This reproduces the expected three-fold ground-state degeneracy. In the even-parity sector $(0,0)$, at least one of the $b_p^{\hexagon}$ must be -1; superpositions of dimers in the $(0,0)$ sector form the lowest excited states of the model, with a degeneracy of N_p, since there are N_p different ways to violate exactly one plaquette. We can also interpret this result in terms of the quasiparticle excitations of the model: in the restricted Hilbert space on a closed manifold, a single fermion excitation is always bound to a plaquette flip $b_p^{\hexagon} = -1$.

2.3.5 Majorana-Dimer Model on a Triangular Lattice

The Majorana loop model introduced in the previous section, albeit exactly solvable, has quite complicated plaquette terms. In this section we describe a triangular-lattice Majorana-dimer model that exhibits much simpler plaquette terms and naturally generalizes the bosonic dimer Hamiltonian in Eq. (2.1). First we need to construct local terms in the Hamiltonian that favor the correct Majorana pairing for a given dimer configu-

ration. These are similar to the vertex and edge terms in the honeycomb lattice model and will not be repeated here. In the following we mainly consider the limit where these binding terms are dominant, allowing us to work within the restricted Hilbert space $\mathcal{H}_r$.

The potential term is diagonal in the dimer basis and does not involve Majorana operators; this piece therefore takes exactly the same form as in Eq. (2.1). The flip term must, however, once again modify the bosonic dimers along with the accompanying Majoranas, which can be accomplished by supplementing the bosonic flip operator with braid matrices as follows:

$$\mathbf{B}_p^{\triangle} = e^{i\theta_p} \left\{ \begin{array}{l} \left| \right\rangle\!\left\langle \right| \otimes U_{12} \\ \left| \right\rangle\!\left\langle \right| \otimes U_{12} \\ \left| \right\rangle\!\left\langle \right| \otimes U_{12} \\ \left| \right\rangle\!\left\langle \right| \otimes U_{12}. \end{array} \right. + \text{h.c.} \tag{2.26}$$

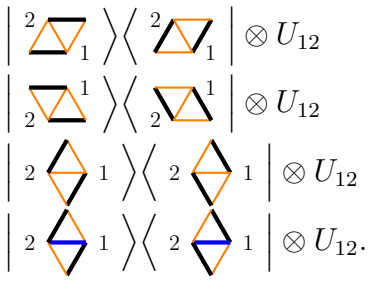

Here $U_{12} = (1 + s_{12}\gamma_1\gamma_2)/\sqrt{2}$, with the $\gamma_{1,2}$ operators labeled as above and s_{12} defined by the Kasteleyn orientation. The phase factors $e^{i\theta_p}$ are explained below — for now we simply note that $e^{i\theta_p} = e^{i\pi/4}$ for plaquettes whose interior bond coincides with the position of a reference dimer [blue bonds in Fig. 2.2], while for all other plaquettes $e^{i\theta_p} = 1$. One can check that the braid operators indeed give the desired Majorana pairings.

The full Hamiltonian, constructed analogously to the Fisher-lattice model of Eq. (2.23), reads

$$H = J_v \sum_v A_v^{\triangle} - J_e \sum_e \mathbf{A}_e^{\triangle} - \sum_p \left(t\mathbf{B}_p^{\triangle} - VC_p^{\triangle} \right), \tag{2.27}$$

where

$$\mathbf{A}_e^{\triangle} = \frac{1-\sigma_e^z}{2}\frac{1+is_{ij}\gamma_i\gamma_j}{2} \tag{2.28}$$

is the Majorana-dimer projector at an edge e that connects vertices i, j. There are two minor differences from Eq. (2.23): the additional potential term C_p from the bosonic dimer model on the triangular lattice is needed, and additional projectors previously tacked onto the flip term $\mathbf{B}_p$ no longer appear. This latter choice is made to simplify the Hamiltonian and does not affect the existence of frustration-free ground states; however, neighboring $\mathbf{B}_p$ terms do not commute in this model independent of whether the additional projectors are present or absent.

We include the phase factors $e^{i\theta_p}$ in Eq. (2.26) for the following reason: As explained in Appendix 2.8, with open boundary conditions (e.g., on a disk) the Majorana-dimer flip term as written is *unfrustrated* in the sense described in Sec. 2.3.3. It follows that in open boundary conditions the spectrum of the Majorana-dimer model within the restricted subspace is identical to that of the bosonic dimer model for any t/V. This mapping allows us to directly import known results for the bosonic dimer model to the present case. For example, at the RK point $t = V$, the ground state wavefunction is the equal-weight superposition of all Majorana-dimer states given in Eq. (2.11). Additionally, we see that no gapless edge modes are present, as found for the commuting-projector Majorana loop model discussed previously.

While these rigorous analytical statements do not simply extend to the torus, numerical evidence from small clusters strongly suggests that the topological ground-state

degeneracy also matches that of the Majorana loop model. We have checked numerically on 4×4, 6×4 and 4×6 lattices with periodic boundary conditions that the Majorana-dimer model remains unfrustrated in the $(1,0), (0,1), (1,1)$ sectors, but not in the $(0,0)$ sector. [More precisely, we verified by brute force that all non-trivial off-diagonal matrix elements of $h_{DD'}$ in Eq. (2.14) can be set equal to $-t$ in the first three sectors but not the last.] The frustration in the $(0,0)$ sector has a similar origin as the honeycomb lattice model: flipping a collection of plaquettes that covers the entire torus yields a π phase only in the $(0,0)$ sector, while all other loops of dimer moves accumulate no net phase.

We also performed exact diagonalizaton of our model on a 4×4 torus constrained to the restricted Hilbert space. At the RK point, we find one ground state in each of the $(1,0), (0,1), (1,1)$ sectors with exactly zero energy. The perfectly staggered states of the triangular lattice dimer model remain zero-energy states at this point as well, but only three ground states extend into the region $V < t$, as in the bosonic dimer model. Assuming the unfrustrated condition persists all the way to the thermodynamic limit, the ground states of the $(1,0), (0,1), (1,1)$ sectors are degenerate for the entire parameter region $V_c < V < t$ (where the bosonic dimer model is in the topological phase) when the vertex constraints are strictly enforced with $J_v, J_e \to \infty$. The lowest excited states in the exact diagonalization are the lowest-energy states in the $(0,0)$ sector—which for the 4×4 lattice at the RK point are 6-fold degenerate with energy $0.14t$. By analogy with the Majorana loop model, these lowest excited states cost an energy comparable to inserting a vison into the bosonic dimer model, and thus we expect they remain gapped away from

the other ground states in the thermodynamic limit. For the range of parameters where the ground state of the $(0,0)$ sector has higher energy than the other sectors, the model will have three topologically degenerate fermion-parity-odd ground states on a torus as well as gapped edges with open boundary conditions. Thus it is natural to expect that the resulting topological order is identical to the above Majorana loop model.

2.4 Identifying Topological Order

We are now ready to analyze the universal properties of the gapped states obtained above. We will present both analytical and numerical evidence that the topological order indeed corresponds to an Ising phase together with a chiral $p_x - ip_y$ superconductor. For theoretical expedience we primarily concentrate on the Fisher-lattice model, which allows many exact statements to be made given the exact solvability. We stress, however, that the results are expected to extend straightforwardly to the triangular lattice as well.

2.4.1 Ising topological quantum field theory review

We first review the Ising topological quantum field theory (TQFT). This topological phase—which is realized, e.g., in Kitaev's honeycomb model [85] or the $\nu = 1$ bosonic Pfaffian quantum Hall state [59, 60]—supports three types of anyons denoted by I, σ, ψ.

The nontrivial fusion rules are given by

$$\begin{aligned} \sigma \times \sigma &= I + \psi \\ \sigma \times \psi &= \sigma \\ \psi \times \psi &= I. \end{aligned} \tag{2.29}$$

It turns out that eight different bosonic topological phases exhibit these same fusion rules yet are distinguished by the topological twist factor of σ:

$$\theta_\sigma = e^{\frac{\pi i n}{8}}, \tag{2.30}$$

where n is an odd integer. (For any n the ψ twist factor is $\theta_\psi = -1$.) Since the corresponding chiral central charge is $c_- = n/2$, we label these phases as $\text{Ising}^{(n/2)}$. It is worth mentioning that the bulk-anyon braiding statistics is identical for n and $n + 16$. The usual Ising phase [85] is $\text{Ising}^{(1/2)}$ in this notation.

The modular matrices on a torus, which have been conjectured to uniquely identify

the topological phase [131, 21], are given by [85]

$$S = \frac{1}{2}\begin{pmatrix} 1 & 1 & \sqrt{2} \\ 1 & 1 & -\sqrt{2} \\ \sqrt{2} & -\sqrt{2} & 0 \end{pmatrix} \tag{2.31}$$

$$T = e^{-\frac{\pi i n}{24}}\begin{pmatrix} 1 & 0 & 0 \\ 0 & -1 & 0 \\ 0 & 0 & e^{\frac{\pi i n}{8}} \end{pmatrix}. \tag{2.32}$$

Here, T encodes the self-statistics (twist factors) of the quasi-particles, while S encodes the mutual statistics.

The ground-state degeneracy (GSD) of a topological phase on a genus-g surface can be obtained from the Verlinde formula [108]:

$$\text{GSD} = \sum_a S_{Ia}^{2-2g} \tag{2.33}$$

with a running over all quasiparticle types. For the Ising TQFT, we have $S_{II} = S_{I\psi} = \frac{1}{2}$ and $S_{I\sigma} = \frac{1}{\sqrt{2}}$, yielding

$$\text{GSD} = 2 \cdot \left(\frac{1}{2}\right)^{2-2g} + \left(\frac{1}{\sqrt{2}}\right)^{2-2g} = 2^{g-1}(2^g + 1). \tag{2.34}$$

The systems under consideration arise microscopically from fermionic matter, so it is useful to consider Ising phases supplemented by physical fermions, whose particle content is denoted by $\text{Ising}^{(n/2)} \times \{I, f\}$. Now the self-statistics of an anyon is only defined up to ± 1 since one can always attach a fermion f to the anyon. Therefore, the bulk anyon

properties are identical in this case for n and $n \pm 8$.

2.4.2 Ground-State Degeneracy on Closed Surfaces

The first piece of evidence that our Majorana-dimer models support Ising topological order comes from the ground-state degeneracy on closed surfaces. We have shown in Sec. 2.3 that systems defined on a torus host a three-fold ground-state degeneracy. We now further argue that on a genus-g surface the ground-state degeneracy is $2^{g-1}(2^g+1)$—exactly as for an Ising topological phase [see Eq. (2.34)].

Recall that the three-fold degeneracy on a torus arises because only odd-fermion-parity states can maximally satisfy all Hamiltonian terms, implying that one of the ground states of the pure bosonic dimer model is lifted to higher energy. Similar constraints hold on higher-genus surfaces. In fact, we will show that

$$\prod_p \mathbf{B}_p^{\hexagon} = (-1)^g P_f, \tag{2.35}$$

where g is the genus of the surface. This relation can be proven inductively. A surface Σ_g with genus g can be obtained from a genus-$(g-1)$ surface Σ_{g-1} by making a hole and gluing on an open torus T. Without losing generality, we can choose a trivalent graph such that the gluing hole coincides with a plaquette p_0. Assuming the relation (2.35) holds for Σ_{g-1}, we have

$$\mathbf{B}_{p_0}^{\hexagon} \prod_{\substack{p\in\Sigma_{g-1}\\ p\neq p_0}} \mathbf{B}_p^{\hexagon} = (-1)^{g-1} P_f(\Sigma_{g-1}). \tag{2.36}$$

For the open torus (punctured at p_0), using Eq. (2.25) we have

$$\mathbf{B}_{p_0}^{\hexagon} \prod_{\substack{p' \in \mathrm{T} \\ p' \neq p_0}} \mathbf{B}_{p'}^{\hexagon} = -P_f(\mathrm{T}). \tag{2.37}$$

We then glue the open torus and Σ_{g-1} together at p_0 to get Σ_{g-1}; after gluing the plaquette p_0 no longer belongs to the surface Σ_g. Multiplying the two relations and recalling that $(\mathbf{B}_{p_0}^{\hexagon})^2 = 1$ (in the restricted Hilbert space), we obtain

$$\prod_{p \in \Sigma_g} \mathbf{B}_p^{\hexagon} = (-1)^g P_f(\Sigma_{g-1}) P_f(\mathrm{T}) = (-1)^g P_f(\Sigma_g), \tag{2.38}$$

yielding Eq. (2.35) as claimed. Therefore, on a genus-g surface all ground states must have fermion parity equal to $P_f = (-1)^g$ in order to satisfy $\mathbf{B}_p^{\hexagon} = 1 \; \forall \; p$. Using the result of Appendix 2.7, the number of ground state on a genus-g surface is then $2^{g-1}(2^g + 1)$.

The fact that the ground states have global fermion parity equal to $(-1)^g$ can be understood from the presence of the "hidden" $p_x - ip_y$ superconductor: it is known that the ground state of a $p_x - ip_y$ superconductor on a torus with periodic boundary conditions has odd fermion parity [128]. Generalizing to a genus-g surface (which can be viewed as a connected sum of g tori), it is not hard to see that the ground state fermion parity should be $(-1)^g$. Since the Ising phase is purely bosonic, the ground state fermion parity of the Ising $\times$ $(p_x - ip_y)$ topological phase is also $(-1)^g$.

2.4.3 Fully Gapped Boundary to Vacuum

For the discussion of the edge physics, it is important to fix the background in which the phase desribed here arises. In the following, we will take the Majorana degrees of freedom in our model to arise microscopically from a medium with zero "background"

central charge, such as an array of Kitaev chains. As an alternative setup, the Majoranas could arise from a vortex lattice in a chiral p-wave superconductor with central charge $c = \pm 1/2$; results for the latter case can be obtained straightforwardly from the setup examined explicitly below.

Since we have shown that the Majorana loop state on the Fisher lattice is the ground state of a commuting-projector Hamiltonian, on a manifold with boundary there can not be any chiral edge modes [85]. We have also shown that the Majorana-dimer model on a triangular lattice is fully gapped with open boundary conditions. A fully gapped boundary implies the following: (a) The chiral central charge c_- must vanish. For Ising$\times$ $(p_x - ip_y)$ we indeed find that $c_- = \frac{1}{2} - \frac{1}{2} = 0$. (b) The topological order must contain a "Lagrangian subalgebra" [94, 87, 90, 40], namely a set of bosonic quasiparticles whose condensation eliminates the topological order completely. For the Ising $\times$ $(p_x - ip_y)$ topological phase, the particle content in the bulk can be conveniently represented by $\{I, \sigma, \psi\} \times \{I, f\}$ where f represents physical fermions. One can easily identify the Lagrangian subgroup as $\{I, \psi f\}$. Condensing the combination ψf identifies ψ with f and confines both σ and σf due to the nontrivial braiding statistics between σ and ψ [7]; the result is a trivial fermionic phase with particle content $\{I, f\}$. Together with the vanishing of the chiral central charge, this implies the existence of a fully gapped edge [10].

We notice that the ψf boson can be identified with the "vison" excitation of the lattice model. A vison in the Majorana loop model corresponds to a plaquette violation,

i.e. $B_p = -1$ for a certain p. Such excitations can be generated with a string operator along an open path P on the dual lattice:

$$W_v(P) = \prod_{j \in P} \sigma_j^z. \tag{2.39}$$

Here the product runs over all edges j intersecting with P. Notice that W_v does not involve any Majoranas, and in fact takes the same form as the string operator that generates plaquette excitations in the bosonic toric code. Therefore we expect the visons are bosonic.

2.4.4 Modular Matrices

The above arguments illustrate the consistency of the Ising $\times (p_x - ip_y)$ theory with the numerical observations thus far. However, we should notice that there are in fact four different types of topological order that are consistent with the ground-state degeneracy counting and existence of gapped boundaries. Following the notation laid out above, these correspond to $\text{Ising}^{(n/2)} \times (p_x - ip_y)^n$, where again n is an odd integer and $\text{Ising}^{(1/2)}$ denotes the usual Ising phase. All such phases have $c_- = 0$. Moreover, we should regard n and $n+8$ as representing the same phase [9] since their bulk anyon content is identical [recall Sec. 2.4.1]. Thus the four distinct states that we would like to discriminate amongst correspond to $n = 1, 3, 5, 7$.

To affirmatively and unambiguously identify the topological order, we characterize the topological properties of the bulk anyons through the modular S and T matrices, which can be extracted using the entanglement properties of ground states on the torus [160].

This calculation is done for the Majorana-dimer model on the Fisher lattice (Sec. 2.3.4), since the vanishing correlation length for the ground states negates the need to perform any finite-size scaling; for this reason, a minimal 2×2 lattice on a torus suffices. [For the triangular lattice model (Sec. 2.3.5), analogous calculations on small clusters (e.g., 4×4) were inconclusive most likely due to the system's finite correlation length; we leave for future work a thorough numerical investigation of this model using, for example, DMRG.] Because the ground states preserve the C_3 rotation symmetry of the Fisher lattice, we adopt the method developed in Refs. [160, 33, 13] to extract the modular matrix ST^{-1} using the action of a $2\pi/3$ rotation. This allows us to compute T and S individually given minimal assumptions about the form of these matrices. Without this rotational symmetry, we could instead use the methods of Ref. [161] to compute the S matrix and constrain the T matrix.

The presence of fermions in our model forces us to slightly modify the algorithm of Refs. [160, 33, 13] to determine the modular matrices S and T. There are two assumptions of these previous works that no longer hold. The first is that the modular matrix ST^{-1}, which corresponds to a $2\pi/3$ rotation, satisfies $(ST^{-1})^3 = 1$, i.e., $R_{2\pi/3}^3 = 1$. Naively, one might define the rotation through its action on the the fermionic operator f_q at site q by $R_{2\pi/3} f_q R_{2\pi/3}^{-1} = f_{R_{2\pi/3}(q)}$. This would imply that the representation of $R_{2\pi/3}$ on the ground state manifold would have to satisfy $R_{2\pi/3}^3 = 1$. In a fermionic topological phase, however, rotations can act in more subtle ways.

To see this, we note that S and T matrices must be understood as the non-Abelian

Berry phases associated with the degenerate ground states under adiabatic deformation of the system [42], and thus we should view $R_{2\pi/3}$ in the same way for the purpose of extracting modular matrices. As demonstrated in Ref. [157] via explicit Berry phase calculations, modular transformations of the ground state of a $(p_x - ip_y)^n$ superconductor with periodic boundary conditions along both directions are given by

$$S_{(p_x-ip_y)^n} = e^{\frac{\pi i n}{4}} \qquad\qquad T_{(p_x-ip_y)^n} = e^{-\frac{\pi i n}{12}}. \tag{2.40}$$

In particular, the ground state on a torus with C_3 symmetry satisfies

$$R^3_{\frac{2\pi}{3}} = (ST^{-1})^3 = (e^{\frac{\pi i n}{3}})^3 = (-1)^n. \tag{2.41}$$

Similarly, a ground state on a torus with C_4 symmetry satisfies $R^4_{\frac{\pi}{2}} = S^4 = (e^{\frac{\pi i n}{4}})^4 = (-1)^n$. The nontrivial right-hand side is a direct consequence of the fact that the ground state of a $(p_x - ip_y)^n$ superconductor has odd fermion parity when n is odd, because a 2π rotation acting on a fermion yields a -1 phase factor—where again the 2π rotation should be understood in the sense of an adiabatic Berry phase. We will need to account for this subtle Berry phase effect in our calculation.

One can also obtain these relations by microscopic considerations in our setup: Adiabatically rotating the system by 2π can be seen to be topologically equivalent to a series of braids that for every Majorana operator sends $\gamma_i \to -\gamma_i$, and thus the action of $R_{2\pi/3}$ on the Majorana operators must be taken to be

$$R_{2\pi/3}\gamma_i R^\dagger_{2\pi/3} = -\gamma_{R_{2\pi/3}(i)}. \tag{2.42}$$

Similar results can be obtained by viewing the system as a network of Majorana wires, where a 2π rotation is known to have the same effect [68].

The second assumption that while valid for bosonic theories, must be reconsidered in our case, is that the modular matrix S has a positive row and column corresponding to the vacuum anyon of the topological theory. While this assumption holds for bosonic topological orders, it can already be seen to fail for $S_{(p_x-ip_y)^n}$ above. The existence of a positive row and column can be used to extract S and T from a combination of modular matrices such as ST^{-1} [160], but without it some ambiguity in the precise values of S and T persists. While these issues could be remedied by expensive adiabatic computations of the S and T matrices, we will show below that the easier minimally entangled state (MES) calculations indeed contain enough information to distinguish the $\text{Ising}^{(n/2)} \times (p_x - ip_y)^n$ phases. The key fact is that the modular matrices of these theories, which read

$$\begin{aligned} S &= S_{\text{Ising}^{(n/2)}} \otimes S_{(p_x-ip_y)^n} \\ T &= T_{\text{Ising}^{(n/2)}} \otimes T_{(p_x-ip_y)^n} \end{aligned}, \tag{2.43}$$

will still have a row and column that are positive *modulo a constant prefactor*, since the difference from a bosonic theory is completely due to an overall phase contributed by the $(p_x - ip_y)^n$ sector. In the following, we will carefully step through the logic to show that the Majorana-dimer model of this chapter produces the topological phase with $n = 1$. Then we discuss how our construction can be modified to produce Hamiltonian and wavefunction representatives for each of the other odd n as well.

To proceed we must first choose a basis $\{|i\rangle\}$ for the three-dimensional ground-state manifold. We employ the ground states $|n_1, n_2\rangle$ of the Majorana-dimer model in each

topological sector with fixed winding numbers n_1, n_2 of the transition graph loops, where (n_1, n_2) takes one of the three values $(0,1),(1,0),(1,1)$. Notice that the overall phase of each ground state is arbitrary and that the winding number basis does not clearly specify the phases.

The second step of the analysis is to compute the overlap matrix $\langle i|R_{2\pi/3}|j\rangle$ for these ground states. As discussed above, we choose the rotation to act such that

$$R^3_{2\pi/3} = P_f. \tag{2.44}$$

One possible choice of phase convention is that the action of $2\pi/3$ rotations in the winding number basis takes the form

$$R_{\frac{2\pi}{3}} = \begin{pmatrix} 0 & 1 & 0 \\ 0 & 0 & -1 \\ 1 & 0 & 0 \end{pmatrix}, \tag{2.45}$$

which indeed satisfies $R^3_{2\pi/3} = -1$. Other phase conventions for the ground states yield a rotation matrix that differ from the above by conjugation with a diagonal matrix of phases, but do not affect the final answers below.

Accessing the anyon properties requires changing to the MES basis, i.e., the states that minimize the entanglement entropy with respect to a non-contractible cut of the torus [160], which are known to have a definite topological charge through the torus. The MES basis for the cuts shown in Fig. 2.4 was found by brute-force minimization of

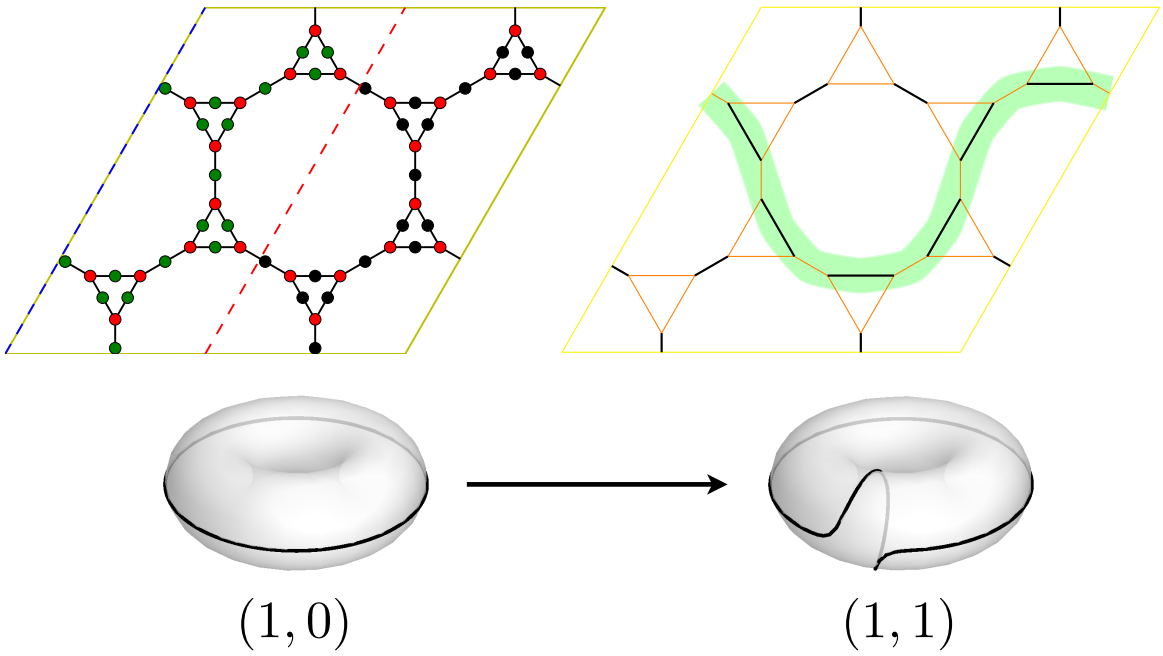

Figure 2.4: Upper left: The entanglement cut (red dashed line) used for the numerical calculations of the modular S and T matrices. Upper right: A dimer configuration belonging to the $(1, 0)$ topological sector. Bottom: The Dehn twist T permutes the sectors $(1, 0)$ and $(1, 1)$ while preserving the sector $(0, 1)$.

the entanglement entropy. Using the phase convention defined in Eq. (2.45), we find

$$\begin{aligned} |1\rangle &= \frac{1}{\sqrt{2}}(|1,0\rangle - e^{\frac{3i\pi}{8}}|1,1\rangle) \\ |2\rangle &= \frac{1}{\sqrt{2}}(|1,0\rangle + e^{\frac{3i\pi}{8}}|1,1\rangle) \\ |3\rangle &= |0,1\rangle. \end{aligned} \tag{2.46}$$

The entanglement entropies of the three MES's are respectively $3\ln 2$, $3\ln 2$, and $4\ln 2$. Generally speaking, a MES corresponding to anyon type a should have topological entanglement entropy $\gamma_a = 2\ln\frac{D}{d_a}$, where d_a is the quantum dimension of a and $D = \sqrt{\sum_a d_a^2}$ is the total quantum dimension [160]. For Ising anyons, we have $\gamma_I = \gamma_\psi = 2\ln 2, \gamma_\sigma = \ln 2$. Up to topological-sector-independent area law contributions, this is fully consistent with the calculated entanglement entropies if we identify $|3\rangle$ with the non-Abelian σ anyon.

In the MES basis, the $2\pi/3$ rotation becomes

$$R_{\frac{2\pi}{3}} = e^{\frac{3\pi i}{8}} \begin{pmatrix} \frac{1}{2} & -\frac{1}{2} & \frac{e^{\frac{\pi i}{4}}}{\sqrt{2}} \\ \frac{1}{2} & -\frac{1}{2} & -\frac{e^{\frac{\pi i}{4}}}{\sqrt{2}} \\ \frac{e^{-\frac{3\pi i}{8}}}{\sqrt{2}} & \frac{e^{-\frac{3\pi i}{8}}}{\sqrt{2}} & 0 \end{pmatrix}. \tag{2.47}$$

Following [33] and [13], in a topologically ordered phase a $2\pi/3$ rotation of a torus is represented by ST^{-1}, up to conjugation by a diagonal phase matrix D and a permutation matrix P:

$$R_{\frac{2\pi}{3}} = PD\left(ST^{-1}\right)D^\dagger P^\dagger. \tag{2.48}$$

The undetermined matrices D and P are due to the freedom to rephase each MES and reorder the MES's with the same topological entanglement entropy. Here both T and D are diagonal, while S is proportional to a matrix with all positive elements in the first row and column. We will consider this equation for each possible permutation P.

The above equation with $P = I$ allows us to determine S up to an overall phase by fixing the first row and column of $R_{\frac{2\pi}{3}}$ to be non-negative as in Eq. (2.45):

$$S = e^{i\eta} \begin{pmatrix} \frac{1}{2} & \frac{1}{2} & \frac{1}{\sqrt{2}} \\ \frac{1}{2} & \frac{1}{2} & -\frac{1}{\sqrt{2}} \\ \frac{1}{\sqrt{2}} & -\frac{1}{\sqrt{2}} & 0 \end{pmatrix}. \tag{2.49}$$

This is, not surprisingly, the S matrix of an Ising topological phase up to an overall phase. By matching this to Eq. (2.48), we can solve for T:

$$T = e^{i(\eta - \frac{3\pi}{8})} \begin{pmatrix} 1 & 0 & 0 \\ 0 & -1 & 0 \\ 0 & 0 & e^{\frac{\pi i}{8}} \end{pmatrix}. \tag{2.50}$$

This form of T and the knowledge that $c_- = 0$ pins down the topological order to be $\text{Ising}^{(1/2)} \times (p_x - ip_y)$. In particular, upon selecting $\eta = \frac{\pi}{4}$ these S and T matrices precisely agree with Eq. (2.43) with $n = 1$ [1].

Suppose that we instead choose a permutation matrix P that swaps the states $|1\rangle$ and $|2\rangle$ that possess identical topological entanglement entropies. While the same S results, we find that the T matrix now takes the form

$$T = e^{i(\eta + \frac{5\pi}{8})} \begin{pmatrix} 1 & 0 & 0 \\ 0 & -1 & 0 \\ 0 & 0 & e^{\frac{9\pi i}{8}} \end{pmatrix}. \tag{2.51}$$

Now the S and T matrices agree with Eq. (2.43) with $n = 9$ when $\eta = \frac{9\pi}{4}$. As discussed above, the phases $n = 1$ and $n = 9$ have the same bulk anyon content and should be identified; thus, this result is consistent with a unique identification of the topological phase from the modular matrices and chiral central charge.

[1] More generally, selecting $\eta = \frac{\pi x}{4}$, one can check that the S and T matrices will agree with those of $\text{Ising}^{(1/2)} \times (p_x - ip_y)^x$ whenever $x = 1 \mod 6$. This is due to the fact that 6 copies of $(p_x - ip_y)$ contributes a factor of 1 to the ST^{-1} matrix — thus, the modular matrix ST^{-1} does not completely determine the topological phase. Since 6 copies of $(p_x - ip_y)$ shift the chiral central charge c_- by 3, the additional knowledge that $c_- = 0$ fixes the appropriate factor $(p_x - ip_y)^x$.

Semion Variant

A similar calculation can be performed with the semion version of the dimer model introduced in Sec. 2.3.4. In this case, we instead find the MES to be given by

$$\begin{aligned} |1\rangle &= \frac{1}{\sqrt{2}}(|0,1\rangle + e^{\frac{7i\pi}{8}}|1,1\rangle) \\ |2\rangle &= \frac{1}{\sqrt{2}}(|0,1\rangle - e^{\frac{7i\pi}{8}}|1,1\rangle) \\ |3\rangle &= |1,0\rangle. \end{aligned} \tag{2.52}$$

Using this MES basis, the rotation matrix is written as

$$R_{\frac{2\pi}{3}} = e^{-\frac{\pi i}{8}} \begin{pmatrix} \frac{1}{2} & -\frac{1}{2} & -\frac{e^{\frac{\pi i}{4}}}{\sqrt{2}} \\ \frac{1}{2} & -\frac{1}{2} & \frac{e^{\frac{\pi i}{4}}}{\sqrt{2}} \\ \frac{e^{\frac{\pi i}{8}}}{\sqrt{2}} & \frac{e^{\frac{\pi i}{8}}}{\sqrt{2}} & 0 \end{pmatrix}. \tag{2.53}$$

This leads to the same S matrix as Eq. (2.49), but a distinct T matrix:

$$T = e^{i(\eta+\frac{\pi}{8})} \begin{pmatrix} 1 & 0 & 0 \\ 0 & -1 & 0 \\ 0 & 0 & e^{\frac{5\pi i}{8}} \end{pmatrix}. \tag{2.54}$$

With $\eta = \frac{5\pi}{4}$, the S and T now match the product of an Ising$^{(5/2)}$ theory and a $(p_x - ip_y)^5$ superconductor. Intuitively, the topological twist of σ shifts by i due to the attachment of a semion with exchange statistics i to the Ising anyon.

2.5 Generalizations to multiple Majoranas per site: 8-fold way

The eight topological phases Ising$^{(n/2)}$ for $n = 1, 3, 5, \ldots, 15$ discussed in Sec. 2.4.1 can be generated using a procedure of tensoring and condensation of bosons [7, 110]. Specif-

n	Phase	Twists
0	Toric Code	$1, -1, 1, 1$
2	$\mathrm{U}(1)_4$	$1, -1, e^{i\pi/4}, e^{i\pi/4}$
4	$\mathrm{U}(1)_2 \times \mathrm{U}(1)_2$	$1, -1, e^{i\pi/2}, e^{i\pi/2}$
6	$\mathrm{SO}(6)_1$	$1, -1, e^{3i\pi/4}, e^{3i\pi/4}$
8	$\mathrm{SO}(8)_1$	$1, -1, -1, -1$

Table 2.2: Even-n phases from the 16-fold way.

ically, tensoring n layers of Ising topological phases and condensing all of the bosons $\psi_i\psi_{i+1}$ formed from the combined fermions of neighboring layers gives the above progression of phases for odd n. For even $n \leq 8$, the phases listed in Table 2.2 occur. The phases for $8 < n < 16$ can be described as conjugates of the $n' = 16 - n$ phases listed in the table. The phase $n = 16$ has identical bulk particle content as Kitaev's toric code, and the pattern repeats with period 16. This is Kitaev's 16-fold way for gauged topological superconductors [85]. A similar progression of phases occurs using the fermionic $\mathrm{Ising}^{(1/2)} \times (p_x - ip_y)$ of this chapter as a generating state. However, as mentioned in Sec. 2.4.1, the pattern repeats after $n = 8$, since the topological twists are only well defined up to an overall sign in the presence of physical fermions.

To create Majorana-dimer wavefunctions for these $n > 1$ phases, it suffices to accompany each bosonic dimer with n Majorana-dimers instead of just 1. Specifically, each lattice site i now has n Majorana modes $\gamma_i^{(\alpha)}, \alpha \in \{1, \ldots, n\}$, and the n Majorana-dimers $(\gamma_i^{(\alpha)}, \gamma_j^{(\alpha)})$ are formed with the same orientation for each α. These wavefunctions can be viewed as dressed loop wavefunctions with n copies of the Kitaev chain along each loop. It is straightforward to write down an exactly solvable Hamiltonian for this state by generalizing the construction in Sec. 2.3.4.

To see that this procedure suffices, imagine n initially decoupled copies of the $n = 1$ model. Now add a coupling term between neighboring layers that energetically favors the loops in each layer to reside at the same location. Since the vison is just the violation of the plaquette term, and the simultaneous violation of plaquettes in two layers is invisible if loops are forced to surround the same plaquette in each layer, each of these terms drives a condensation transition that condenses the vison pairs $\psi_i\psi_{i+1}$ from neighboring layers (recall that the vison in each of the layer is the $\psi_i f$ particle). The end result of this process is the same as a single layer of loops dressed by n copies of the Kitaev chain.

We bolster the above argument by repeating the calculation of the modular matrices for the $n = 2$ case. Here we have four ground states—all with even fermion parity—that are formed from the four topological sectors. Using a phase convention where the rotation matrix takes the form

$$R_{\frac{2\pi}{3}} = \begin{pmatrix} 1 & 0 & 0 & 0 \\ 0 & 0 & 1 & 0 \\ 0 & 0 & 0 & 1 \\ 0 & 1 & 0 & 0 \end{pmatrix}, \tag{2.55}$$

the MES were found to be

$$\begin{aligned} |1\rangle &= \frac{1}{\sqrt{2}}(|1,0\rangle - e^{\frac{i\pi}{4}}|1,1\rangle) \\ |2\rangle &= \frac{1}{\sqrt{2}}(|1,0\rangle + e^{\frac{i\pi}{4}}|1,1\rangle) \\ |3\rangle &= \frac{1}{\sqrt{2}}(|0,0\rangle + |0,1\rangle) \\ |4\rangle &= \frac{1}{\sqrt{2}}(|0,0\rangle - |0,1\rangle). \end{aligned} \tag{2.56}$$

Using the same procedure as before, we find that the modular matrices satisfy

$$S = \frac{e^{i\eta}}{2} \begin{pmatrix} 1 & 1 & 1 & 1 \\ 1 & 1 & -1 & -1 \\ 1 & -1 & -i & i \\ 1 & -1 & i & -i \end{pmatrix}, \tag{2.57}$$

and

$$T = e^{i(\eta - \frac{3\pi}{4})} \begin{pmatrix} 1 & 0 & 0 & 0 \\ 0 & -1 & 0 & 0 \\ 0 & 0 & e^{\frac{\pi i}{4}} & 0 \\ 0 & 0 & 0 & e^{\frac{\pi i}{4}} \end{pmatrix}. \tag{2.58}$$

These are precisely the modular matrices of the $\mathrm{U}(1)_4 \times (p_x - ip_y)^2$ theory with $\eta = \frac{\pi}{2}$. As in Section 2.4.4, permutations of the MES produce different forms for the T matrix with the same S matrix, but these can all be regarded as representing the same bulk topological order. We note that a different exactly solvable model for this fermionic topological phase was studied in Ref. [64].

In the above construction, each additional layer and condensation of $\mathrm{Ising}^{(1/2)} \times (p_x - ip_y)$ increases n by 1. We can also *decrease* n by using a layer of a conjugate phase. One way to produce the conjugate phase is to act on the $n = 1$ state with an anti-unitary operator T, such as

$$TiT^{-1} = -i \tag{2.59}$$

$$T\gamma_i T^{-1} = \gamma_i. \tag{2.60}$$

This operation flips the sign of the coupling of all Majorana pairs, and so is equivalent to reversing the orientation of all Majorana-dimers. A repeat of the modular matrix

calculation confirms that this produces the $n = -1$ state, or equivalently the $n = 7$ state. Similarly, reversing the orientation of the $n = 5$ semion variant in Section 2.4.4 produces the $n = 3$ state. Thus our single-layer states and their conjugates suffice to generate all four of the n-odd topological phases.

One final check on the arguments in this section is provided by considering a layer construction of the $n = 1$ and $n = -1$ states. This is done similarly to the $n = 2$ construction, but with the orientation on one layer reversed. The modular matrix computation for this state produces the S and T matrix of the toric code topological order, which is the $n = 0$ phase of the 8-fold way.

2.6 Conclusion

In this chapter, we have introduced a new class of models, termed *Majorana-dimer* models. Starting from models of bosonic dimers, we introduce Majorana modes on the edges of the lattice and couple them to the dimers such that the Majorana modes always pair up according to the dimer configurations. We explicitly construct two frustration-free Hamiltonians governing the dynamics of the dimers: an exactly solvable Hamiltonian consisting of commuting projectors on the Fisher lattice, and a much simpler Hamiltonian on the triangular lattice. We characterize the universal topological properties of the models using ground-state degeneracy on closed surfaces and modular transformations, and show that the resulting gapped phases realize Ising $\times$ $(p_x - ip_y)$ topological order in the simplest case, and phases related to Kitaev's 16-fold way in the general case. All

these phases have gapped boundaries and cannot arise in purely bosonic systems. We note that similar results have been obtained by Walker and Wang [149]. It is interesting to ask whether the phase described here is part of an even larger family of systems. A natural extension of our work would be to replace the Majorana modes by parafermionic generalizations [44, 11, 35, 31, 100, 4], and couple them to dimers to form a phase with deconfined excitations that harbor parafermion zero modes.

The models we study can be viewed as gauged fermionic SPTs protected by an on-site $\mathbb{Z}_2$ symmetry [125, 134, 156, 62]. This is particularly clear in the Fisher lattice model: performing a duality transformation sends $\sigma_e^z \leftrightarrow \tau_p^z \tau_q^z$, where p and q label the two plaquettes adjacent to e and τ's are Ising spins on the dual lattice. This dual model has a global $\mathbb{Z}_2$ symmetry generated by $\prod_p \tau_p^x$, and loops in the original model correspond to Ising domain walls in the dual model. A commuting-projector model for this fermion SPT was recently found in Ref. [141], which is closely related to the Fisher lattice model studied in this chapter via the above duality transformation. Moreover, the generalization to n Majoranas per site discussed in Sec. 2.5 can also be dualized to capture other $\mathbb{Z}_2$ fermionic SPT's, and the 8-fold way precisely corresponds to the $\mathbb{Z}_8$ classification of the SPT's [134, 62]. These phases can also be realized with non-interacting fermions: consider the $n = 1$ case and spin-1/2 electrons. Spin-up (down) electrons form $p_x + ip_y$ ($p_x - ip_y$) superconductors. The $\mathbb{Z}_2$ symmetry is generated by $(-1)^{N_\uparrow}$, i.e., conservation of the fermion parity of spin-up electrons. Gauging the $\mathbb{Z}_2$ symmetry would turn the $p_x + ip_y$ superconductor into an Ising phase, and therefore the gauged SPT is indeed

Ising $\times$ $(p_x - ip_y)$.

Our results have important consequences for the question of which topological phases of matter can be represented with tensor network states of small bond dimension. Previously, it has been shown that all bosonic topological phases with fully gapped boundaries have exact PEPS representations [22, 63, 24]. At the same time, there is evidence that topological phases with chiral edges and exponentially decaying bulk correlations—including the Ising theory whose particle content is the same as the phase described here—cannot be efficiently represented as tensor networks [148, 38, 154]. Crucially, given that we have explicitly constructed frustration-free Hamiltonians, the phase of matter discussed in this chapter is likely to be described exactly by a PEPS of relatively small bond dimension. Our construction therefore suggests that the use of fermionic systems allows a broader class of topological orders to be desribed as tensor networks than previously known. These phases may also be more susceptible to many-body localization [76, 15, 124, 123].

Finally, it would be very interesting to realize the Majorana-RVB physics encapsulated in Eq. (2.11), and the resulting Ising $\times$ $(p_x - ip_y)$-type topological order, in a purely fermionic microscopic setting (*without* the accompanying bosonic dimers). In this context, our results highlight the possibility of a topological superconductor with p-wave pairing that breaks time reversal symmetry, but nevertheless has a gapped edge. This could be consistent with phenomenology observed in strontium ruthenates [105]. Barring the admittedly far-fetched possibility of relevance to this material, one could obtain

more natural models for this phase in engineered quantum systems. As a concrete physical realization we imagine, for example, a triangular Abrikosov vortex lattice in a two-dimensional $p_x + ip_y$ superconductor where each vortex hosts a Majorana zero mode [128] (for possible physics arising in such systems, see e.g., Refs. [61, 103, 92, 32]), or an appropriately arranged array of Majorana nanowires [84, 104, 112, 12]. In each case, we at least have the correct Majorana degrees of freedom at hand. In the former case, there is also similar sign structure in the couplings of these Majoranas. The effective coupling of Majorana vortex modes through the $p_x + ip_y$ superconductor determined by the overlap integrals of the mode wavefunctions have phases that satisfy the clockwise-odd rule, which in this context has been labeled the Grosfeld-Stern rule [61, 32]. Furthermore, the phase of individual t_{ij} depends on a choice of branch cuts of the underlying superfluid's order parameter which start and terminate at the vortices; these branch cuts play a role similar to the reference dimer configuration in our chapter. The similarity suggests that the Ising$\times(p_x - ip_y)$ phase could appear in the phase diagram of the Majorana modes in a vortex lattice with (beyond quadratic) interactions induced through the superconductor.

The question of whether one can design suitable interactions among these zero modes to induce an Ising $\times$ $(p_x - ip_y)$-type phase must be addressed in future work, but the results presented here provide new motivation to address this problem.

2.7 Fermion Parity Details: Clockwise-Odd Rule and State Counting

Let us prove the clockwise-odd rule for fermion parity on a transition loop. Consider a transition loop containing $2N$ Majoranas. Assume that the reference dimer configuration corresponds to the pairings $is_{2j-1,2j}\gamma_{2j-1}\gamma_{2j} = 1$ with $j = 1, \ldots, N$, and that the new configuration has $is_{2j,2j+1}\gamma_{2j}\gamma_{2j+1} = 1$. Denoting the loop fermion parity operator by $\hat{P}_{\text{loop}}$, the fermion parity of the new state $|\Psi\rangle$ is

$$\begin{aligned}
\langle\Psi|\hat{P}_{\text{loop}}|\Psi\rangle &= \langle\Psi|\prod_{j=1}^{N} is_{2j-1,2j}\gamma_{2j-1}\gamma_{2j}|\Psi\rangle \\
&= i^N \prod_{j=1}^{N} s_{2j-1,2j}\langle\Psi|\gamma_1\gamma_2\cdots\gamma_{2N-1}\gamma_{2N}|\Psi\rangle \\
&= -\, i^N \prod_{j=1}^{N} s_{2j-1,2j}\langle\Psi|\gamma_2\cdots\gamma_{2N-1}\gamma_{2N}\gamma_1|\Psi\rangle \\
&= -\prod_{j=1}^{2N} s_{j,j+1}\langle\Psi|\prod_{j=1}^{N} is_{2j,2j+1}\gamma_{2j}\gamma_{2j+1}|\Psi\rangle \\
&= -\prod_{j=1}^{2N} s_{j,j+1}.
\end{aligned} \tag{2.61}$$

This is exactly the clockwise-odd rule quoted in Sec. 2.3.2.

We now consider the fermion parity of Majorana-dimer states on a high-genus surface, assuming periodic boundary conditions. There are 2^{2g} topological sectors of dimer configurations. Notice that a genus-g surface can be viewed as the connected sum of g tori. Each torus inherits the periodic boundary conditions so there are three states with odd fermion parity and one with even fermion parity. Therefore, the total number of

states with even fermion parity is

$$\begin{aligned}\sum_{k=0}^{k\leq[g/2]}\binom{g}{2k}3^{2k} &= \frac{1}{2}[(3+1)^g+(-1)^g(3-1)^g] \\ &= \frac{1}{2}[2^{2g}+(-1)^g 2^g] \\ &= 2^{g-1}[2^g+(-1)^g],\end{aligned} \tag{2.62}$$

and the total number of states with odd fermion parity is $2^{2g}-2^{g-1}[2^g+(-1)^g] = 2^{g-1}[2^g-(-1)^g]$.

2.8 Majorana-Dimer Model with Open Boundary Conditions

In Sec. 2.3.3 we defined a map from the Majorana-dimer model in the restricted Hilbert space to the bosonic dimer Hamiltonian via the nonlocal transformation $|F(D)\rangle|D\rangle \to |D\rangle$. Recall that matrix elements for the fermionic part of the flip term are given by

$$h_{DD'} = -\langle F(D')|\mathcal{B}_p|F(D)\rangle. \tag{2.63}$$

We fix the innate phase ambiguity for $|F(D)\rangle$ by the following convention. Define $|\mathbf{0}\rangle$ as the vacuum of fermions in the reference configuration. The overlap $\langle\mathbf{0}|F(D)\rangle$ is always non-zero with open boundary conditions: if we examine the transition graph between D and the reference dimer configuration, $|F(D)\rangle$ is essentially the ground state of Kitaev chains on the transition loops, or in other words the state obtained by applying $\prod_{e=(i,j)\in l}\frac{1+is_{ij}\gamma_i\gamma_j}{2}$ along each transition loop l. In our system with open boundary conditions, the ground state of each Kitaev chain has even fermion parity, and it is a

well-known fact that the wavefunction of such chains is an equal-weight superposition (up to signs) of all fermion occupation numbers with given parity, including the vacuum. Thus with open boundary conditions $\langle \mathbf{0}|F(D)\rangle$ is indeed always non-zero, and we select phase conventions for $|F(D)\rangle$ such that this overlap is real and positive.

Consider now the action of triangular-lattice flip term as defined in Eq. (2.26) for a certain plaquette p, and let the dimer configurations before and after the dimer flip by D and D', respectively. (We assume that D is flippable.) Denote the fermionic part of $\mathbf{B}_p$ by

$$\mathcal{B}_p = e^{is_{1p}\theta_p}\left(\frac{1+s_{2p}\gamma_{p,1}\gamma_{p,2}}{\sqrt{2}}\right), \tag{2.64}$$

where $\gamma_{p,1}$ and $\gamma_{p,2}$ sit opposite the interior bond of the plaquette and $s_{1,2p}$ are signs that depend on the specific plaquette flip under consideration. [This expression is somewhat schematic but all we need here; see Eq. (2.26) for the precise form]. The main objective of this Appendix is to prove that with open boundary conditions

$$|F(D')\rangle = \mathcal{B}_p|F(D)\rangle. \tag{2.65}$$

Clearly $|F(D')\rangle$ and $\mathcal{B}_p|F(D)\rangle$ can at most differ by a phase factor, as they are both normalized and correspond to the same pairings of Majoranas. So to prove the equality it suffices to show that $\langle \mathbf{0}|\mathcal{B}_p|F(D)\rangle > 0$.

One can prove this relation by examining the transition graph between the configuration D and the reference dimer configuration. There are three possible situations:

1. The first case arises when two dimers in the plaquette p of the configuration D belong to different transition loops, e.g.,

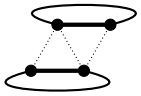
,

and flipping them decreases the total number of loops in the graph by one. Recall that the fermionic wavefunction of each transition loop in D can be viewed as a Kitaev chain, and that the Kastelyn orientation guarantees that the fermion parity of the wavefunction (only counting those Majoranas on the transition loop) must be even. Applying a Majorana operator γ_i to a given loop flips the loop's parity and yields a wavefunction that is orthogonal to any wavefunction where that loop has even parity—including the reference state. Therefore we conclude that $\langle \mathbf{0}|\gamma_{p,1}\gamma_{p,2}|F(D)\rangle = 0$ in this case. We should also notice that $e^{i\theta_p} = 1$. In our model the phase $e^{i\theta_p}$ is nontrivial only when the interior bond in the flipped plaquette coincides with a reference dimer. But if that is the case then the two dimers that we flip must initially belong to the same transition loop, contradicting our assumption. We thus conclude from Eq. (2.64) that

$$\langle \mathbf{0}|\mathcal{B}_p|F(D)\rangle = \frac{1}{\sqrt{2}}\langle \mathbf{0}|F(D)\rangle > 0. \tag{2.66}$$

2. When the two dimers in the plaquette p originate from the same transition loop, the associated Kasteleyn arrows become important. From Fig. 2.2 we see that the arrows on the two dimers can orient either parallel or antiparallel. The second case we consider arises when these arrows are antiparallel, e.g.,

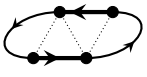

Now the plaquette flip increases the number of loops by one. This is exactly the inverse process of flipping two dimers belonging to different loops, so we can simply adopt the argument in case 1 above to arrive at the same conclusion in Eq. (2.66).

3. The third case arises when two dimers with parallel Kasteleyn arrows belong to the same loop, e.g.,

With open boundary conditions, such configurations can only arise when the transition loop connects the two dimers directly via the interior bond of the plaquette, which in turn implies that the interior bond belongs to the reference dimer configuration. (Notice that with periodic boundary conditions this assertion no longer holds. The transition loop can wind around a non-contractible cycle to accommodate two dimers with parallel Kasteleyn arrows). In this case we have $i\gamma_{p,1}\gamma_{p,2}|\mathbf{0}\rangle = \pm|\mathbf{0}\rangle$ by definition and hence $\langle\mathbf{0}|\mathcal{B}_p|F(D)\rangle = e^{\mp i\theta_p}e^{\pm i\pi/4}\langle\mathbf{0}|F(D)\rangle$. The additional phase factor $e^{\pm i\pi/4}$ is exactly cancelled by our choice of $\theta_p = \pi/4$, and again we have $\langle\mathbf{0}|\mathcal{B}_p|F(D)\rangle = \langle\mathbf{0}|F(D)\rangle > 0$.

We have now demonstrated that Eq. (2.65) holds for systems with open boundary conditions. Inserting this relation into Eq. (2.63) immediately yields $h_{DD'} = -\langle F(D')|\mathcal{B}_p|F(D)\rangle = -1$ (again with open boundary conditions) whenever D is flippable to D' by B_p. So the corresponding dimer model is unfrustrated.

We would like to remark that the proof here does not rely on the specific geometry of the lattice in an essential way, and can be readily adapted to Majorana-dimer flips on tetragonal plaquettes in other lattices provided one keeps track of the phase factor appearing in the last case. Appendix 2.9.2 describes a procedure for adapting these tools to the Fisher lattice.

2.9 Fermionic Plaquette Operators on the Fisher Lattice

2.9.1 Matrix Elements of the Fermionic Plaquette Operator

Here we will show that the matrix elements of $\mathcal{B}_p^{\hexagon}$, again defined through

$$\mathcal{B}_p^{\hexagon}|F(D)\rangle = U_{1,2n-1}\cdots U_{1,5}U_{1,3}|F(D)\rangle, \tag{2.67}$$

indeed conform to Eq. (2.17) as claimed in the main text. It suffices to focus only on Majoranas within a loop that is cycled by $\mathcal{B}_p^{\hexagon}$. Consider such a loop in the initial configuration D that contains $2n$ Majoranas paired up as $is_{2j-1,2j}\gamma_{2j-1}\gamma_{2j} = 1$ where $j = 1,\ldots,n$. Defining parity projectors

$$P_{i,j} = \frac{1 + is_{ij}\gamma_i\gamma_j}{2}, \tag{2.68}$$

we then have

$$P_{2j-1,2j}|F(D)\rangle = |F(D)\rangle, \forall\ j. \tag{2.69}$$

A plaquette move initiated by $\mathcal{B}_p^{\hexagon}$ (and its bosonic-sector counterpart $B_p^{\hexagon}$) sends $D \to D'$ and yields a new Majorana dimerization pattern with

$$P_{2j,2j+1}|F(D')\rangle = |F(D')\rangle, \forall\ j. \tag{2.70}$$

Next we deduce the action of the braid operators $U_{i,j}$ in Eq. (2.67). Because $is_{12}\gamma_1\gamma_2 = 1$ when acting on $|F(D)\rangle$ (and using $s_{23} = s_{12}s_{13}$), we have

$$\begin{aligned} U_{1,3}|F(D)\rangle &= \frac{1 + s_{13}\gamma_1\gamma_3 \cdot is_{12}\gamma_1\gamma_2}{\sqrt{2}}|F(D)\rangle \\ &= \sqrt{2}P_{2,3}|F(D)\rangle. \end{aligned} \tag{2.71}$$

After the exchange, the state $U_{1,3}|F(D)\rangle$ now has $is_{23}\gamma_2\gamma_3 = 1$ and $is_{14}\gamma_1\gamma_4 = 1$ owing to the projector $P_{2,3}$. Iterating this procedure for the remaining braid operators yields

$$\mathcal{B}_p^{\hexagon}|F(D)\rangle = (\sqrt{2})^{n-1}P_{2n-2,2n-1}\cdots P_{4,5}P_{2,3}|F(D)\rangle. \tag{2.72}$$

With the aid of Eq. (2.70) we therefore immediately obtain

$$\langle F(D')|\mathcal{B}_p^{\hexagon}|F(D)\rangle = (\sqrt{2})^{n-1}\langle F(D')|F(D)\rangle. \tag{2.73}$$

Finally, we note that while the phase of the overlap $\langle F(D')|F(D)\rangle$ is ambiguous, the norm is fixed:

$$|\langle F(D')|F(D)\rangle| = 2^{(1-n)/2}. \tag{2.74}$$

This relation allows us to rewrite Eq. (2.73) in the desired form,

$$\langle F(D')|\mathcal{B}_p^{\hexagon}|F(D)\rangle = \frac{\langle F(D')|F(D)\rangle}{|\langle F(D')|F(D)\rangle|}. \tag{2.75}$$

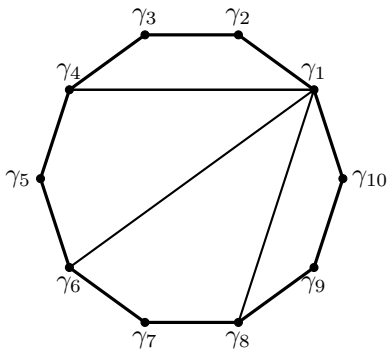

Figure 2.5: An example of tetragonalization for $t = 4$. A flip operator for the original 10-sided polygon may be decomposed into a series of elementary flips for each tetragon. In this representation the tetragonal plaquettes, from top to bottom right, respectively correspond to $U_{1,3}$, $U_{1,5}$, $U_{1,7}$ and $U_{1,9}$ in Eq. (2.67).

2.9.2 Commutation Relations of Plaquette Operators

The goal of this section is to prove that $\mathcal{B}_p^{\hexagon}\mathcal{B}_{p'}^{\hexagon} = \mathcal{B}_{p'}^{\hexagon}\mathcal{B}_p^{\hexagon}$ in the restricted Hilbert space. As a primer it is very useful to first develop a geometric understanding of the operator $\mathcal{B}_p^{\hexagon}$ by drawing an analogy to the plaquette operator in the triangular-lattice model. Imagine we partition the polygon enclosed by a transition loop into t tetragons by connecting site 1 with sites $4, 6, \ldots, t-1$; see Fig. 2.5 for an illustration. One can view $\mathcal{B}_p^{\hexagon}$ as implementing a series of elementary dimer flips through the tetragons as defined precisely as on the triangular lattice (first $[1, 2, 3, 4]$, then $[1, 4, 5, 6]$, and so on), provided we allow dimers to occupy the auxiliary edges at intermediate steps. The advantage of this 'tetragonalization' is that we can easily track the phase of the fermionic state at each step (by looking at the overlap with some reference state) using the rules explained in Appendix 2.8.

With this geometric picture in hand, given a Majorana-dimer state $|F(D)\rangle$ one can

write down a representation $\mathcal{B}^{\hexagon}_{p,T}$ of the desired plaquette move acting on $|F(D)\rangle$ using some tetragonalization T of the polygon. In fact they are all equivalent in the restricted subspace, in the sense that for arbitrary tetragonalizations T_1 and T_2 and any dimer covering D, $\mathcal{B}^{\hexagon}_{p,T_1}|F(D)\rangle = \mathcal{B}^{\hexagon}_{p,T_2}|F(D)\rangle$. One can see this as follows. By construction, $\mathcal{B}^{\hexagon}_{p,T}|F(D)\rangle$ gives a state corresponding to the same pairing of Majoranas for any tetragonalization T. Two tetragonalizations T_1 and T_2 thus generically give $\mathcal{B}^{\hexagon}_{p,T_1}|F(D)\rangle = e^{i\phi_{p,D}}\mathcal{B}^{\hexagon}_{p,T_2}|F(D)\rangle$. One can conveniently isolate the phase factor on the right by taking an overlap with $|F(D)\rangle$:

$$e^{i\phi_{p,D}} = \frac{\langle F(D)|\mathcal{B}^{\hexagon}_{p,T_1}|F(D)\rangle}{\langle F(D)|\mathcal{B}^{\hexagon}_{p,T_2}|F(D)\rangle}. \tag{2.76}$$

It turns out, however, that $\langle F(D)|\mathcal{B}^{\hexagon}_{p,T}|F(D)\rangle > 0$ independent of the tetragonalization T. We can view this expectation value as the overlap between $\mathcal{B}^{\hexagon}_{p,T}|F(D)\rangle$ and a reference state $|F(D)\rangle$. (Using this reference state instead of $|\mathbf{0}\rangle$ is convenient here since the former more efficiently captures local effects of $\mathcal{B}^{\hexagon}_{p,T}$.) In each elementary step, the tetragon dimer flip term with associated braid operator $U_{1,2j+1}$ changes the number of loops in the corresponding transition graph—i.e., each step falls into either case 1 or 2 from Appendix 2.8. Thus the overlap with $|F(D)\rangle$ remains positive throughout so that $\langle F(D)|\mathcal{B}^{\hexagon}_{p,T}|F(D)\rangle > 0$ generically as claimed. This property allows us to conclude that $\phi_{p,D} = 0$ in Eq. (2.76), which in turn proves that $\mathcal{B}^{\hexagon}_{p,T_1}|F(D)\rangle = \mathcal{B}^{\hexagon}_{p,T_2}|F(D)\rangle$. We can therefore safely drop the subscript T hereafter. The freedom of choosing any tetragonalization greatly simplifies the proof below.

We turn now to commutation of $\mathcal{B}^{\hexagon}_{p}$'s in the restricted subspace. Because the bosonic

pieces of the flip term commute, one can readily see that $\mathcal{B}_p^{\hexagon}\mathcal{B}_{p'}^{\hexagon}|F(D)\rangle$ and $\mathcal{B}_{p'}^{\hexagon}\mathcal{B}_p^{\hexagon}|F(D)\rangle$ give states with identical Majorana pairing. In other words, these states at most differ by a complex phase factor. One can show that the phases are also the same by analyzing the matrix elements $\langle F(D)|\mathcal{B}_p^{\hexagon}\mathcal{B}_{p'}^{\hexagon}|F(D)\rangle$ and $\langle F(D)|\mathcal{B}_{p'}^{\hexagon}\mathcal{B}_p^{\hexagon}|F(D)\rangle$, in a spirit similar to the proof in the previous paragraph. While there are naively many different configurations to consider, several simplifications streamline the analysis. First, we only need to consider the cases in which p and p' are neighboring plaquettes, since the commutation relation follows trivially otherwise. Second, we can focus exclusively on the Majoranas that may be affected by both $\mathcal{B}_p^{\hexagon}$ and $\mathcal{B}_{p'}^{\hexagon}$, as shown in the following diagram:

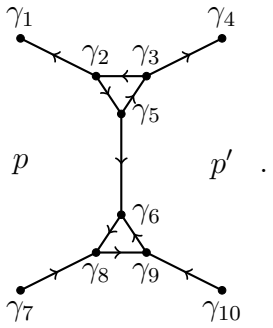

And finally, it suffices to check only four different types of neighboring plaquette configurations. For each one we tetragonalize the plaquette operators and keep track of the phase factors that arise.

To see how the proof works, consider an initial configuration $|F(D)\rangle$ where neither p nor p' has any loop extending in the overlapping region. Figure 2.6 illustrates $\mathcal{B}_{p'}^{\hexagon}\mathcal{B}_p^{\hexagon}$ for this case. After applying $\mathcal{B}_p^{\hexagon}$, the overlap with $|F(D)\rangle$ is positive as shown in the previous subsection. Then for $\mathcal{B}_{p'}^{\hexagon}$ we tetragonalize p' as indicated by the shaded regions in Fig. 2.6. As we can see from the illustration, the dimer flip at each step changes the transition

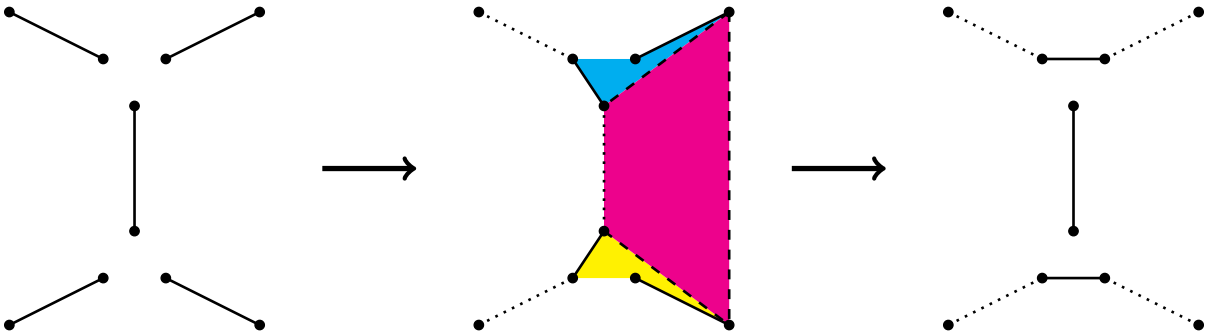

Figure 2.6: Illustration of $\mathcal{B}_{p'}^{\hexagon}\mathcal{B}_p^{\hexagon}$ acting on an initial configuration without any loops in the overlap area between neighboring plaquettes p and p'. The dashed lines in the middle figure are auxiliary lines for tetragonalization.

loop number (again corresponding to case 1 or 2 from Appendix 2.8), and therefore the overlap with $|F(D)\rangle$ remains positive. The reverse ordering $\mathcal{B}_p^{\hexagon}\mathcal{B}_{p'}^{\hexagon}$ works very similarly: After applying $\mathcal{B}_{p'}^{\hexagon}$, one can tetragonalize p such that each elementary dimer flip in $\mathcal{B}_p^{\hexagon}$ changes the loop number. So we have shown that both $\langle F(D)|\mathcal{B}_p^{\hexagon}\mathcal{B}_{p'}^{\hexagon}|F(D)\rangle$ and $\langle F(D)|\mathcal{B}_{p'}^{\hexagon}\mathcal{B}_p^{\hexagon}|F(D)\rangle$ are positive.

Next we consider a slightly more complicated initial configuration $|F(D)\rangle$ in which plaquette p is occupied by a loop; for an illustration of $\mathcal{B}_p^{\hexagon}\mathcal{B}_{p'}^{\hexagon}$ here see Fig. 2.7. After applying $\mathcal{B}_{p'}^{\hexagon}$ the overlap with $|F(D)\rangle$ is positive as usual. However, when we then apply $\mathcal{B}_p^{\hexagon}$, some of the elementary dimer flips fall into case 3 from Appendix 2.8 (see the two shaded tetragons in the middle figure). It is then essential to carefully track the phases accumulated. It turns out that the phases cancel so that the overlap with $|F(D)\rangle$ remains positive in the end. For the opposite ordering $\mathcal{B}_{p'}^{\hexagon}\mathcal{B}_p^{\hexagon}$ one can tetragonalize without running into case 3, yielding $\langle F(D)|\mathcal{B}_{p'}^{\hexagon}\mathcal{B}_p^{\hexagon}|F(D)\rangle > 0$ as well.

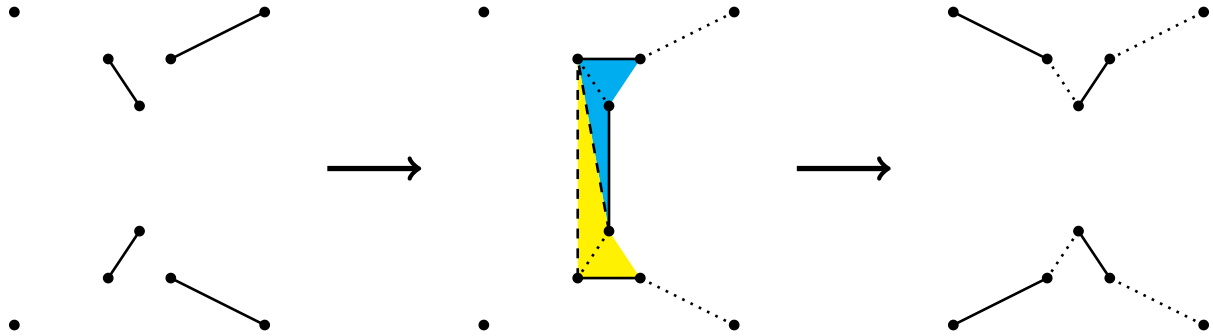

Figure 2.7: Variation of Fig. 2.6 in which the plaquette p is occupied by a loop.

The remaining two cases arise when the loop extends to both p and p' plaquettes beyond the overlapping region. By applying the same technique, one can see that for those cases both $\langle F(D)|\mathcal{B}_{p}^{\hexagon}\mathcal{B}_{p'}^{\hexagon}|F(D)\rangle$ and $\langle F(D)|\mathcal{B}_{p'}^{\hexagon}\mathcal{B}_{p}^{\hexagon}|F(D)\rangle$ encounter one elementary dimer flip that falls into case 3 and that $\langle F(D)|\mathcal{B}_{p'}^{\hexagon}\mathcal{B}_{p}^{\hexagon}|F(D)\rangle = \langle F(D)|\mathcal{B}_{p}^{\hexagon}\mathcal{B}_{p'}^{\hexagon}|F(D)\rangle = |A|e^{\pm i\frac{\pi}{4}}$.

Putting these results together, we see that $\mathcal{B}_{p}^{\hexagon}\mathcal{B}_{p'}^{\hexagon} = \mathcal{B}_{p'}^{\hexagon}\mathcal{B}_{p}^{\hexagon}$ in the restricted subspace, which is a key ingredient for obtaining a commuting-projector Hamiltonian on the Fisher lattice.

Bibliography

[1] Ian Affleck, Tom Kennedy, Elliott H. Lieb, and Hal Tasaki. Rigorous results on valence-bond ground states in antiferromagnets. *Phys. Rev. Lett.*, 59:799–802, Aug 1987.

[2] Ian Affleck, Tom Kennedy, Elliott H. Lieb, and Hal Tasaki. Valence bond ground states in isotropic quantum antiferromagnets. *Comm. Math. Phys.*, 115(3):477–528, 1988.

[3] Franz J Ahlers, Martin Gtz, and Klaus Pierz. Direct comparison of fractional and integer quantized hall resistance. 15 March 2017.

[4] Jason Alicea and Paul Fendley. Topological phases with parafermions: Theory and blueprints. *Annual Review of Condensed Matter Physics*, 7(1):119–139, 2016.

[5] P. W. Anderson. *Mater. Res. Bull.*, 8:153, 1973.

[6] P. W. Anderson. *Science*, 235:1196, 1987.

[7] F. A. Bais and J. K. Slingerland. Condensate-induced transitions between topologically ordered phases. *Phys. Rev. B*, 79:045316, Jan 2009.

[8] Leon Balents, Lorenz Bartosch, Anton Burkov, Subir Sachdev, and Krishnendu Sengupta. Putting competing orders in their place near the mott transition. *Phys. Rev. B*, 71:144508, Apr 2005.

[9] Maissam Barkeshli, Parsa Bonderson, Meng Cheng, and Zhenghan Wang. *Preprint*, 2014.

[10] Maissam Barkeshli and Chetan Nayak. *Preprint*, 2016.

[11] Maissam Barkeshli and Xiao-Liang Qi. Topological nematic states and non-abelian lattice dislocations. *Phys. Rev. X*, 2:031013, Aug 2012.

[12] Maissam Barkeshli and Jay D. Sau. *Preprint*, 2015.

[13] B. Bauer, L. Cincio, B. P. Keller, M. Dolfi, G. Vidal, S. Trebst, and A. W. W. Ludwig. *Nature Communications*, 5:5137, 2014.

[14] B. Bauer, P. Corboz, R. Orús, and M. Troyer. Implementing global abelian symmetries in projected entangled-pair state algorithms. *Phys. Rev. B*, 83:125106, 2011.

[15] Bela Bauer and Chetan Nayak. Area laws in a many-body localized state and its implications for topological order. *Journal of Statistical Mechanics: Theory and Experiment*, 2013(09):P09005, 2013.

[16] Daniel Ben-Zion, Diptarka Das, and John McGreevy. Exactly solvable models of spin liquids with spinons, and of three-dimensional topological paramagnets. *Phys. Rev. B*, 93:155147, Apr 2016.

[17] Erez Berg, Emanuele G. Dalla Torre, Thierry Giamarchi, and Ehud Altman. Rise and fall of hidden string order of lattice bosons. *Phys. Rev. B*, 77:245119, Jun 2008.

[18] B. Andrei Bernevig and Shou-Cheng Zhang. Quantum spin hall effect. *Phys. Rev. Lett.*, 96:106802, Mar 2006.

[19] B Blok and X G Wen. Effective theories of the fractional quantum hall effect: Hierarchy construction. *Phys. Rev. B Condens. Matter*, 42(13):8145–8156, 1 November 1990.

[20] Parsa Bonderson. *Non-Abelian Anyons and Interferometry*. PhD thesis, California Institute of Technology, May 2007.

[21] P. Bruillard, S.-H. Ng, E. Rowell, and Z. Wang. On modular categories. *Preprint*, 2013.

[22] Oliver Buerschaper, Miguel Aguado, and Guifré Vidal. Explicit tensor network representation for the ground states of string-net models. *Phys. Rev. B*, 79:085119, Feb 2009.

[23] Oliver Buerschaper, Siddhardh C. Morampudi, and Frank Pollmann. Double semion phase in an exactly solvable quantum dimer model on the kagome lattice. *Phys. Rev. B*, 90:195148, Nov 2014.

[24] Nick Bultinck, Michael Mariën, Dominic J. Williamson, Mehmet B. Sahinoğlu, Jutho Haegeman, and Frank Verstraete. *Preprint*, 2015.

[25] Pasquale Calabrese and John Cardy. Entanglement entropy and quantum field theory. *Journal of Statistical Mechanics: Theory and Experiment*, 2004(06):P06002, 2004.

[26] A. H. Castro Neto, F. Guinea, N. M. R. Peres, K. S. Novoselov, and A. K. Geim. The electronic properties of graphene. *Rev. Mod. Phys.*, 81:109–162, Jan 2009.

[27] Xie Chen, Zheng-Cheng Gu, Zheng-Xin Liu, and Xiao-Gang Wen. Symmetry-protected topological orders in interacting bosonic systems. *Science*, 338(6114):1604–1606, 2012.

[28] Xie Chen, Zheng-Cheng Gu, Zheng-Xin Liu, and Xiao-Gang Wen. Symmetry protected topological orders and the group cohomology of their symmetry group. *Phys. Rev. B*, 87:155114, Apr 2013.

[29] Xie Chen, Zheng-Cheng Gu, and Xiao-Gang Wen. Local unitary transformation, long-range quantum entanglement, wave function renormalization, and topological order. *Phys. Rev. B Condens. Matter*, 82(15):155138, 26 October 2010.

[30] Xie Chen, Zheng-Cheng Gu, and Xiao-Gang Wen. Classification of gapped symmetric phases in one-dimensional spin systems. *Phys. Rev. B*, 83:035107, 2011.

[31] Meng Cheng. Superconducting proximity effect on the edge of fractional topological insulators. *Phys. Rev. B*, 86:195126, Nov 2012.

[32] Ching-Kai Chiu, D. I. Pikulin, and M. Franz. Strongly interacting majorana fermions. *Phys. Rev. B*, 91:165402, Apr 2015.

[33] L. Cincio and G. Vidal. Characterizing topological order by studying the ground states on an infinite cylinder. *Phys. Rev. Lett.*, 110:067208, 2013.

[34] J. Ignacio Cirac, Didier Poilblanc, Norbert Schuch, and Frank Verstraete. Entanglement spectrum and boundary theories with projected entangled-pair states. *Phys. Rev. B*, 83:245134, Jun 2011.

[35] David J. Clarke, Jason Alicea, and Kirill Shtengel. Exotic non-abelian anyons from conventional fractional quantum hall states. *Nature Comm.*, 4:1348, 2013.

[36] C. Dasgupta and B. I. Halperin. Phase transition in a lattice model of superconductivity. *Phys. Rev. Lett.*, 47:1556–1560, Nov 1981.

[37] Marcel den Nijs and Koos Rommelse. Preroughening transitions in crystal surfaces and valence-bond phases in quantum spin chains. *Phys. Rev. B*, 40:4709–4734, Sep 1989.

[38] J. Dubail and N. Read. Tensor network trial states for chiral topological phases in two dimensions and a no-go theorem in any dimension. *Phys. Rev. B*, 92:205307, Nov 2015.

[39] P. Dziawa, B. J. Kowalski, K. Dybko, R. Buczko, A. Szczerbakow, M. Szot, E. Lusakowska, T. Balasubramanian, B. M. Wojek, M. H. Berntsen, O. Tjernberg, and T. Story. *Nat Mater*, 11(12):1023–1027, Dec 2012.

[40] I.S. Eliens, J.C. Romers, and F.A. Bais. Diagrammatics for bose condensation in anyon theories. *Phys. Rev. B*, 90:195130, 2014.

[41] Dominic V. Else and Chetan Nayak. Classifying symmetry-protected topological phases through the anomalous action of the symmetry on the edge. *Phys. Rev. B*, 90:235137, Dec 2014.

[42] Xiao-Gang Wen Esko Keski-Vakkuri. *Int. J. Mod. Phys. B*, 7:4227, 1993.

[43] M. Fannes, B. Nachtergaele, and R. F. Werner. Finitely correlated states on quantum spin chains. *Comm. Math. Phys.*, 144(3):443–490, 1992.

[44] Paul Fendley. Parafermionic edge zero modes in z n -invariant spin chains. *Journal of Statistical Mechanics: Theory and Experiment*, 2012(11):P11020, 2012.

[45] Matthew P. A. Fisher and D. H. Lee. Correspondence between two-dimensional bosons and a bulk superconductor in a magnetic field. *Phys. Rev. B*, 39:2756–2759, Feb 1989.

[46] Michael E. Fisher. On the dimer solution of planar ising models. *J. Math. Phys.*, 7(10):1776–1781, 1966.

[47] John Ove Fjaerestad. Classical and quantum dimers on the star lattice. *Preprint*, 2008.

[48] E. Fradkin and Steven A. Kivelson. Short range resonating valence bond theories and superconductivity. *Mod. Phys. Lett. B*, 4:225, 1990.

[49] P. Di Francesco, P. Mathieu, and D. Senéchal. *Conformal Field Theory*. Graduate texts in contemporary physics. Springer, New York, 1997.

[50] Michael Freedman, Matthew B. Hastings, Chetan Nayak, and Xiao-Liang Qi. Weakly coupled non-abelian anyons in three dimensions. *Phys. Rev. B*, 84:245119, 2011.

[51] Michael Freedman, Matthew B. Hastings, Chetan Nayak, Xiao-Liang Qi, Kevin Walker, and Zhenghan Wang. Projective ribbon permutation statistics: A remnant of non-abelian braiding in higher dimensions. *Phys. Rev. B*, 83:115132, 2011.

[52] Michael Freedman, Chetan Nayak, Kirill Shtengel, Kevin Walker, and Zhenghan Wang. A class of p,t-invariant topological phases of interacting electrons. *Annals of Physics*, 310(2):428 – 492, 2004.

[53] J Frhlich and A Zee. Large scale physics of the quantum hall fluid. *Nucl. Phys. B*, 364(3):517–540, 28 October 1991.

[54] Liang Fu. Topological crystalline insulators. *Phys. Rev. Lett.*, 106:106802, Mar 2011.

[55] Liang Fu and C. L. Kane. Topological insulators with inversion symmetry. *Phys. Rev. B*, 76:045302, Jul 2007.

[56] Liang Fu, C. L. Kane, and E. J. Mele. Topological insulators in three dimensions. *Phys. Rev. Lett.*, 98:106803, Mar 2007.

[57] A. Gendiar, N. Maeshima, and T. Nishino. Stable Optimization of a Tensor Product Variational State. *Progr. Theor. Phys.*, 110(4):691–699, 2003.

[58] Thierry Giamarchi. *Quantum Physics in One Dimension*. International Series of Monographs on Physics. Oxford University Press, USA, February 2004.

[59] M. Greiter, X. G. Wen, and F. Wilczek. *Phys. Rev. Lett.*, 66:3205, 1991.

[60] M. Greiter, X. G. Wen, and F. Wilczek. *Nucl. Phys. B*, 374:567, 1992.

[61] Eytan Grosfeld and Ady Stern. Electronic transport in an array of quasiparticles in the $\nu = 52$ non-abelian quantum hall state. *Phys. Rev. B*, 73:201303, 2006.

[62] Zheng-Cheng Gu and Michael Levin. Effect of interactions on two-dimensional fermionic symmetry-protected topological phases with Z_2 symmetry. *Phys. Rev. B*, 89:201113, May 2014.

[63] Zheng-Cheng Gu, Michael Levin, Brian Swingle, and Xiao-Gang Wen. Tensor-product representations for string-net condensed states. *Phys. Rev. B*, 79:085118, Feb 2009.

[64] Zheng-Cheng Gu, Zhenghan Wang, and Xiao-Gang Wen. Lattice model for fermionic toric code. *Phys. Rev. B*, 90:085140, Aug 2014.

[65] F D Haldane and E H Rezayi. Finite-size studies of the incompressible state of the fractionally quantized hall effect and its excitations. *Phys. Rev. Lett.*, 54(3):237–240, 21 January 1985.

[66] F D M Haldane. Fractional quantization of the hall effect: A hierarchy of incompressible quantum fluid states. *Phys. Rev. Lett.*, 51(7):605–608, 15 August 1983.

[67] F. D. M. Haldane. Model for a quantum hall effect without landau levels: Condensed-matter realization of the "parity anomaly". *Phys. Rev. Lett.*, 61:2015–2018, Oct 1988.

[68] Bertrand I. Halperin, Yuval Oreg, Ady Stern, Gil Refael, Jason Alicea, and Felix von Oppen. Adiabatic manipulations of majorana fermions in a three-dimensional network of quantum wires. *Phys. Rev. B*, 85:144501, 2012.

[69] M. Z. Hasan and C. L. Kane. *Colloquium* : Topological insulators. *Rev. Mod. Phys.*, 82:3045–3067, Nov 2010.

[70] M. B. Hastings. Lieb-schultz-mattis in higher dimensions. *Phys. Rev. B*, 69:104431, Mar 2004.

[71] M. B. Hastings. Sufficient conditions for topological order in insulators. *Europhysics Letters*, 70(6):824, 2005.

[72] M B Hastings and Xiao-Gang Wen. Quasiadiabatic continuation of quantum states: The stability of topological ground-state degeneracy and emergent gauge invariance. *Phys. Rev. B Condens. Matter*, 72(4):045141, 25 July 2005.

[73] Yasuhiro Hieida, Kouichi Okunishi, and Yasuhiro Akutsu. Numerical renormalization approach to two-dimensional quantum antiferromagnets with valence-bond-solid type ground state. *New Journal of Physics*, 1(1):7, 1999.

[74] Ching-Yu Huang, Xie Chen, and Frank Pollmann. Detection of symmetry-enriched topological phases. *Phys. Rev. B*, 90:045142, 2014.

[75] Taylor L. Hughes, Emil Prodan, and B. Andrei Bernevig. Inversion-symmetric topological insulators. *Phys. Rev. B*, 83:245132, Jun 2011.

[76] David A. Huse, Rahul Nandkishore, Vadim Oganesyan, Arijeet Pal, and S. L. Sondhi. Localization-protected quantum order. *Phys. Rev. B*, 88:014206, 2013.

[77] Mohsin Iqbal, Didier Poilblanc, and Norbert Schuch. Semionic resonating valence-bond states. *Phys. Rev. B*, 90:115129, Sep 2014.

[78] B Jeckelmann and B Jeanneret. The quantum hall effect as an electrical resistance standard. *Rep. Prog. Phys.*, 64(12):1603, 7 November 2001.

[79] Chao-Ming Jian and Michael Zaletel. The existence of featureless paramagnets on the square and the honeycomb lattices in 2+1d. 2015.

[80] Hong-Chen Jiang, Zhenghan Wang, and Leon Balents. Identifying topological order by entanglement entropy. *Nat. Phys.*, 8(12):902–905, 11 November 2012.

[81] C. L. Kane and E. J. Mele. Quantum spin hall effect in graphene. *Phys. Rev. Lett.*, 95:226801, Nov 2005.

[82] P W Kasteleyn. The statistics of dimers on a lattice: I. the number of dimer arrangements on a quadratic lattice. *Physica*, 27(12):1209–1225, December 1961.

[83] Itamar Kimchi, S. A. Parameswaran, Ari M. Turner, Fa Wang, and Ashvin Vishwanath. Featureless and nonfractionalized mott insulators on the honeycomb lattice at 1/2 site filling. *Proceedings of the National Academy of Sciences*, 110(41):16378–16383, 2013.

[84] A Yu Kitaev. Unpaired majorana fermions in quantum wires. *Physics-Uspekhi*, 44(10S):131, 2001.

[85] Alexei Kitaev. Anyons in an exactly solved model and beyond. *Annals Phys.*, 321:2, 2006.

[86] Alexei Kitaev. Periodic table for topological insulators and superconductors. *arXiv preprint arXiv:0901.2686*, 2009.

[87] Alexei Kitaev and Liang Kong. Models for gapped boundaries and domain walls. *Comm. Math. Phys.*, 313(2):351–373, 2012.

[88] Alexei Kitaev and John Preskill. Topological entanglement entropy. *Phys. Rev. Lett.*, 96(11):110404, Mar 2006.

[89] A.Yu. Kitaev. Fault-tolerant quantum computation by anyons. *Ann. Phys.*, 303(1):2 – 30, 2003.

[90] Liang Kong. Anyon condensation and tensor categories. *Nucl. Phys. B*, 886(0):436 – 482, 2014.

[91] M König et al. Quantum spin hall insulator state in hgte quantum wells. *Science*, 318(5851):766–770, 2007.

[92] Ville Lahtinen, Andreas W. W. Ludwig, Jiannis K. Pachos, and Simon Trebst. Topological liquid nucleation induced by vortex-vortex interactions in kitaev's honeycomb model. *Phys. Rev. B*, 86:075115, Aug 2012.

[93] R B Laughlin. Anomalous quantum hall effect: An incompressible quantum fluid with fractionally charged excitations. *Phys. Rev. Lett.*, 50(18):1395–1398, 2 May 1983.

[94] Michael Levin. Protected edge modes without symmetry. *Phys. Rev. X*, 3:021009, May 2013.

[95] Michael Levin and Xiao-Gang Wen. Detecting topological order in a ground state wave function. *Phys. Rev. Lett.*, 96:110405, Mar 2006.

[96] Michael A. Levin and Xiao-Gang Wen. String-net condensation: A physical mechanism for topological phases. *Phys. Rev. B*, 71:045110, 2005.

[97] Hui Li and F. D. M. Haldane. Entanglement spectrum as a generalization of entanglement entropy: Identification of topological order in non-abelian fractional quantum hall effect states. *Phys. Rev. Lett.*, 101:010504, Jul 2008.

[98] Wei Li, Shuo Yang, Meng Cheng, Zheng-Xin Liu, and Hong-Hao Tu. Topology and criticality in the resonating affleck-kennedy-lieb-tasaki loop spin liquid states. *Phys. Rev. B*, 89:174411, 2014.

[99] Elliott Lieb, Theodore Schultz, and Daniel Mattis. Two soluble models of an antiferromagnetic chain. *Annals of Physics*, 16(3):407 – 466, 1961.

[100] Netanel H. Lindner, Erez Berg, Gil Refael, and Ady Stern. Fractionalizing majorana fermions: Non-abelian statistics on the edges of abelian quantum hall states. *Phys. Rev. X*, 2:041002, Oct 2012.

[101] Jie Lou, Shu Tanaka, Hosho Katsura, and Naoki Kawashima. Entanglement spectra of the two-dimensional affleck-kennedy-lieb-tasaki model: Correspondence between the valence-bond-solid state and conformal field theory. *Phys. Rev. B*, 84:245128, Dec 2011.

[102] Yuan-Ming Lu and Ashvin Vishwanath. Theory and classification of interacting integer topological phases in two dimensions: A Chern-Simons approach. *Phys. Rev. B Condens. Matter*, 86(12):125119, 14 September 2012.

[103] Andreas W W Ludwig, Didier Poilblanc, Simon Trebst, and Matthias Troyer. Two-dimensional quantum liquids from interacting non-abelian anyons. *New Journal of Physics*, 13(4):045014, 2011.

[104] Roman M. Lutchyn, Jay D. Sau, and S. Das Sarma. Majorana fermions and a topological phase transition in semiconductor-superconductor heterostructures. *Phys. Rev. Lett.*, 105:077001, 2010.

[105] Y. Maeno, T. M. Rice, and M. Sigrist. The intriguing superconductivity of strontium ruthenate. *Physics Today*, 54:42, 2001.

[106] R. Moessner and S. L. Sondhi. Resonating valence bond phase in the triangular lattice quantum dimer model. *Phys. Rev. Lett.*, 86:1881–1884, 2001.

[107] R. Moessner, S. L. Sondhi, and Eduardo Fradkin. Short-ranged resonating valence bond physics, quantum dimer models, and ising gauge theories. *Phys. Rev. B*, 65:024504, Dec 2001.

[108] G. Moore and N. Seiberg. Lectures on rational conformal field theory. In M. Green, R. Iengo, S. Randjbar-Daemi, E. Sezgin, and A. Strominger, editors, *Superstring '89*, Singapore, 1990. World Scientific.

[109] Gregory Moore and Nicholas Read. Nonabelions in the fractional quantum hall effect. *Nuclear Physics B*, 360(2):362–396, 1991.

[110] Titus Neupert, Huan He, Curt von Keyserlingk, Germán Sierra, and B Andrei Bernevig. Boson condensation in topologically ordered quantum liquids. *Phys. Rev. B*, 93(11):115103, 1 March 2016.

[111] T. Nishino, Y. Hieida, K. Okunushi, N. Maeshima, Y. Akutsu, and A. Gendiar. Two-Dimensional Tensor Product Variational Formulation. *Progr. Theor. Phys.*, 105(3):409–417, 2001.

[112] Yuval Oreg, Gil Refael, and Felix von Oppen. Helical liquids and majorana bound states in quantum wires. *Phys. Rev. Lett.*, 105:177002, 2010.

[113] R. Orús and G. Vidal. Infinite time-evolving block decimation algorithm beyond unitary evolution. *Phys. Rev. B*, 78:155117, Oct 2008.

[114] M. Oshikawa. Insulator, conductor, and commensurability: A topological approach. *Phys. Rev. Lett.*, 90:236401, Jun 2003.

[115] Masaki Oshikawa. Commensurability, excitation gap, and topology in quantum many-particle systems on a periodic lattice. *Phys. Rev. Lett.*, 84:1535–1538, Feb 2000.

[116] Stellan Östlund and Stefan Rommer. Thermodynamic limit of density matrix renormalization. *Phys. Rev. Lett.*, 75:3537–3540, Nov 1995.

[117] S. A. Parameswaran, Itamar Kimchi, Ari M. Turner, D. M. Stamper-Kurn, and Ashvin Vishwanath. Wannier permanent wave functions for featureless bosonic mott insulators on the 1/3-filled kagome lattice. *Phys. Rev. Lett.*, 110:125301, Mar 2013.

[118] D. Perez-Garcia, F. Verstraete, M. M. Wolf, and J. I. Cirac. Peps as unique ground states of local hamiltonians. *Quantum Info. Comput.*, 8(6):650–663, July 2008.

[119] H. C. Po, H. Watanabe, M. P. Zaletel, and A. Vishwanath. Filling-Enforced Quantum Band Insulators in Spin-Orbit Coupled Crystals. *ArXiv e-prints*, June 2015.

[120] Frank Pollmann, Erez Berg, Ari M. Turner, and Masaki Oshikawa. Symmetry protection of topological phases in one-dimensional quantum spin systems. *Phys. Rev. B*, 85:075125, Feb 2012.

[121] Frank Pollmann and Ari M. Turner. Detection of symmetry-protected topological phases in one dimension. *Phys. Rev. B*, 86:125441, Sep 2012.

[122] Frank Pollmann, Ari M Turner, Erez Berg, and Masaki Oshikawa. Entanglement spectrum of a topological phase in one dimension. *Phys. Rev. B*, 81(6):064439, 26 February 2010.

[123] Andrew C. Potter and Romain Vasseur. *Preprint*, 2016.

[124] Andrew C. Potter and Ashvin Vishwanath. *Preprint*, 2015.

[125] Xiao-Liang Qi. A new class of (2 + 1)-dimensional topological superconductors with $\mathbb{Z}_8$ topological classification. *New J. Phys.*, 15(6):065002, 2013.

[126] Xiao-Liang Qi and Shou-Cheng Zhang. Topological insulators and superconductors. *Rev. Mod. Phys.*, 83:1057–1110, Oct 2011.

[127] Yang Qi, Zheng-Cheng Gu, and Hong Yao. Double-semion topological order from exactly solvable quantum dimer models. *Phys. Rev. B*, 92:155105, Oct 2015.

[128] N. Read and Dmitry Green. Paired states of fermions in two dimensions with breaking of parity and time-reversal symmetries and the fractional quantum Hall effect. *Phys. Rev. B*, 61:10267, 2000.

[129] N. Read and S. Sachdev. *Nucl. Phys. B*, 316:609, 1989.

[130] Daniel S. Rokhsar and Steven A. Kivelson. Superconductivity and the quantum hard-core dimer gas. *Phys. Rev. Lett.*, 61:2376–2379, Nov 1988.

[131] E. Rowell, R. Stong, and Z. Wang. On classification of modular tensor categories. *Commun. Math. Phys.*, 292(2):343, 2009.

[132] Shinsei Ryu, Joel E. Moore, and Andreas W. W. Ludwig. Electromagnetic and gravitational responses and anomalies in topological insulators and superconductors. *Phys. Rev. B*, 85:045104, Jan 2012.

[133] Shinsei Ryu, Andreas P Schnyder, Akira Furusaki, and Andreas W W Ludwig. Topological insulators and superconductors: tenfold way and dimensional hierarchy. *New Journal of Physics*, 12(6):065010, 2010.

[134] Shinsei Ryu and Shou-Cheng Zhang. Interacting topological phases and modular invariance. *Phys. Rev. B*, 85:245132, Jun 2012.

[135] U. Schollwöck. The density-matrix renormalization group. *Rev. Mod. Phys.*, 77:259–315, Apr 2005. Equation 134.

[136] U. Schollwöck. The density-matrix renormalization group in the age of matrix product states. *Annals of Physics*, 326(1):96 – 192, 2011.

[137] Norbert Schuch, David Pérez-García, and Ignacio Cirac. Classifying quantum phases using matrix product states and projected entangled pair states. *Phys. Rev. B*, 84:165139, 2011.

[138] D. N. Sheng, Z. Y. Weng, L. Sheng, and F. D. M. Haldane. Quantum spin-hall effect and topologically invariant chern numbers. *Phys. Rev. Lett.*, 97:036808, Jul 2006.

[139] Robert-Jan Slager, Andrej Mesaros, Vladimir Juricic, and Jan Zaanen. The space group classification of topological band-insulators. *Nat Phys*, 9(2):98–102, Feb 2013.

[140] Y. Tanaka, Zhi Ren, T. Sato, K. Nakayama, S. Souma, T. Takahashi, Kouji Segawa, and Yoichi Ando. Experimental realization of a topological crystalline insulator in snte. *Nat Phys*, 8(11):800–803, Nov 2012.

[141] Nicolas Tarantino and Lukasz Fidkowski. Discrete spin structures and commuting projector models for 2d fermionic symmetry protected topological phases. 7 April 2016.

[142] Ari M. Turner, Yi Zhang, Roger S. K. Mong, and Ashvin Vishwanath. Quantized response and topology of magnetic insulators with inversion symmetry. *Phys. Rev. B*, 85:165120, Apr 2012.

[143] F. Verstraete and J. I. Cirac. Renormalization algorithms for Quantum-Many Body Systems in two and higher dimensions. *Preprint*, 2004.

[144] F. Verstraete, M. M. Wolf, D. Perez-Garcia, and J. I. Cirac. Criticality, the area law, and the computational power of projected entangled pair states. *Phys. Rev. Lett.*, 96:220601, Jun 2006.

[145] Guifré Vidal. Efficient classical simulation of slightly entangled quantum computations. *Phys. Rev. Lett.*, 91:147902, 2003.

[146] Guifré Vidal. Efficient simulation of one-dimensional quantum many-body systems. *Phys. Rev. Lett.*, 93:040502, 2004.

[147] Guifre Vidal. Classical simulation of infinite-size quantum lattice systems in one spatial dimension. *Phys. Rev. Lett.*, 98(7):070201, 2007.

[148] T. B. Wahl, H.-H. Tu, N. Schuch, and J. I. Cirac. Projected entangled-pair states can describe chiral topological states. *Phys. Rev. Lett.*, 111:236805, Dec 2013.

[149] Kevin Walker. Codimension 1 defects, categorified group actions, and condensing fermions. IPAM workshop on "Symmetry and Topology in Quantum Matter", 2015.

[150] Xiao-Gang Wen. Construction of bosonic symmetry-protected-trivial states and their topological terms via $G \times SO(\infty)$ non-linear σ-models. 30 October 2014.

[151] Xiao-Gang Wen. Symmetry-protected topological invariants of symmetry-protected topological phases of interacting bosons and fermions. *Phys. Rev. B*, 89:035147, Jan 2014.

[152] Xiao-Gang Wen. A theory of 2+1d bosonic topological orders. *Natl Sci Rev*, 3(1):68–106, 1 March 2016.

[153] Steven R. White. Density matrix formulation for quantum renormalization groups. *Phys. Rev. Lett.*, 69:2863–2866, Nov 1992.

[154] Shuo Yang, Thorsten B. Wahl, Hong-Hao Tu, Norbert Schuch, and J. Ignacio Cirac. Chiral projected entangled-pair state with topological order. *Phys. Rev. Lett.*, 114:106803, Mar 2015.

[155] Hong Yao, Liang Fu, and Xiao-Liang Qi. *Preprint*, 2010.

[156] Hong Yao and Shinsei Ryu. Interaction effect on topological classification of superconductors in two dimensions. *Phys. Rev. B*, 88:064507, Aug 2013.

[157] Yi-Zhuang You and Meng Cheng. Preprint, 2016.

[158] Michael P. Zaletel, S. A. Parameswaran, Andreas Rüegg, and Ehud Altman. Chiral bosonic mott insulator on the frustrated triangular lattice. *Phys. Rev. B*, 89:155142, Apr 2014.

[159] Yi Zhang, Tarun Grover, Ari Turner, Masaki Oshikawa, and Ashvin Vishwanath. Quasiparticle statistics and braiding from ground-state entanglement. *Phys. Rev. B*, 85:235151, 2012.

[160] Yi Zhang, Tarun Grover, Ari Turner, Masaki Oshikawa, and Ashvin Vishwanath. Quasiparticle statistics and braiding from ground-state entanglement. *Phys. Rev. B*, 85:235151, 2012.

[161] Yi Zhang, Tarun Grover, and Ashvin Vishwanath. General procedure for determining braiding and statistics of anyons using entanglement interferometry. *Phys. Rev. B*, 91:035127, Jan 2015.